Synthesis and Characterization of Ferroelectric and Antiferroelectric Complex Perovskite Systems

by
Siqi Huo

B.Sc., South China Agricultural University, 2011

Thesis Submitted in Partial Fulfillment of the
Requirements for the Degree of
Master of Science

in the
Department of Chemistry
Faculty of Science

© Siqi Huo 2014
SIMON FRASER UNIVERSITY
Fall 2014

Approval

Name:	**Siqi Huo**
Degree:	**Master of Science**
Title:	***Synthesis and Characterization of Ferroelectric and Antiferroelectric Complex Perovskite Systems***
Examining Committee:	**Chair:** Dr. David Vocadlo Professor

Dr. Zuo-Guang Ye
Senior Supervisor
Professor

_____

Dr. Daniel B. Leznoff
Supervisor
Professor

_____

Dr. Byron Gates
Supervisor
Associate Professor

_____

Dr. Vance Williams
External Examiner
Associate Professor
Department of Chemistry
Simon Fraser University

_____

Date Defended/Approved: December 9th, 2014 _____

Partial Copyright Licence

SFU

Abstract

Single crystals of $Pb(Sc_{1/2}Nb_{1/2})O_3$ (PSN) were grown by a high-temperature solution method using $(PbO + B_2O_3)$ as flux. The size of the as-grown crystals varies from 1 to 2 mm. X-ray diffraction indicates a pure perovskite phase without B-site ordering. Polarized light microscopy shows that the crystals are of rhombohedral symmetry at room temperature and become cubic at 112 ℃ on heating which is the Curie temperature (T_C). A relaxor-to-ferroelectric phase transition is confirmed at T_C by dielectric spectroscopy. Frequency-dependent permittivity is observed in dielectric measurement, revealing relaxor behavior. Poling the crystal at room temperature does not change T_C but suppresses the permittivity. A typical ferroelectric hysteresis loop is obtained at room temperature, indicating the ferroelectric nature of the PSN crystal.

A new antiferroelectric solid solution of $(1-x)PbZrO_3-xPb(Zn_{1/2}W_{1/2})O_3$ [(1-x)PZ-xPZnW, with x = 0 - 10%] has been prepared in the form of ceramics by conventional solid state reaction method. X-ray powder diffraction reveals the perovskite structure of the (1-x)PZ-xPZnW ceramics. The lattice parameters a_{pc} and b_{pc} of the ceramics reduce more significantly than c_{pc} with increasing concentration of PZnW. These variations of lattice constants as a function of compositions indicate the formation of solid solution. T_C decreases from 228 ℃ to 195 ℃ when the percentage of PZnW increases from 0% to 10%. Meanwhile, another transition related to the transformation from antiferroelectric (AFE) to an intermediate ferroelectric (FE) phase was observed and its transition temperature (T_{AFE-FE}) was found to shift from 213 ℃ for x = 0 to 58 ℃ for x = 0.10. A typical ferroelectric hysteresis loop was obtained, indicating the FE nature of the intermediate phase.

The antiferroelectric $0.97PbZrO_3-0.03Pb(Zn_{1/2}W_{1/2})O_3$ (97%PZ-3%PZnW) ceramic was prepared by the solid state reaction method. The temperature dependence of dielectric permittivity was studied. T_C on cooling and heating are both 212 ℃, indicating a second-order phase transition. Another phase transition below T_C was observed, from the AFE phase at room temperature to an intermediate phase at higher temperature. This transition shows thermal hysteresis, occurring at 155 ℃ and 175 ℃ on cooling and heating, respectively. It represents a first-order phase transition. Within the temperature range of the intermediate phase, ferroelectric hysteresis loops were displayed and a non-centrosymmetric structure was revealed by second harmonic generation, which indicates the FE nature for the intermediate phase. High resolution X-ray diffraction and the subsequent refinement results show that the intermediate FE phase is rhombohedral in space group *R3m* and the AFE phase is orthorhombic in space group *Pbam*. A phase diagram of the $(1-x)PbZrO_3-xPb(Zn_{1/2}W_{1/2})O_3$ solid solution has been established as a result of this work.

To my dear parents,

Shaohua Huo and Peiyi Peng

Acknowledgements

To begin with, I would like to express my deep gratitude to my senior supervisor, Dr. Zuo-Guang Ye, for his guidance, support and encouragement during my Master study. I would like to thank my supervisory committee members, Dr. Daniel B. Leznoff and Dr. Byron Gates for their valuable comments and helpful advices. I would like to further thank Dr. Vance Williams for being my internal examiner.

My thanks also go to all the members in Dr. Ye research group, both past and present, for their support and friendship. I would especially like to thank Dr. Nan Zhang, Dr. Alexei A. Bokov and Dr. Hua Wu for insightful discussion on data analysis, and Dr. Hamel Tailor and Dr. Yujuan Xie for teaching me valuable experimental skills.

I appreciate the financial and facility support from 4D LABS, Department of Chemistry, Simon Fraser University, the Natural Sciences and Engineering Research Council of Canada and the U.S. Office of Naval Research.

Finally, I would like to thank my parents Shaohua Huo and Peiyi Peng for their love and support. Without their encouragement, I would never have come to this stage.

Table of Contents

List of Tables

List of Figures

xii

List of Abbreviations

FE	Ferroelectric
AFE	Antiferroelectric
PE	Paraelectric
pc	Pseudocubic
t	Tolerance factor
PSN	$Pb(Sc_{1/2}Nb_{1/2})O_3$
PZ	$PbZrO_3$
PZnW	$Pb(Zn_{1/2}W_{1/2})O_3$
PZ-PZnW	$PbZrO_3$-$Pb(Zn_{1/2}W_{1/2})O_3$
XRD	X-ray Diffraction
PLM	Polarized Light Microscopy
A	Analyzer
P	Polarizer
SEM	Scanning Electron Microscopy
SHG	Second-harmonic generation
P-E loops	Polarization versus electric field loops
E_c	Coercive field in ferroelectric materials or critical field in antiferroelectric materials
E_F	Critical field for the field-induced ferroelectric state in antiferroelectric materials
E_A	Critical field for releasing the field-induced ferroelectric state in antiferroelectric materials
P_r	Remanent polarization
P_S	Saturated polarization
T_C	Curie temperature
T_{AFE-FE}	Transition temperature of the ferroelectric-antiferroelectric phase transition
T_m	The temperature of the maximum dielectric constant
T_B	Burns temperature
T	Temperature
ε'	Real part of dielectric constant
ε''	Imaginary part of dielectric constant

ε'_m	Maximum dielectric constant
Δn	Birefringence
ZFC	Zero-field cooling
ZFH	Zero-field heating
TSSG	Top-seeded solution growth

Chapter 1.

General Introduction

This thesis presents the synthesis and characterization of Pb-based complex perovskite ferroelectric, antiferroelectric and relaxor ferroelectric materials in the forms of single crystals and ceramics. Our goal is to gain a comprehensive understanding of their structures, electrical properties and phase transitions. This chapter will provide a general introduction to some background and essential concepts, including the perovskite structure, the piezoelectricity, ferroelectricity and antiferroelectrcity, the order of phase transitions, the relaxor ferroelectrics, the $Pb(Sc_{1/2}Nb_{1/2})O_3$ system, and the $PbZrO_3$-based systems.

1.1. Perovskite Structure

Materials that crystallize in the perovskite structure have a general formula of ABO_3. Many important functional materials adopt the perovskite structure, which makes it a popular topic in research. The perovskite exhibits a high flexibility of composition and structural distortion, leading to a wide range of properties such as the piezoelectric, pyroelectric, ferroelectric, and magnetic properties.

The fundamental structure of perovskite is cubic where the oxygen is situated at each of the six face centers of the cube, forming a corner-linked array of octahedra. The larger A-cation occupies the space between the oxygen octahedra while the smaller B-cation sits at the center of the octahedra. The coordination numbers of A- and B-cations are 12 and 6, respectively. Figure 1.1 illustrates a typical perovskite structure.

The stability and distortion of crystal structures vary with different types and sizes of A- and B- cations. The tolerance factor (t) is an indicator for predicting the stability of perovskite structures, which can be calculated by the following equation[1, 2]:

$$t = \frac{R_A + R_O}{\sqrt{2}(R_B + R_O)} \quad ,$$ (1.1)

where R_A, R_B and R_O are the radii of the A-, B-, and oxygen ions, respectively. A large number of metallic ions are stable in the perovskite structure as long as the t value is within the range of 0.88< t < 1.09.[3]
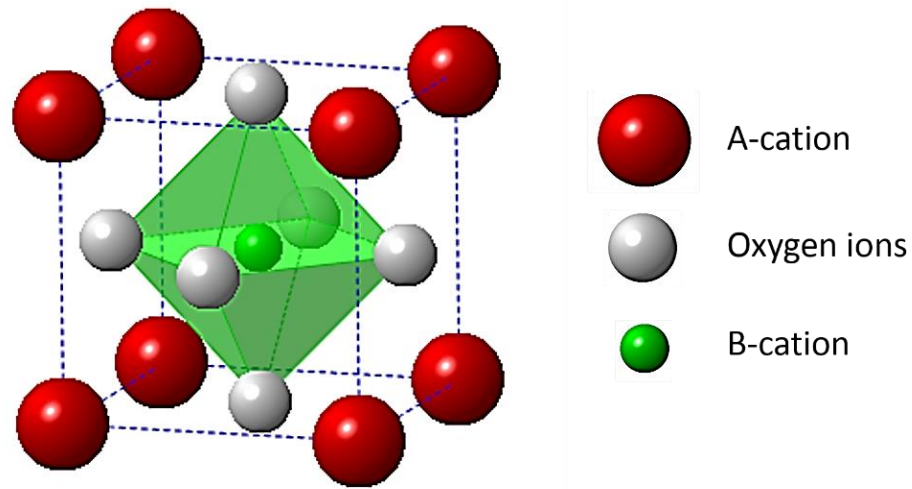
Figure 1.1.   Prototype perovskite ABO_3 unit cell in cubic symmetry. A-cation and B-cation are at the corner and body centre of the unit cell, respectively. Oxygen ions occupy the face centres.

1.2. Piezoelectricity

Piezoelectricity was first discovered by Jacques and Pierre Curie in 1880 while they were studying certain materials such as quartz, zinc blende, topaz, and tourmaline, which all had the ability to generate an electrical potential in response to applied mechanical pressure[4, 5]. The prefix "piezo" originates from the Greek word "pressure". Twenty out of the thirty-two crystal classes (point groups) are non-centrosymmetric and can exhibit a direct piezoelectric property. By applying a pressure to a piezoelectric material, electric charge starts accumulating within the material; this is known as direct

piezoelectric effect. However, the materials can also generate a mechanical strain if one applies an electrical field to it; this is known as the converse piezoelectric effect. Piezoelectric is a linear effect.[5] The direct effect can be described using the following equation [6]:

$$D_i = d_{ij}\sigma_j \qquad (i = 1,\ 2,\ 3;\ j = 1,\ 2,\ \ldots,6), \quad (1.2)$$

where σ_i is the mechanical stress applied to a piezoelectric material, D_i is the charge density and d_{ij} is the piezoelectric coefficient in unit pC/N. D_i is produced in the i direction by the application of a mechanical stress σ_j along j direction. In general, the piezoelectric coefficients that are measured along the direction of the applied field are called the longitudinal coefficients (ij=11, 22, 33). While the piezoelectric coefficients that are measured in the direction perpendicular to the field are called the transverse coefficients (ij=12, 23, 31). The remaining are shear coefficients (ij=14, 15, 16, …, 34, 35, 36).[7]

Figure 1.2 demonstrates the direct piezoelectric effect with the field and polarization along the z-axis ($i = j = 3$). When applying a compressive stress onto the piezoelectric material, the polarization decreases. However, when a tensile force is applied instead, the polarization increases.

Conversely, the change of strain resulting from the converse piezoelectric effect can be expressed using:

$$S_j = d_{ji}E_i \quad (i = 1,\ 2,\ 3;\ j = 1,\ 2,\ldots,\ 6), \qquad (1.3)$$

where S_j is the mechanical strain, E_j is the external electric field in j direction and d_{ji} is the piezoelectric coefficient.
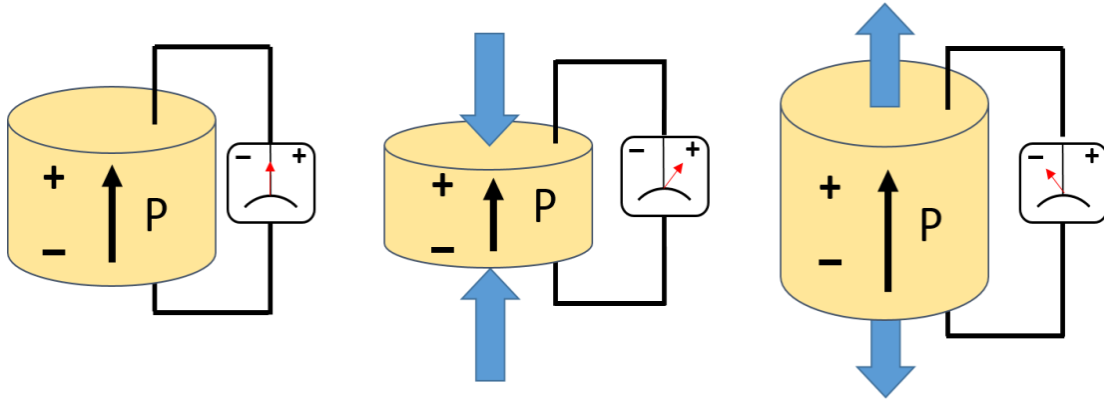
Figure 1.2.   Schematic illustration of the direct piezoelectricity.

1.3. Ferroelectricity and Antiferroelectricity

Ferroelectric (FE) materials are those with a spontaneous electric polarization which is switchable with a sufficiently strong electric field applied in an appropriate direction.[6] Therefore, in order to be ferroelectric, the material itself must be polar. This also means that ferroelectric materials must show piezoelectric effects. Ferroelectric properties can be characterized by the polarization-electric field hysteresis loop (P-E loop), as shown in Figure 1.3. It describes the dependence of polarization (P) on the strength of an applied field (E). A ferroelectric single crystal usually is not uniformly polarized but rather, it forms domains. The polarization within a domain is uniform but polarizations between domains could have different orientations. Similarly, grains in a virgin polycrystalline sample are randomly orientated. Thus, their initial polarization is zero (point A). When an electric field is applied, domains begin to rotate to align with the field. This gives rise to an increase in polarization (curve AB). The saturation of polarization P_S is reached at high field strength, but subsequently decreasing field does not reproduce polarization behavior A → B that was observed on increasing the field. Instead, a remnant polarization, P_r, remains even when the E field is reduced to zero. The field applied in the opposite direction that brings the polarization down to zero is called the coercive field E_C.
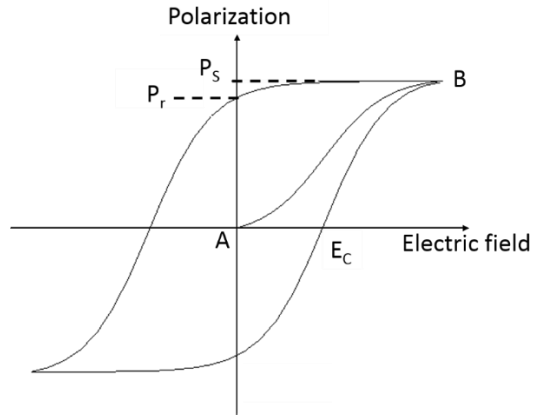
Figure 1.3.   Display of a typical ferroelectric polarization-electric field hysteresis loop.

The ferroelectric state usually exists at low-temperature because thermal motions at high temperatures tend to destroy the ferroelectric ordering in adjacent octahedra along with the structural symmetry.[8] The temperature at which the breakdown of dipole ordering begins upon heating is known as the Curie temperature (T_C). Above T_C, the material exhibits paraelectric (PE) behaviour. For ferroelectrics of perovskite structure, the paraelectric structure is of cubic symmetry belonging to the space group $Pm\bar{3}m$. In the PE phase, no residual polarization is retained after the electric field is removed. Within the paraelectric phase, the dielectric constant ε' obeys the Curie-Weiss Law [8, 9]:

$$\varepsilon' = \frac{C}{T-T_o} \quad , \tag{1.4}$$

where T is the absolute temperature in Kelvin, C and T_o are the Curie and Weiss constants, respectively. When the temperature falls below T_C, the material experiences a structural phase transition to a lower symmetry. An abrupt change in dielectric permittivity always appears during a ferroelectric phase transition, as shown in Figure 1.4.
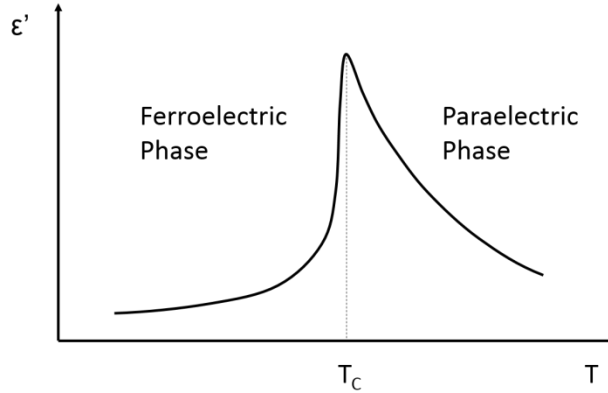
Figure 1.4.   Variation of dielectric constant (ε') as a function of temperature (T) of a ferroelectric material, indicating the ferroelectric – paraelectric phase transition at Curie temperature (T_C).

The characteristics of antiferroelectric (AFE) materials are different from those of ferroelectrics. The structure of antiferroelectrics is non-polar. Individual dipoles orient antiparallel to their adjacent dipoles, which results in a net polarization of zero. For antiferroelectric materials, antiparallel dipole ordering is more stable than the parallel dipole ordering. However, application of an electric field can stabilize the parallel dipole arrangement and thus lower its free energy. Therefore, if the external field reaches the critical value E_F, a phase transition from antiferroelectric to ferroelectric phase can be induced. But when the field decreases to a critical value, E_A, the material restores its antiferroelectric phase. As a result, at high positive or negative fields a field-induced ferroelectric hysteresis loop appears, giving rise to the double hysteresis loop, as shown in Figure 1.5a, which is a feature of antiferroelectrics.[10] E_A and E_F decrease on heating because the energy barrier between antiferroelectric and ferroelectric states is reduced by thermal energy.[11] Similarly to FEs, an antiferroelectric material transforms to a paraelectric phase at the Curie temperature T_C.[12]

Figure 1.5b represents the electric field effect on the minimum free energy depending on the type of ordering. With the absence of external fields, adjacent dipoles align antiparallel to each other because AFE alignment has the lowest free energy. With the application of an external field, the free energy of the FE ordering that goes along the same direction as the field reduces (state ②) and once the field reaches E_F, it reaches the lowest point (state ③). Thus, a field-induced transition from AFE to FE phase takes

6

place. The polarization consequently surges with increasing field as the dipoles are forced to align parallel to each others as it is saturated at high field. If the field decreases to critical value E_A, the minimum energy of FE ordering restores back to the initial magnitude. The FE→AFE phase transition occurs and the polarization plunges (state ④).
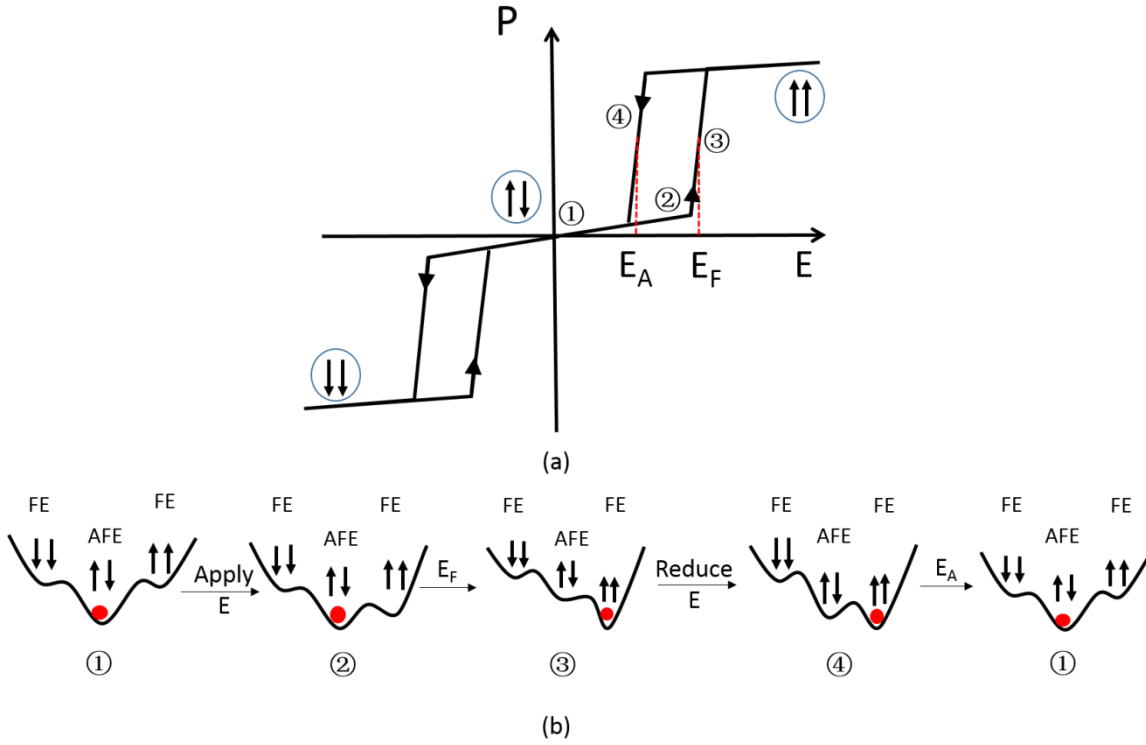
Figure 1.5.   (a) Illustration of a double hysteresis loop of antiferroelectric behaviour. (b) Energy diagrams explaining the double hysteresis loops with application of an electric field.

Antiferroelectrics are useful materials for potential applications as high-energy-storage capacitors. Figure 1.6 shows the hysteresis loop and effective energy density of three kinds of materials: linear dielectrics (LDs), ferroelectrics, and antiferroelectrics.[10] The energy storage density J (energy stored per unit volume) is defined as:[13]

$$J = \int_0^{P_{max}} E dP = \int_0^{E_{max}} P dE \quad . \qquad (1.5)$$

According to Equation 1.5, the storage energy density J of a dielectric can be represented by the numerical integration of the area between P = 0 and the P-E curves. In Figure 1.6, the shaded area in P-E curves represents the energy released (J_{re}) during discharging process. It is evident that J_{re} of FEs is dissipated by its remnant polarization. On the other hand, the polarizations of LDs are always small. Therefore, AFEs are superior to FEs and LDs in the usage as high energy density capacitors, because of their field-induced AFE-FE phase transition.[13]

(a)
Ferroelectrics

(b)
Linear dielectrics

(c)
Antiferroelectrics
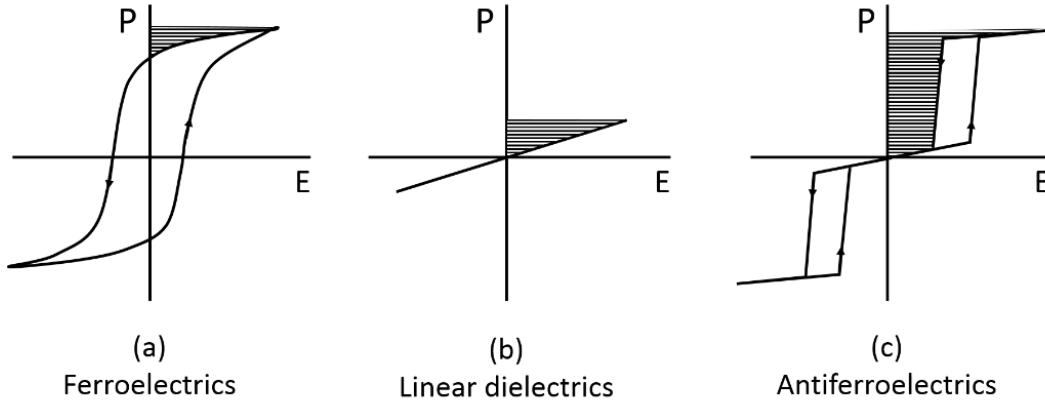
Figure 1.6.   Polarization-electric field curves of (a) ferroelectrics, (b) linear dielectrics and (c) antiferroelectrics. The shaded areas denote the discharge/recoverable energy.

1.4. Order of Phase Transitions

It is convenient to treat the ferroelectric phase transition by using the elastic Gibbs function G as a state function of the ferroelectric system. A ferroelectric crystal is considered to have an intrinsic spontaneous polarization along a specific axis determined by its structural symmetry. Free energy G is independent of the polarization direction. If the external pressure is assumed to be constant and $\mathbf{P_S}$ is stable at a certain temperature, G can be expressed in terms of polarization $\mathbf{P_s}$ as follows[14]:

$$G = G_0 + \frac{1}{2} a\mathbf{P}_S^2 + \frac{1}{4} b\mathbf{P}_S^4 + \frac{1}{6} c\mathbf{P}_S^6 + ..., \tag{1.6}$$

where G_0, a, b and c are temperature-dependent coefficients. G_0 is the elastic free energy of the system when $\mathbf{P_S}$ = 0. Terms higher than $\mathbf{P}_S^6$ can be omitted because their values

are negligible. The system is stable when G reaches a minimum value under the conditions of:

$$\frac{\partial G}{\partial P} = 0 \quad , \tag{1.7}$$

$$\text{and} \quad \frac{\partial E}{\partial P} = \chi^{-1} > 0 \quad . \tag{1.8}$$

The relation between the field **E** and **P** is given by:

$$E = \frac{\partial G}{\partial P} = a\boldsymbol{P} + b\boldsymbol{P}^3 + c\boldsymbol{P}^5 \quad , \tag{1.9}$$

Combining Equation 1.6 to 1.9, the equations for a ferroelectric system then take the forms as:

$$\boldsymbol{P_S}(a + b\boldsymbol{P}_S^2 + c\boldsymbol{P}_S^4) = 0 \quad , \tag{1.10}$$

$$\text{and} \quad \chi^{-1} = a + 3b\boldsymbol{P}_S^2 + 5c\boldsymbol{P}_S^4 > 0 \quad . \tag{1.11}$$

In the paraelectric state, $\boldsymbol{P_s} = 0$, then $\chi^{-1} = a > 0$, which means that a is a positive value when the system is in a stable paraelectric state. The susceptibility $\chi = \varepsilon'\text{-}1$, and since $\varepsilon' \gg$ 1, $\chi \approx \varepsilon'$. According to the Curie-Weiss Law, the susceptibility χ can be written as $\chi = C /$ $(T-T_o)$. Thus, $a = \chi^{-1} = (T-T_o) / C$ when $T > T_o$. In the case of $P_S \neq 0$, b > 0 corresponds to a second-order phase transition, while b < 0 corresponds to a first-order phase transition.[14,15]

1.4.1.   Second Order Phase Transition

The root of $\boldsymbol{P}_S^2 \neq 0$ with a positive value (corresponding to a real value $\boldsymbol{P_s}$) from Equation 1.10 is

$$\boldsymbol{P}_S^2 = \frac{(|b| - 4ac)^{1/2}}{2c} \qquad (b{<}0) \quad . \tag{1.12}$$

9

As $|a| \cdot c \ll b^2$, Equation 1.12 can be simplified as $\mathbf{P}_S^2 = -\frac{a}{b}$ ($a < 0$, $b > 0$) by expanding the square root in inverse powers of b^2. As $a = (T-T_o)/C$ is deduced from the Curie Weiss Law, $\mathbf{P}_S^2$ can be written as $\mathbf{P}_S^2 = -(T - To)/(C \cdot b)$.[14,16] Shown in Figure 1.7a is a plot of the spontaneous polarization $\mathbf{P_S}$ as a function of temperature. $\mathbf{P_s}$ decrease gradually to 0 when temperature approaching T_C upon heating.

Combining Equation 1.6 and 1.12 and considering $\mathbf{E} = 0$, the free energy for the second order phase transitions can be expressed as:

$$G - G_o = -\frac{a^2}{b} = -\left(\frac{T - T_o}{C}\right)^2 / b < 0 \qquad . \qquad (1.13)$$

The first and second derivatives of Equation 1.13 are continuous and discontinuous, respectively. The difference of entropy (the first derivative of free energy) is zero at T_o. In other words, the transition takes place at T_o and the Curie temperature T_C equals to T_o in the second-order phase transitions. The variation of $G-G_0$ as a function of temperature is plotted in Figure 1.7b. The double wells in the energy diagram at temperatures lower than T_o ($=T_C$) correspond to two stable ferroelectric states. The susceptibility and its reciprocal as a function of temperature are plotted in Figure 1.7c.

(a)   (b)   (c)
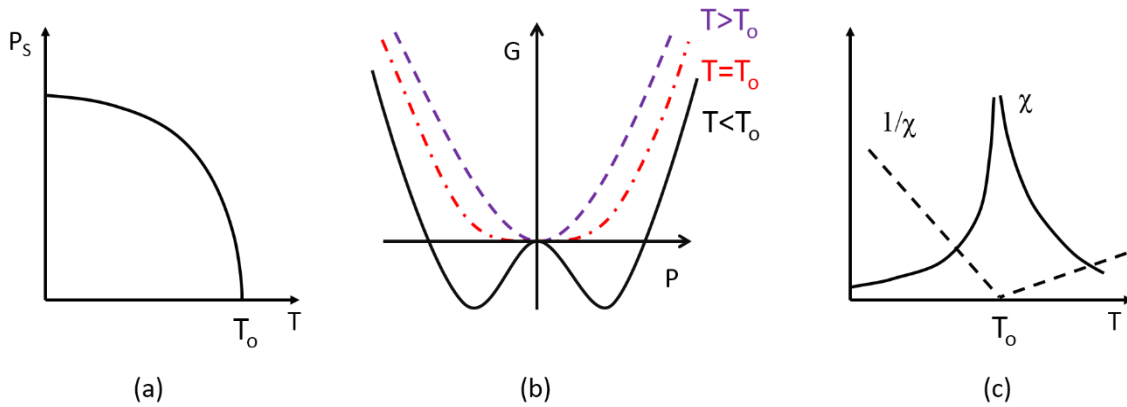
Figure 1.7.   Second-order phase transitions represented by the temperature dependences of (a) $\mathbf{P_S}$, (b) the variation of free energy, and (c) the susceptibility χ and its inverse $1/\chi$.

1.4.2. First Order Phase Transition

For first order phase transition (b < 0), the spontaneous polarization $\mathbf{P_S}$ can be expressed using Equation 1.13 and free energy $G - G_o$ and can be written as:

$$G - G_o = \frac{b(b^2 - 6ab) - (b^2 - 4ac)^{3/2}}{24c^2} \quad . \qquad (1.14)$$

Because the first derivative of $G - G_o$ is always greater than zero, the free energy increase monotonically with increasing value of a. Suppose $G = G_o$ and set $a = a_o$, then $a_o = 3b^2 / 16c$. If $a < a_o$, G is still less than G_o and $\mathbf{P}_S^2$ will relate to a state that is more stable than the state without polarization. In addition, when substituting a_o into the Curie-Weiss Law, it shows that $T_o \neq T_C$. Demonstrated in Figure 1.8b is the free energy versus polarizations at different temperatures. The polarized state is stable at $T < T_C$, corresponding to the double wells. The polarized state shows the same energy as the paraelectric state (the middle well) at $T = T_C$. When temperature increases to T_1 ($T_1 > T_C$), the paraelectric state becomes most stable and the phase transition occurs. However, the reverse phase transition from paraelectric to ferroelectric phase takes place at T_2 ($T_2 < T_C$).[17] As a result, thermal hysteresis occurs between heating and cooling for the first order phase transitions. This is one of the key characteristics of this type of phase transitions.

On account of a sharp change in $\mathbf{P_S}$, the term of $\mathbf{P}_S^4$ cannot be neglected. By substituting a_o into Equation 1.13, it shows that $\mathbf{P}_S^2 = \frac{3|b|}{4c}$ at a temperature slightly below T_C. Thus, P_S decreases abruptly and discontinuously to zero at T_C (Figure 1.8a). At $T < T_C$, $\chi^{-1} = 4a$. The reciprocal of susceptibility as a function of temperature is shown in Figure 1.8c. It can be seen that χ^{-1} changes abruptly at T_C.

11
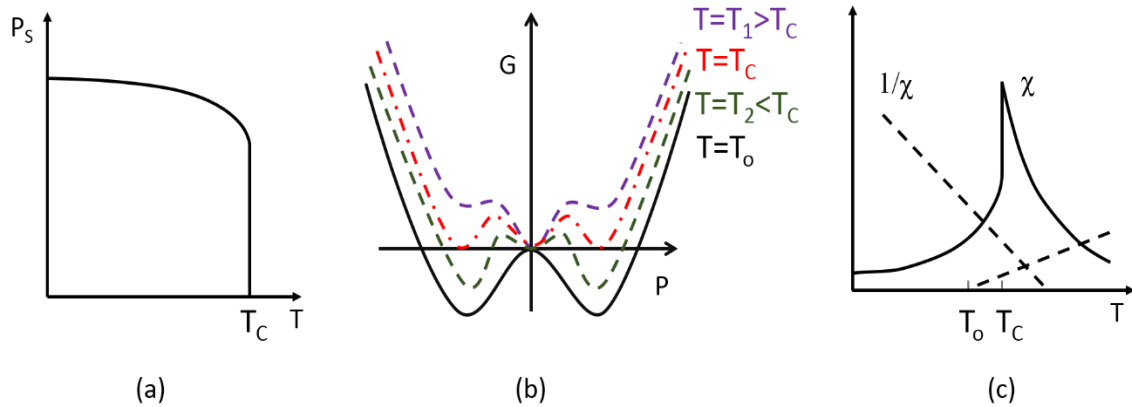
Figure 1.8. First-order phase transitions represented by the temperature dependences of (a) P_S, (b) the variation of free energy, and (c) the susceptibility χ and its inverse $1/\chi$.

1.5. Relaxor Ferroelectrics

Relaxor ferroelectrics form a special class of disordered ferroelectric materials. There has been an enormous growth of interest in the topic of relaxor materials over the past 20 years. They exhibit high dielectric permittivity with diffuse dielectric maximum in its temperature dependence,[18, 19] which makes them excellent candidates for capacitors. At higher temperatures, relaxor ferroelectrics are in the nonpolar paraelectric state that is similar to the normal ferroelectrics above T_C, where the dielectric constant ε' also follows the Curie-Weiss Law.[18] Upon cooling, they transform into an ergodic relaxor (ER) state where polar nanoregions (PNRs) with dipole moments on nanoscale form and their orientations are randomly distributed. This transition takes place at the so called Burns temperature (T_B).[18] It is not considered a structural phase transition because no structure changes occur on either the macroscopic or mesoscopic scale. Dipole dynamics slows down upon further cooling, which generates a large and wide peak in the temperature dependence of dielectric permittivity with frequency dispersion, and it eventually becomes frozen. The magnitude of this peak (ε_m) is of the same order as, or higher than, the peaks in normal ferroelectrics at T_C but compared to the latter, it is highly diffuse. Noticeably, the dielectric maximum ε_m and its temperature T_m are frequency-dependent. With decreasing frequency, T_m drops while ε_m increases. In general, these properties are mostly associated with different cations occupying the crystallographically equivalent sites in the perovskite structure.[20] The prototypical relaxor behaviour was observed in the

perovskites with disorder of non-isovalent ions, for example, $Pb(Mg_{1/2}Nb_{1/2})O_3$ (PMN) [21] with partially ordered B-site cations and the nonstoichiometric solid solution of $Pb_{1-x}La_x(Zr_{1-y}Ti_y)_{1-x/4}O_3$ (PLZT)[22]. The effect of compositional ordering on the properties of relaxor ferroelectrics was initially studied in $Pb(Sc_{1/2}Ta_{1/2})O_3$ (PST) and $Pb(Sc_{1/2}Nb_{1/2})O_3$ (PSN) systems.[23, 24] It was discovered that an increased degree of B-site ordering resulted in an increase in the correlation length between local polar domains. This leads to a transition into an ordinary ferroelectric phase.

A superparaelectric model was proposed by Cross to describe relaxor ferroelectric behaviour.[20] This superparaelectric model is analogous with that of the superparamagnetic state, and it suggests that independent diploes at high temperature ($>T_m$) are dynamically disordered through thermal motion among different polarization states. During cooling the thermal effect decreases, but the size of PNRs and their energy barrier increases. It is expected that the dynamics of PNRs slows down and becomes frozen, which is similar to the case of spin glass materials. Dielectric relaxation of relaxor materials satisfies the Vogel-Fulcher (V-F) relationship:[25]

$$\omega = \omega_0 \; exp \left| \frac{-E_a}{(T_m - T_f)} \right| \quad , \qquad\qquad (1.15)$$

where ω_0, E_a and T_f are parameters.

The permittivity in a wide temperature range above T_m deviates from the Curie-Weiss law, which supports the existence of polar clusters. The dielectric properties in this temperature range can be described by using a quadratic law:[26]

$$\frac{\varepsilon_m}{\varepsilon} = 1 + \frac{(T - T_m)^2}{2\delta_m^2} \quad , \qquad\qquad (1.16)$$

where ε_m is the dielectric maximum and the parameter δ_m can be used to describe the diffuseness.

1.6. Pb(Sc$_{1/2}$Nb$_{1/2}$)O$_3$ Systems

The Pb(Sc$_{1/2}$Nb$_{1/2}$)O$_3$ (PSN) system was first synthesized in the form of ceramics by Smolenskii *et al.*[27] It shows a Curie temperature T$_C$ of around 90 °C.[27] Single crystals of PSN were grown using the flux method with a flux consisting of PbO or PbO+B$_2$O$_3$.[28,29,30] PSN belongs to the complex perovskite family with two different B cations on the B-site with 1:1 ratio. This type of perovskite is interesting because thermal treatment can alter its degree of B-cation ordering and therefore influences the material properties.[31] For example, fully compositionally ordered PSN shows typical ferroelectric behavior while disordered PSN demonstrates relaxor behavior.[32] The ordered structure can be revealed mainly by the $(\frac{1}{2} \frac{1}{2} \frac{1}{2})$ and $(\frac{3}{2} \frac{1}{2} \frac{1}{2})$ reflections in the X-ray diffraction pattern, due to the existence of the superlattice produced by the B-site ordering. B-cations (Sc^{3+} and Nb^{5+}) occupy the adjacent centers of oxygen octahedra alternatively in the fully ordered PSN system, giving rise to a superlattice formed by two interpenetrating sublattices, as shown in Figure 1.9. However, chemical disorder alone is not sufficient to generate the typical relaxor properties such as broadened dielectric peak with frequency dispersion down to low temperature. In this case, lead vacancies play an important role in suppressing the spontaneous ferroelectric transition. For instance, introduction of lead vacancies makes the disordered PST remain in a relaxor state and show similar properties as PMN.[33]
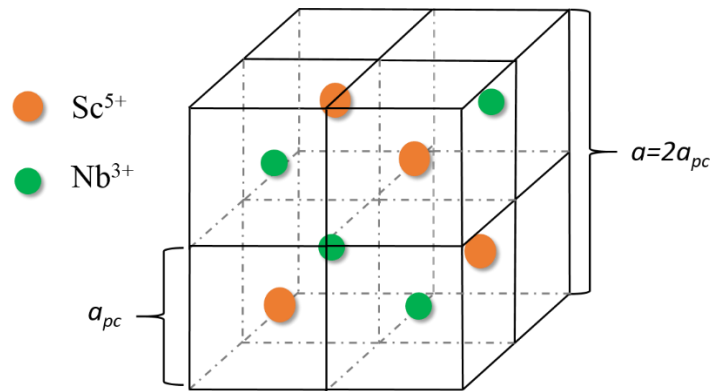
Figure 1.9.   Sketched structure of fully ordered perovskite Pb(Sc$_{1/2}$Nb$_{1/2}$)O$_3$ superlattice (Pb^{2+} and O^{2-} are omitted). Subscript "*pc*" stands for "pseudocubic setting".

The investigation by Chu et al. shows that the disordered PSN ceramics experience a spontaneous transition from relaxor state to ferroelectric state during zero-field cooling when the lead vacancies are suppressed.[32] The transition is relatively sharp, followed by a step-like anomaly in the temperature dependence of dielectric constants at different frequencies which occurs at several degrees below the temperature of permittivity maximum. PSN single crystal also presents diffuse and dispersive dielectric maximum, indicating the relaxor ferroelectric nature of the system.[34] However, this transition is different from that of relaxor $Pb(Mg_{1/2}Nb_{1/2})O_3$ (PMN) in which such a transition cannot be observed in their dielectric properties on zero-field cooling, but can be observed after the application of an electric field.[35] The difference between the dielectric behavior of different types of relaxors comes from the different kinetics for the development of the PNRs.[34] In the PSN system, the PNRs in the high-temperature ergodic state perform as ordering units, giving rise to a sharp order-disorder type ferroelectric phase transition.[36] The PNRs interact ferroelectrically with each other and generate a macroscopic order. The ferroelectric phase in $Pb(Zn_{1/3}Nb_{2/3})O_3$ (PZN) originates from the growth in the size of PNRs instead of the coupling between PNRs. On the other hand, the growth of PNRs in PMN is overpowered and the interaction causes the nonergodic state. Guo *et al.*[37] studied the poling behaviour of PSN using piezoresponse force microscopy. It was found that the domain structure and domain evolution of (001)-orientated PSN single crystals were consistent with the characteristics of relaxors even though it was in a room-temperature ferroelectric state. No clear domain wall movement can be observed in the PSN single crystal with the application of an intermediate voltage, while uniform changes of piezoresponse were obtained in contrast to the behaviour of a ferroelectric phase. Namely, PSN at room temperature still contains some degree of relaxor character.[37]

1.7. PbZrO$_3$-Based Systems

PbZrO$_3$ (PZ) is a well-known and the most widely used antiferroelectric perovskite system and has been extensively studied since the 1950s.[38] The antiferroelectricity of PZ originates from the antiparallel arrangement of adjacent Pb^{2+} ions along the $[110]_{pc}$ directions. The alignment of Pb^{2+} ions leads to the quadrupling of the unit cell, adopting an orthorhombic structure in the space group of *Pbam* with dimensions of $\sqrt{2}\,a_{pc} \times 2\sqrt{2}$

$a_{pc} \times 2c_{pc}$ (Figure 1.10),[39, 40] where a_{pc} and c_{pc} are lattice parameters of the pseudocubic perovskite subcell. An external electric field can change the crystal structure from the orthorhombic to a rhombohedral symmetry, which gives rise to a field-induced AFE-FE transition. PZ transforms from AFE to PE phase at T_C (~233 °C) [38] on heating. A possible intermediate ferroelectric phase exists in between the AFE and PE phase, which was first discovered by Scott from a PZ single crystal [41]. Whatmore et al. utilized an X-ray diffraction and dielectric measurements to verify the existence of the intermediate phase and reported that it is of rhombohedral symmetry.[42]
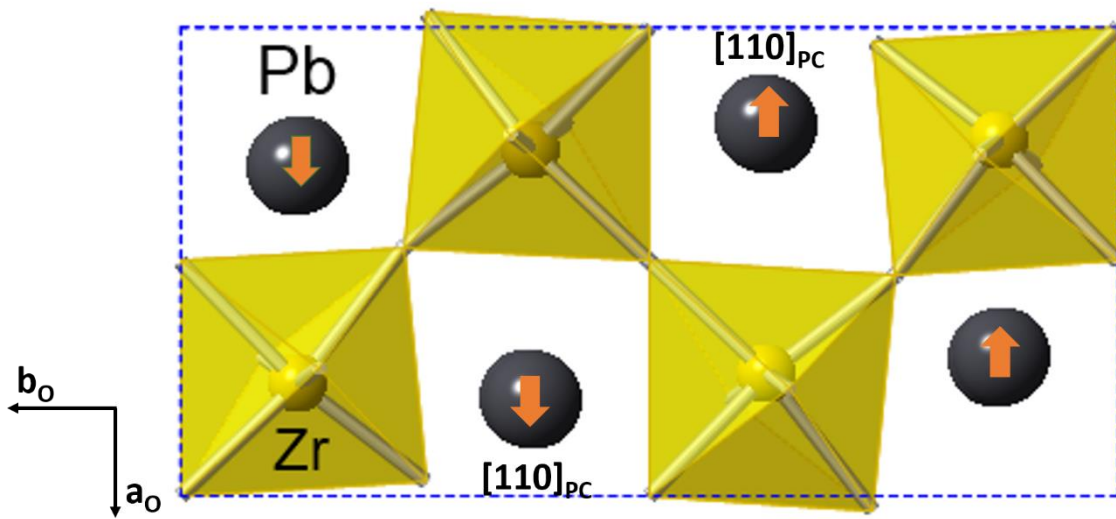
Figure 1.10.   The projection of refined structure of PbZrO$_3$ along the c_O-axis. Orange arrows indicate the direction of Pb^{2+} displacement.

To date, two phase transition theories have been formulated to interpret the phase switching process, which are the phenomenological theory and soft mode theory.

The first phenomenological model is the Landau–Devonshire (L–D) theory, which explains the phase transition process by the free energy difference in between the two phases involved. Later, Kittel assumed that two equivalent lattices exist in AFEs and they could be polarized independently with an interaction between them. P$_a$ and P$_b$ denote the polarizations of the two lattices, so the free energy of the system can be written as:

$$\Delta G = f(P_a^2 + P_b^2) + gP_aP_b + h(P_a^4 + P_a^4) \tag{1.17}$$

where *f*, *g*, *h* are phenomenological coefficients. A complete free energy function for orthorhombic AFEs was later developed by Whatmore et al.[43] For the orthorhombic AFEs, such as PZ, the free energy ΔG of the AFE state is the lowest at room temperature. Next comes ΔG of FE state followed by that of PE state. So the AFE phase is the most stable. The difference in ΔG between AFE and FE phase is small and as a result, the external electric field is able to induce a phase transition from AFE to FE phase. Upon heating, the free energy of the AFE phase rises more significantly than that of FE. At T_{AFE-FE}, the FE phase shows the smallest value of free energy and causes the phase transition from the AFE to FE state. When the temperature reaches T_C, PE has the lowest free energy and becomes the ground state.

The soft model connects the FE and AFE phases based on lattice vibration. It is known that the FE and AFE transitions result from the soft mode instabilities at the Brillouin Zone Center and Brillouin Zone Boundary, respectively.[11] As the temperature approaches the phase transition temperature, the instability causes the vibration frequency to decrease to zero, which results in a phase transition. The occurrence of phase transitions depends on the competition between the long-range Coulombic force, which is the restoring forces of FE phase, and the short-range force, which is restoring forces of AFE phase.

Because the phase switching behavior plays a significant role in the practical applications of AFE materials, understanding the nature of transition process is important. However, the temperature window for the intermediate FE phase is very narrow in PZ, making it difficult, if not impossible, to study its structure and phase transition nature. In addition, the critical field E_F of unmodified PZ system is far higher than its breakdown field, which limits their applications. Thus, chemical modifications have been performed on PZ to optimize its properties. The ions of La^{3+}, Ti^{4+} and Sr^{2+} were used to modify PZ simultaneously, forming the lead lanthanum stannate zirconate titanate (PLZST) solid solution, which successfully enlarges the longitudinal strain of the system.[44, 45] Ba^{2+} ion lowers E_F and T_C of the PZ ceramics. $PbZrO_3$-$Pb(Mg_{1/2}W_{1/2})O_3$[46], $PbZrO_3$-$Pb(In_{1/2}Nb_{1/2})O_3$[47], $PbZrO_3$-$Pb(Co_{1/3}Nb_{2/3})O_3$[48] and many other PZ-based solid solutions were prepared in which the temperature range of the intermediate FE phase was expanded, decreasing the transition temperature T_{AFE-FE}.

1.8. Objectives and Organization of the Thesis

The $Pb(Sc_{1/2}Nb_{1/2})O_3$ system belongs to the family of complex perovskite with two different B cations on the B-site with 1:1 ratio. This type of perovskite is interesting because the B-site ordering can be altered by thermal treatments.[31] Chemically disordered PSN in the forms of both ceramics and single crystals exhibits a phase transition from relaxor state to ferroelectric state upon cooling at zero-field.[32,34] This transition is sharp accompanied by a dielectric permittivity maximum with frequency dispersion. The macroscopic ferroelectric phase in the disordered PSN is attributed to the ferroelectric correlation between PNRs, which gives rise to a transition from cubic to rhombohedral symmetry on cooling.[36, 49] When an external voltage is applied, some degree of relaxor character can be observed such as absence of domain wall movement and uniform increases and decrease of piezoresponse.[37] To date, only a few reports have been available on the domain structure and phase transitions in PSN single crystals probably due to the difficulties encountered in growing PSN single crystals. In addition, the poling effect on the dielectric properties of PSN single crystal is poorly understood. Therefore, it is of particular interest to study the ferroelectric ordering, domain structure, phase transition, and poling effects of PSN single crystals. This part of work constituted **Chapter 3** of this thesis.

$PbZrO_3$ is one of the most widely used antiferroelectric materials. Chemical modifications on the PZ system have attracted extensive attention recently because of the potential applications of the PZ-based systems in high performance energy storage devices. Upon cooling, there is a possible intermediate ferroelectric phase in pure PZ system between the room-temperature AFE phase and the high-temperature (above T_C) paraelectric phase. This intermediate phase only exists within a narrow temperature range (a few degrees), making it difficult to study the structure and properties of this phase in pure PZ. Solid solutions of $PbZrO_3$-$Pb(Mg_{1/2}W_{1/2})O_3$ [46], $PbZrO_3$-$Pb(In_{1/2}Nb_{1/2})O_3$ [47] and some other PZ-based systems were synthesized, which exhibit a lower transition temperature of T_{AFE-FE}. Nevertheless, PZ-based solid solutions are primarily formed with FE end-members. We believe that forming PZ-based solid solution with an AFE end-member is an interesting approach to synthesize new AFEs and to investigate the ferroelectric and antiferroelectric properties, in particular, to study the structure and properties of the intermediate FE phase. In this work, $Pb(Zn_{1/2}W_{1/2})O_3$ (PZnW), which was

predicted to be an antiferroelectric perovskite compound, is utilized to form the antiferroelectric solid solution of $(1-x)PbZrO_3$-$xPb(Zn_{1/2}W_{1/2})O_3$ [$(1-x)PZ$-$xPZnW$]. The synthesis of the solid solution and the influences of PZnW on the structure and properties of PZ will be described in **Chapter 4**. Further investigation of the crystal structure and properties of the intermediate FE phase found in the $(1-x)PZ$-$xPZnW$ solid solution will be reported in **Chapter 5**.

Chapter 2.

Characterization: Principles and Techniques

The techniques and principles used to characterize the crystal structures and physical properties of the anti-/ferroelectric materials prepared in this work will be introduced in this chapter. It includes powder X-ray diffraction, dielectric spectroscopy, ferroelectric hysteresis measurement, polarized light microscopy, and the method of synthesis.

2.1. Powder X-Ray Diffraction

Powder X-ray Diffraction (XRD) is applied to identify crystal structures since crystals have different arrays of atoms that cause the incident beam of X-ray to diffract in many directions.

X-ray is a form of electromagnetic radiations with wavelength ranging from 0.1 to 100 Å. The X-rays which are most widely used in diffraction experiments are monochromatic X-rays. To produce them, high energy electrons are accelerated by a high electric field (higher than 30 kV) to strike a metal target, usually Cu, Mo, etc.. As illustrated in Figure 2.1a, some of the electrons in the Cu K shell can be ionized. Electrons in the outer shells, such as L or M shells, immediately fall down to the vacancy in the K shell and release energy. The transition energies released during this process emerge as X-ray radiation. In addition, they generate an emission spectrum because the values of transition energies are fixed.[50] The emission spectra vary according to different targets. For copper, the transition from 2p to 1s is called K_{α} and from 3p to 1s is called K_{β}, with wavelengths of 1.5418 Å and 1.3922 Å, respectively. Indeed, K_{α} radiation is an average value of $K_{\alpha 1}$ (1.54051 Å) and $K_{\alpha 2}$ (1.54433 Å) which is caused by the spin-orbit coupling of 2p electrons (Figure 2.1b).
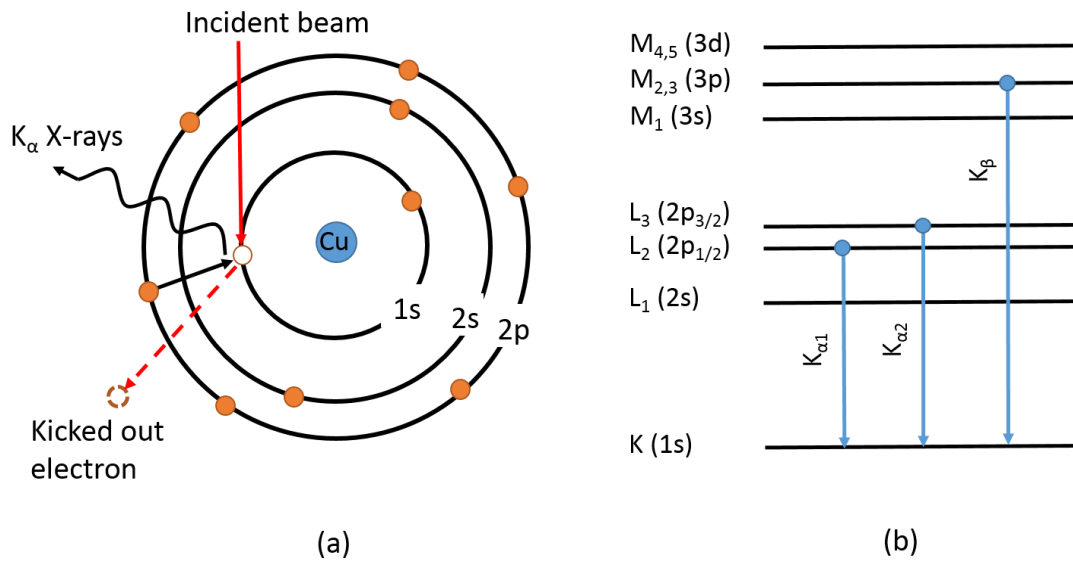
Figure 2.1. (a) Illustration of the generation of Cu *Kα* X-rays. (b) Demonstration of the copper *Kα1*, *Kα2* and *Kβ* emissions at atomic levels.

Substances with crystalline structure are highly ordered with an infinitely repeating array of 3-dimensional unit cells. They are therefore capable of diffracting radiation which is similar to the wavelength of interatomic separations. The most common type of radiation used is X-rays. The crystalline sample is considered as built up of discrete parallel lattice planes. The distance between planes is the d-spacing, d. The incident X-rays are scattered by the atoms and generate reflected beams. Reflected beams mostly cause destructive interference but they can interfere constructively in some specific directions, determined by the Bragg's Law:[8]

$$2d\sin\theta = n\lambda \quad , \tag{2.1}$$

where d is the interplanar spacing, θ is the incident angle and also known as Bragg angle, n in an integer and λ is the wavelength of the incident X-rays. Figure 2.2 demonstrates the derivation of Bragg's Law. The diffracted X-rays are detected and produce a diffraction pattern which is a plot of intensity as a function of the 2θ angle. Many diverse peaks appear at a diffraction pattern, each of which correspond to a set of planes (*hkl*) with the same d-spacing.
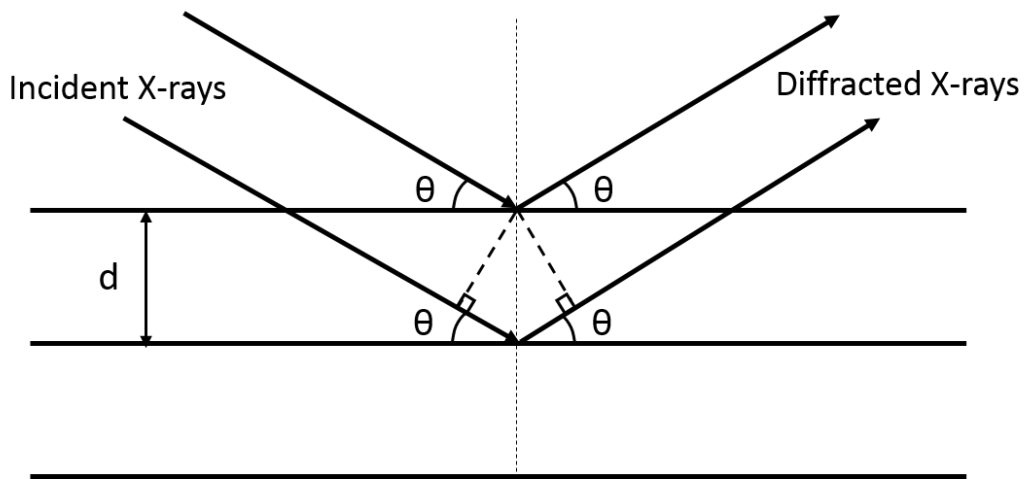
Figure 2.2.　　Derivation of Bragg's Law.

There are two key factors determining the X-ray diffraction patterns of substances. One is the size and shape of the unit cell. The other is the atomic number and d-spacing of different atoms in the unit cell. Therefore, a powder diffraction pattern of a crystal is unique and it can be utilized to identify the structure and symmetry of the sample. There are seven crystal systems that can be distinguished by XRD due to their special combination of three interaxial angles and three axial dimensions (Figure 2.3). The unit cell specification of the seven crystal systems are listed in Table 2.1. The relationship between lattice parameters and d-spacing varies with different structure symmetry. For example, the spacing formula of orthorhombic unit cells can be expressed by:[8]

$$\frac{1}{d_{hkl}^2} = \frac{h^2}{a^2} + \frac{k^2}{b^2} + \frac{l^2}{c^2} \quad , \tag{2.2}$$

where a, b, and c are lattice parameters of the unit cell and hkl are the Miller indices of a set of planes with distance d between them.
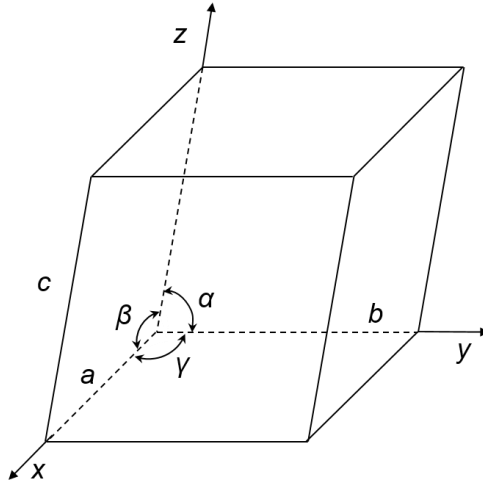
Figure 2.3.   A unit cell labeled with the lengths of the axes (*a*, *b*, *c*) and the angles between them *(α, β, γ)*.

Table 2.1.   The seven crystal systems with their restrictions in lattice parameters

Crystal system	Lattice Parameters
Cubic	$a = b = c$, $\alpha = \beta = \gamma = 90°$
Tetragonal	$a = b \neq c$, $\alpha = \beta = \gamma = 90°$
Orthorhombic	$a \neq b \neq c$, $\alpha = \beta = \gamma = 90°$
Hexagonal (Rhombohedral)	$a = b \neq c$, $\alpha = \beta = 90°$, $\gamma = 120°$ ($a = b = c$, $\alpha = \beta = \gamma < 90°$)
Trigonal	$a = b = c$, $\alpha = \beta = \gamma \neq 90°$
Monoclinic	$a \neq b \neq c$, $\alpha = \gamma = 90°$, $\beta \neq 90°$
Triclinic	$a \neq b \neq c$, $\alpha \neq \beta \neq \gamma \neq 90°$

Complex perovskites are of the same structure, but their symmetries and corresponding lattice parameters vary with compositions and temperature. For cubic symmetry ($a = b = c$, $\alpha = \beta = \gamma = 90°$), as calculated by Equation 2.2, d-spacing between {100}$_{cub}$, {110}$_{cub}$, and {111}$_{cub}$ planes are a, $a / \sqrt{2}$, and $a / \sqrt{3}$, respectively. Thus, (100)$_{cub}$, (110)$_{cub}$ and (111)$_{cub}$ reflections are singlet on the X-ray diffraction pattern of a substance of cubic symmetry. However, if the symmetry changes to a lower symmetry, peak splitting can be observed because the lattice parameters are no longer the same. Take the tetragonal symmetry ($a = b \neq c$, $\alpha = \beta = \gamma = 90°$) for example. Because *a* and *b*

parameters are the same but the c parameter is different from them, one can know that $d_{100}=d_{010}\neq d_{001}$. Consequently, there are two different diffraction angles of the $\{100\}_{cub}$ planes and the $(100)_{cub}$ reflection is a doublet. Figure 2.4 shows the splitting of XRD reflections of the $(111)_{cub}$, $(200)_{cub}$ and $(220)_{cub}$ with regard to different symmetries. Based on this principle, according to the characteristic XRD patterns, it is possible to deduce the phase symmetry of a sample.

In this work, the prepared (anti-)ferroelectric materials are complex perovskite compounds with different symmetries. XRD can be used to study the structural properties such as phase purity, structural symmetry and temperature dependence of structural symmetry (phase transition). Two XRD instruments that were used in this research are the Bruker D8 Advanced Diffractometer and PANalytical X'Pert Pro MPD Diffractometer. In addition, the Rietveld refinement is performed using the TOPAS Academic software in order to obtain accurate information of crystal structures, including the crystallographic point groups, phase components, lattice parameters, bond lengths and angles, and coordination environments.
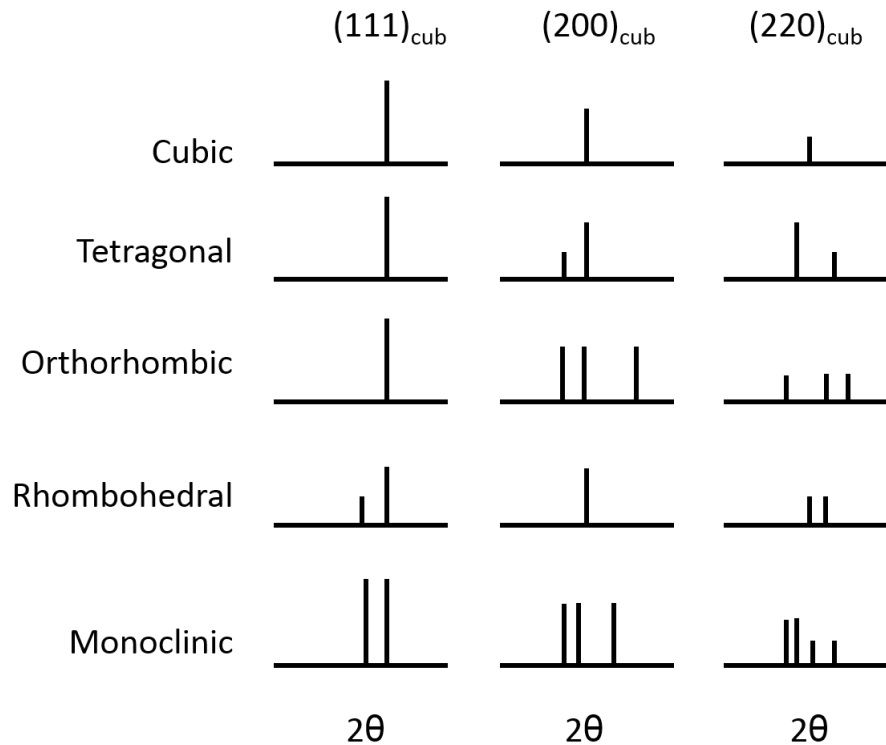
Figure 2.4.   Characteristic X-ray diffraction patterns for different symmetries displaying the corresponding splitting with regard to the $(111)_{cub}$, $(200)_{cub}$ and $(220)_{cub}$ reflections.

2.2. Dielectric Spectroscopy

Temperature and frequency dependences of dielectric properties (dielectric constants and dielectric loss) provide important information on the phase evolution of the piezo- and ferroelectric materials. The dielectric measurements are performed either on a Novocontrol Alpha high-resolution broadband dielectric analyzer or a Solartron 1260 impedance analyzer in combination with a Solartron 1296 dielectric interface. Figure 2.5 shows the schematic of the circuit used in the dielectric property measurements.
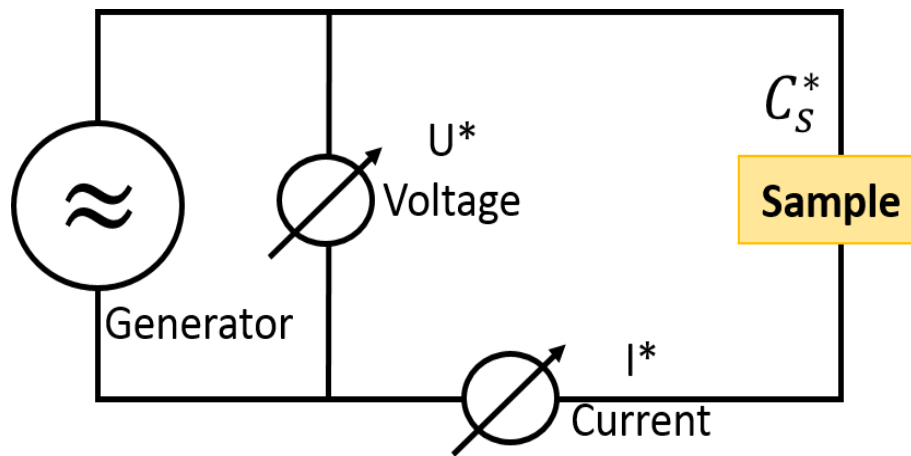
Figure 2.5.   A schematic diagram of the circuit used in dielectric property measurements.

The dielectric sample is connected to two electrodes, and an AC voltage U with frequency ω/2π is applied. The voltage U generates a current I at the same frequency in the sample. The applied voltage ranges from 1 V to 3 V and the frequency is between 3 μHz and 20 MHz. The complex voltage U* and complex current I* flowing through the sample are measured by a phase sensitive voltmeter and ammeter, respectively. The signals are output and used to calculate the complex impedance Z_S* of the sample which equals to:[51]

$$Z_S^* = Z' + iZ'' = \frac{U^*}{I^*} \quad .$$
(2.3)

The complex sample capacity C_S* is related to the complex impedance Z_S* by:

25

$$Z_S^* = -\frac{i}{\omega C_S^*} \qquad . \tag{2.4}$$

The complex dielectric constant ε^* and capacity C_S^* of the sample are related by:[51, 52]

$$\varepsilon^* = \varepsilon' - i\varepsilon'' = \frac{C_S^*}{C_0} \qquad , \tag{2.5}$$

where ε' and ε'' are the real part and imaginary part of the sample permittivity, respectively. C_0 is the empty cell capacity and can be calculated by $C_0 = \varepsilon_0 \cdot A/d$. A is the electrode area, d is the distance between the two electrodes and ε_0 (8.8542×10^{-12} F/m) is the vacuum permittivity. There is usually dielectric loss in the dielectric materials caused by the inherent dissipation of electromagnetic energy. The dielectric loss is described by the tangent of the dielectric loss angle, *tanδ* (Figure 2.6), which is defined as

$$tan\delta = \frac{\varepsilon''}{\varepsilon'} \qquad . \tag{2.6}$$
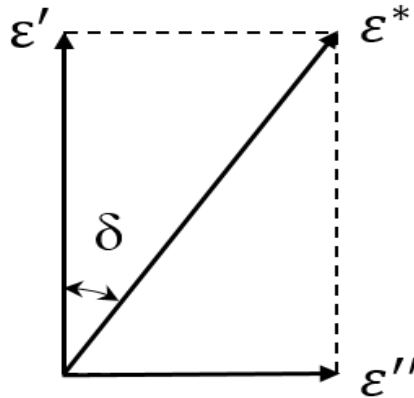
Figure 2.6.   Illustration of the dielectric loss angle δ with regard to the real part and imaginary part of permittivity.

2.3. Ferroelectric Hysteresis Measurements

The ferroelectric properties of the samples are revealed by the polarization versus electric field (P-E) loops. In this work, the ferroelectric property measurements are conducted using an RT66A Standard Ferroelectric Testing System (Radiant

Technologies Inc.). Figure 2.7 shows the schematic diagram of a modified Sawyer-Tower circuit (S-T circuit) used to measure the ferroelectric hysteresis loops. In the S-T circuit, the sample is connected in series with a resistor–capacitor circuit (RC circuit) which can compensate phase shift due to conductivity or dielectric loss in the sample. The capacitance of the reference capacitor C_r is far greater than that of the sample C_S. The capacitors in series have the same charge Q. During the experimental process, an alternating voltage V_{app} is applied across the two series capacitors through a function generator. Given that $Q = C_S V_S = C_r V_r$, $C_r \gg C_S$ and $V_{app} = V_S + V_r$, it is clear that $V_S \approx V_{app}$. The X- and Y- terminal of an oscilloscope read the (nowadays digital) values of V_{app} ($\approx V_S$) and V_r, respectively. Thus, with the sample thickness (d), area (A), the applied electric field E, and the polarization of the sample (P) can be determined by:

$$E = \frac{V_S}{d} \quad , \tag{2.7}$$

$$\text{and} \quad P = \frac{Q}{A} = \frac{C_r V_r}{A} \quad . \tag{2.8}$$

Knowing the above two values, the P-E loop can be displayed.
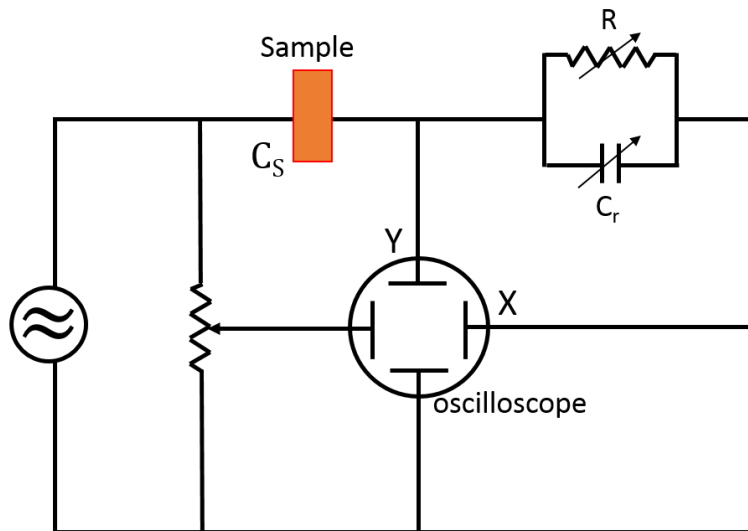
Figure 2.7.　　Schematic diagram of the modified Sawyer-Tower circuit for measuring the ferroelectric P-E loops.[14, 53]

2.4. Polarized Light Microscopy

Polarized Light Microscopy (PLM) is a useful technique to investigate the crystal symmetry, domain structure, and birefringence of ferroelectric single crystals. The instrument used here is an Olympus BX60 (Figure 2.9) with a Linkam HTMS600 heating/cooling stage. There are two polarizing components equipped in the PLM. One is the polarizer (P) placed underneath the sample stage and the other is the analyzer (A) installed above objective aperture. The polarization directions of the polarizer and analyzer are perpendicular to each other so no light can pass through the analyzer without any additional interference, which gives rise to a dark background in the observation tubes.
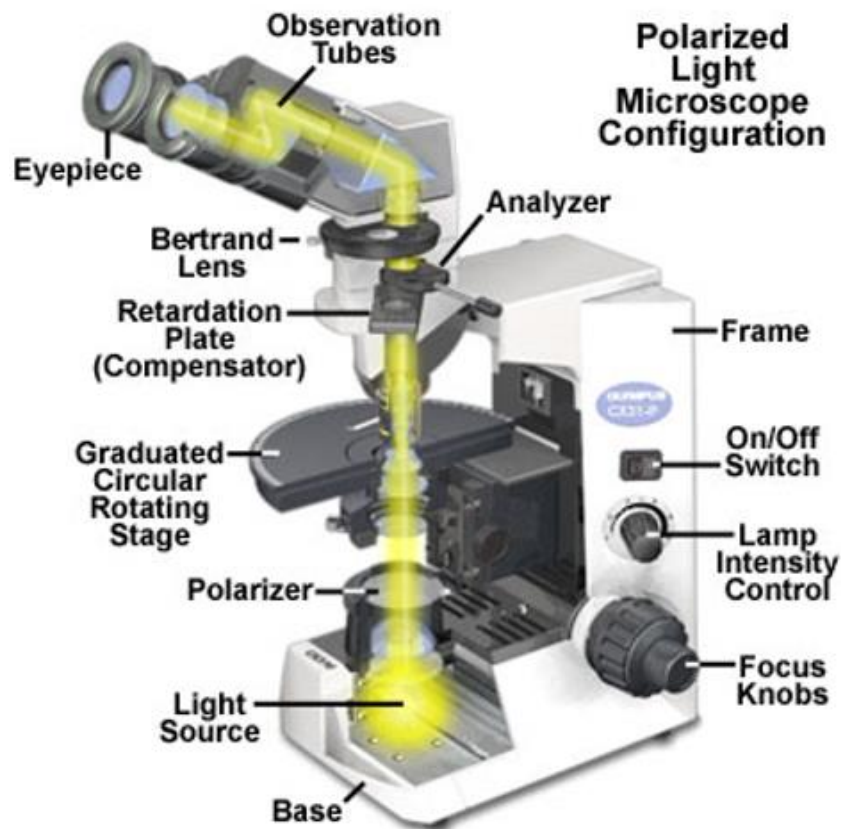
Figure 2.8.   Illustration of the Olympus BX60 polarized light microscope.[54]

For the isotropic single crystals, light has the same velocity (refractive index) in all orientations. For the anisotropic single crystals, there is a special direction known as the

optical axis governing the optical anisotropy. All other directions perpendicular to it are optically equivalent. When the incident light is not parallel to the optical axis, the light is doubly refracted by the anisotropic substance and splits into two polarized rays. The ray whose polarization is perpendicular to the optical axis is called the ordinary (*o*) ray, while the ray whose polarization is in the direction of the optical axis is called the extraordinary (*e*) ray.[55,56] The ordinary ray goes through the object in a straight line same as through an isotropic object, where the extraordinary is laterally displaced. Namely, the two part-rays have different velocities of propagation (refractive indices), giving rise to the retardation (R) between the faster and slower rays. The refractive indices of the extraordinary and ordinary rays are n_e and n_o, respectively. The difference between n_e and n_o is known as birefringence, defined as:

$$\Delta n = n_e - n_o \qquad (2.9)$$

The relationship between the retardation of light and birefringence follows the equation:

$$R = t \times \Delta n \quad , \qquad (2.10)$$

where t is the thickness of the crystal sample. PLM is capable of measuring the retardation and then one can obtain the value of birefringence using the above equation.

When a birefringent crystal is placed in a position where its optical axis is parallel to the analyzer or the polarizer, no light can enter the analyzer as the polarized light is blocked by either the sample or the analyzer. In this case, the crystal is in extinction under the microscope. When the birefringent crystal is situated at an angle θ to the polarizer, the light from the polarizer decomposes into two orthogonal rays – extraordinary and ordinary rays while it traverses through the crystal, as shown in Figure 2.9. The incident light propagates with θ degree to the optical axis of the sample. Thus, extraordinary ray and ordinary ray are at θ and 90° - θ degree to the polarizer, respectively. The two rays are out of phase because they both have different speeds. They therefore generate two light components D_1 and D_2 with different magnitudes ($D_1 \neq D_2$) after passing through the analyzer, giving rise to light intensity at the analyzer. The maximum light intensity is obtained when θ is 45° and the minimum intensity appears

when θ is 0°. The orientation of optical axis is dependent on the crystal symmetry. By determining the extinction angle of a crystal, one is able to deduce its crystallographic symmetry. For example, the optical axis in a tetragonal single crystal is along {100} orientations. A $(001)_{cub}$-orientated platelet of a tetragonal crystal is extinct when its $[100]_{cub}$ or $[010]_{cub}$ edge forms 45° to one of the polarizers. The detailed information on extinction angles for different symmetries can be found in Figure 2.10.

In this work, the optical retardation is measured using the Berek compensator while the crystal is at its brightest positions. The compensator is a calcite or magnesium fluoride optical plate which can be rotated to generate an additional phase shift in the polarized light passing through the crystal sample. It thus compensates and quantitatively determines the optical retardation of a crystal. Ferroelectric crystals of tetragonal or rhombohedral symmetry are uniaxial below Curie temperature T_C. Upon heating, the birefringence usually decreases upon heating within the ferroelectric phase due to the decreasing optical anisotropy. At T_C, the crystal transforms into an isotropic cubic phase and becomes extinct at all angles with respect to crossed polarizers. Investigations of the extinction angle and the temperature dependence of birefringence provide important information on structural symmetry and phase evolution of a ferroelectric/ferroelastic crystal.
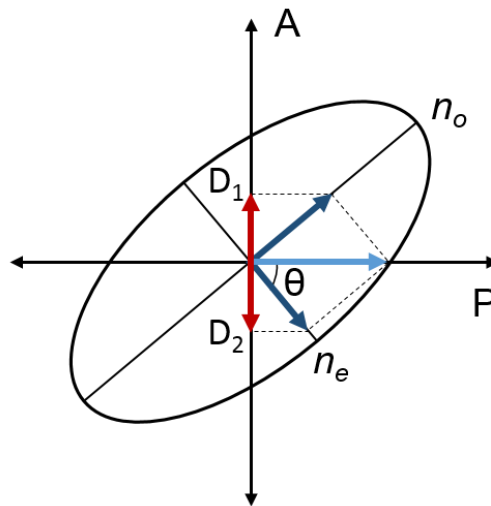
Figure 2.9.   The schematic diagram of the split and recombination of a light passing through a birefringent crystal. A and P stand for analyzer and polarizer, repesctively.
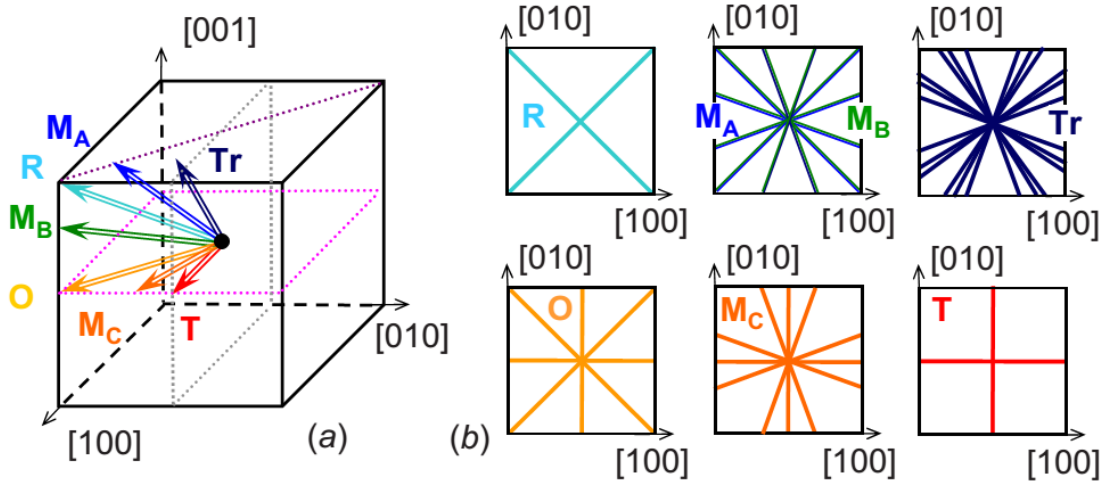
Figure 2.10. Illustration of various ferroelectric crystal symmetries: (a) spontaneous polarization (optical axis) directions with regard to cubic unit cell and (b) possible extinction positions in $(001)_{cub}$-orientated platelet.[57] Letters R, M, T, O, Tr stand for rhombohedral, monoclinic, tetragonal, orthorhombic and trigonal, respectively.

2.5. Synthesis Methods

Solid state materials can be synthesized through a variety of methods. Solids can be prepared in different forms including single crystals, ceramics, powder, nanoparticles and so forth. The primary synthesis method used in this work is the conventional solid state reaction method.

The solid state reaction method is one of the most widely used methods for the synthesis of polycrystalline materials. Firstly, the powder reactants are mixed and ground with a moderate amount of volatile organic liquid added to facilitate the homogeneity of the reactant mixture. The mixed powder is then pressed into pellets or some other shape before being processed in a heat treatment.

A solid state reaction typically takes several complex steps. The formation of $MgAl_2O_4$ spinel from MgO and Al_2O_3 oxides is taken as an example to explain the reaction process. $MgAl_2O_4$ forms at the interface between the grains of MgO and Al_2O_3 oxides at the beginning because the reagents at the interface are in contact with each other. This step is known as nucleation of the reaction.[8] The nuclei of $MgAl_2O_4$ must grow

31

to a critical size when the negative free energy inside the nuclei and the positive surface energy of the nuclei are balanced. Otherwise, the nuclei are unstable and tend to degenerate. The nuclei of the products can form on top of the surface of a reactant (considered as a substrate). In this case, nucleation of $MgAl_2O_4$ can occur on either an MgO or an Al_2O_3 structure, as shown in Figure 2.11. Because the structures of MgO and $MgAl_2O_4$ are both cubic close packed (*ccp*), the oxygen arrangement can be maintained, while assuming the nuclei of $MgAl_2O_4$ and MgO are in the same crystallographic direction. Similarly, nuclei form at the suitable-orientated $Al_2O_3/MgAl_2O_4$ interface. However, the oxide ions in Al_2O_3 are hexagonal close packed (*hcp*), which is different from that of the spinel $MgAl_2O_4$. Therefore, oxygen stacking sequence must transform from *hcp* to *ccp* during the nucleation. In the next stage, counter-diffusion process is necessary to the continuous growth of products since the $MgAl_2O_4$ nuclei separate the two reactants. In this process, Al^{3+} ions diffuse from, and Mg^{2+} ions diffuse to, the $Al_2O_3/MgAl_2O_4$ interface. And vice versa for the $MgO/MgAl_2O_4$ interface (Figure 2.12). The speed of diffusion is different for the two interfaces because the ratio of diffused Mg^{2+} to Al^{3+} ions should maintain 3:2 ratio to preserve local electroneutrality during the reaction. Considering that ions diffuse very slowly, high temperature treatment is normally required to enhance the speed of diffusion of ions.
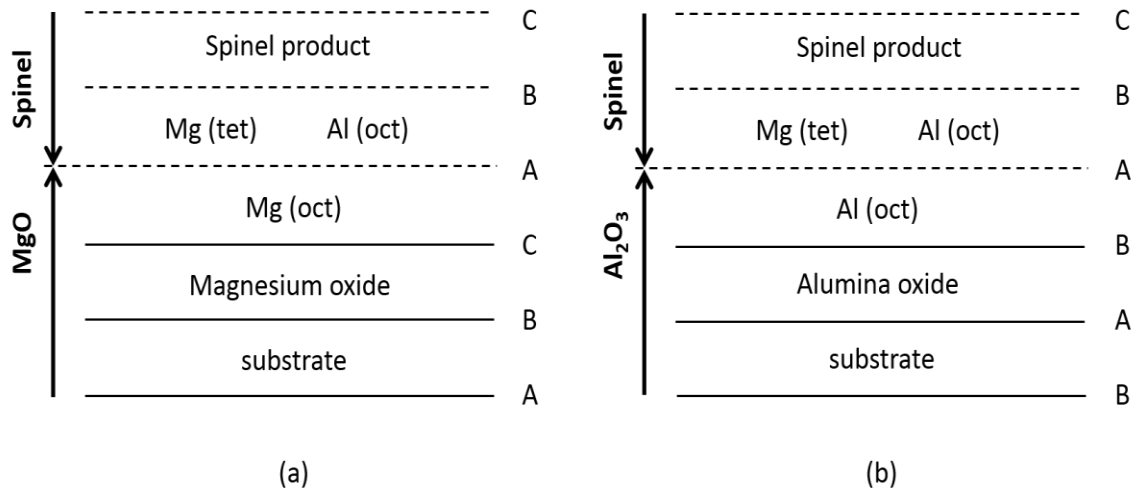
Figure 2.11.   Nucleation of $MgAl_2O_3$ spinel on an (a) MgO and (b) Al_2O_3 substrate. Letters A, B and C indicate the close packing arrangement of the oxide ions.[8]
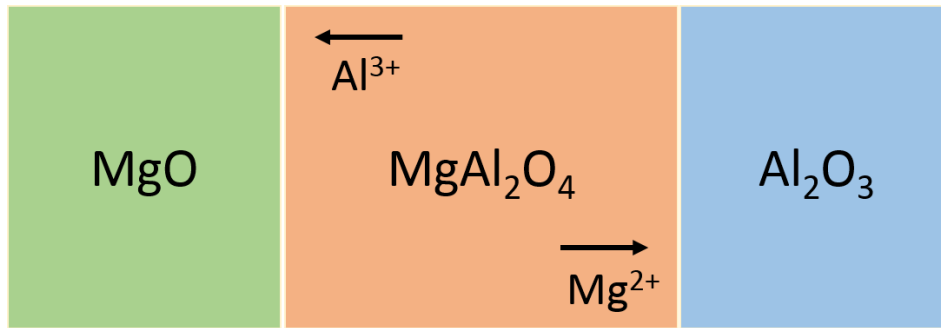
Figure 2.12. Demonstration of the diffusion directions of Mg^{2+} and Al^{3+} ions in the situation that MgO and Al_2O_3 grains are separated by the product nuclei of $MgAl_2O_4$.

Chapter 3.

Growth and Characterization of Ferroelectric Pb(Sc$_{1/2}$Nb$_{1/2}$)O$_3$ Single Crystals

3.1. Abstract

Single crystals of Pb(Sc$_{1/2}$Nb$_{1/2}$)O$_3$ were grown by the high-temperature solution method using (PbO + B$_2$O$_3$) as a flux. The size of the as-grown crystals varies from 1 to 2 mm. X-ray diffraction indicates a pure perovskite phase without B-site ordering. Polarized light microscopy shows that the crystals are of rhombohedral symmetry at room temperature and become cubic at Curie temperature T_C = 112 ^{o}C on heating. A ferroelectric-to-relaxor phase transition is verified at T_C by dielectric spectroscopy. Frequency-dependent permittivity is observed in dielectric measurements, revealing relaxor behavior above T_C. Poling the crystal at room temperature does not change T_C but suppresses the permittivity. A typical ferroelectric hysteresis loop is displayed at room temperature, indicating the ferroelectric nature of the PSN crystal.

3.2. Introduction

Relaxor ferroelectrics were discovered almost 60 years ago. There has been an enormous growth of interest in the topic of relaxor materials over the past 20 years. Relaxors exhibit high dielectric permittivity and peculiar dielectric properties [18, 19], which makes them of great potential for high dielectric capacitors, probes and sensors.[58, 59] On cooling, unlike normal ferroelectrics which experience structural phase transition from the paraelectric (PE) to ferroelectric (FE) phase at the Curie temperature (T_C), relaxor ferroelectrics show the transitions over a broad temperature range, from the PE to the ergodic relaxor (ER) state and then to either the non-ergodic relaxor (NR) or the FE state.[18] In the ER state polar nanoregions (PNRs) are randomly distributed, which

contributes to the frequency dispersion of dielectric properties. The maximum in the temperature dependence of dielectric permittivity is observed in the ER phase whose temperature, T_m, increases with increasing frequency. Below the transition temperature the canonical relaxors such as $Pb(Mg_{1/3}Nb_{2/3})O_3$ (PMN) are in the NR state and the FE phase only exists after the application of external electric field.[35] On the other hand, $Pb(Sc_{1/2}Nb_{1/2})O_3$ (PSN) undergoes a spontaneous transition from an ER state to a FE state.[32]

PSN belongs to the $Pb(B_{1/2}B'_{1/2})O_3$-type complex perovskites with two different B cations in a 1:1 ratio. This material is interesting because thermal treatment can alter the degree of B-cation ordering and thus influence the properties.[10, 24, 60-62] For example, fully compositionally ordered PSN ceramics show typical FE behavior, while disordered ceramics demonstrate relaxor behavior.[32] Disordered PSN undergoes a spontaneous transition from the relaxor to the FE state upon zero-field cooling (ZFC). In partially disordered PSN, locally ordered regions can be detected.[61] In the FE state the disordered PSN is of rhombohedral symmetry belonging to the space group of $R3m$ with the room-temperature pseudocubic unit cell parameters a_{pc} = 4.080(1) Å and α = 89.89(1) °.[63-66] Recently, PSN single crystals have been grown by a high temperature solution method using PbO and B_2O_3 as a flux.[30] Sharp order-disorder type FE phase transition was suggested to take place in the PSN single crystal where PNRs in the ER state perform as ordering units. Ferroelectric interaction between PNRs leads to FE macroscopic order.[34] In the FE state, PSN retains some relaxor character.[37] Hydrostatic pressure tends to suppress the FE correlations of PNRs, while dc biasing electric field strengthens the dipole interactions, giving rise to the formation of large FE domains.[67] To date, only a few studies have been reported on PSN single crystals probably due to the difficulties in growing the crystals. As the properties of crystals can vary significantly by growth conditions, PSN single crystals, in this work, were grown using a flux to charge ratio different from that in previous work.[30] The poling effect on the dielectric properties of the as-grown PSN crystals is investigated.

3.3. Experimental

The PSN single crystals were grown by the high-temperatue solution method using PbO and B_2O_3 (8:1) as a flux. The starting materials, PbO_2 (99.9%), Sc_2O_3 (99.9%) and Nb_2O_5 (99.9%), were mixed stoichiometrically for the following chemical reaction: $4PbO_2 + Sc_2O_3 + Nb_2O_5 \rightarrow 4Pb(Sc_{1/2}Nb_{1/2})O_3$. The mole ratio between flux and charge was 5:2. The oxide mixture was put into a 50-mL platinum crucible and placed into a large sealed platinum crucible in order to prevent the evaporation of PbO. The crystals were grown in a cylindrical furnace with an automatic temperature controller. It was first heated up to 1100 °C at a rate of 250 °C/h and then soaked for 24 hours. After that, it was gradually cooled down to 900 °C at 0.2 °C/h, then to room temperature by 35 °C/h. Finally, crystals were obtained by leaching the flux in a 10% HNO_3 solution. The dimensions of the as-grown crystals were of 1-2 mm. A small amount of crystals were ground into powder to study the crystal structure using a Bruker D8 X-ray diffractometer with Cu Kα radiation. Several crystals were cut and polished parallel to the $(001)_{cub}$ crystallographic faces for optical observation, dielectric measurements and FE measurements. The domain structure was investigated on an Olympus BX60 Polarized Light Microscope equipped with an Olympus UC 30 digital camera and a Linkham (THMS600) heating stage. The dielectric properties were measured on a Novocontrol broadband dielectric analyzer equipped with a high temperature furnace. The polarization versus electric field (P-E) loops were displayed by an RT-66 ferroelectric test system (Radian Technology). With the intention of investigating the poling effect on PSN single crystals, a $(001)_{cub}$-orientated PSN crystal platelet was poled under a field of 30 kV/cm for 20 minutes at room temperature and the dielectric properties were measured subsequently.

3.4. Results and Discussions

3.4.1. Structural Analysis

The XRD pattern of the PSN is shown in Figure 3.1 which indicates a pure perovskite phase. No (1/2 1/2 1/2) peak appears, suggesting the compositionally disordered system. No obvious splits are observed at any peaks in Figure 3.1, but the $(111)_{pc}$ reflection is slightly asymmetric and broadened as compared to the $(100)_{pc}$

reflection (Figure 3.2). This indicates a rhombohedral unit cell that is subtly distorted from a cubic unit cell. Structural Rietveld refinement was performed under $R3m$ model. The resulting parameters are a = 4.0811(6) and α = 89.88(3)°.
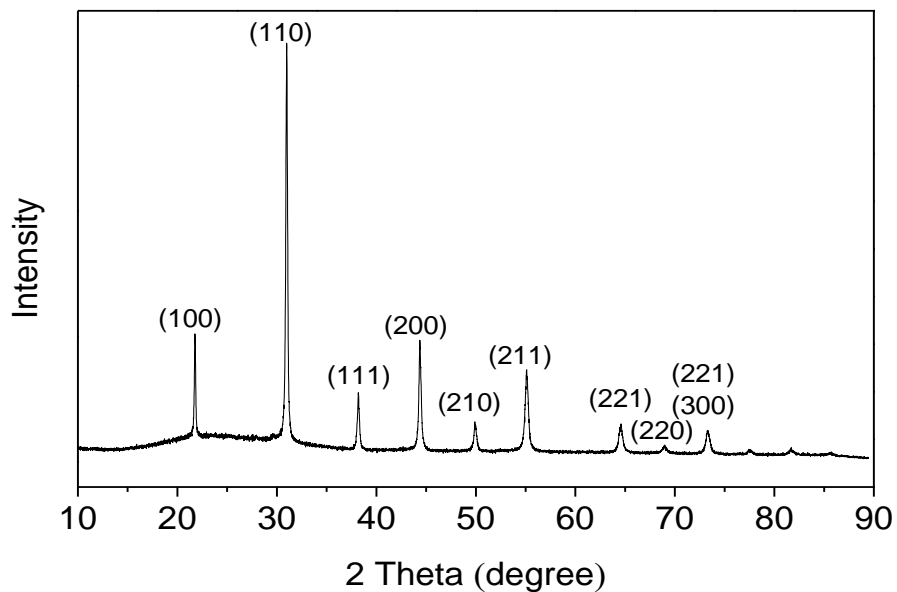
Figure 3.1.   XRD pattern of the as-grown PSN single crystals (ground powder).
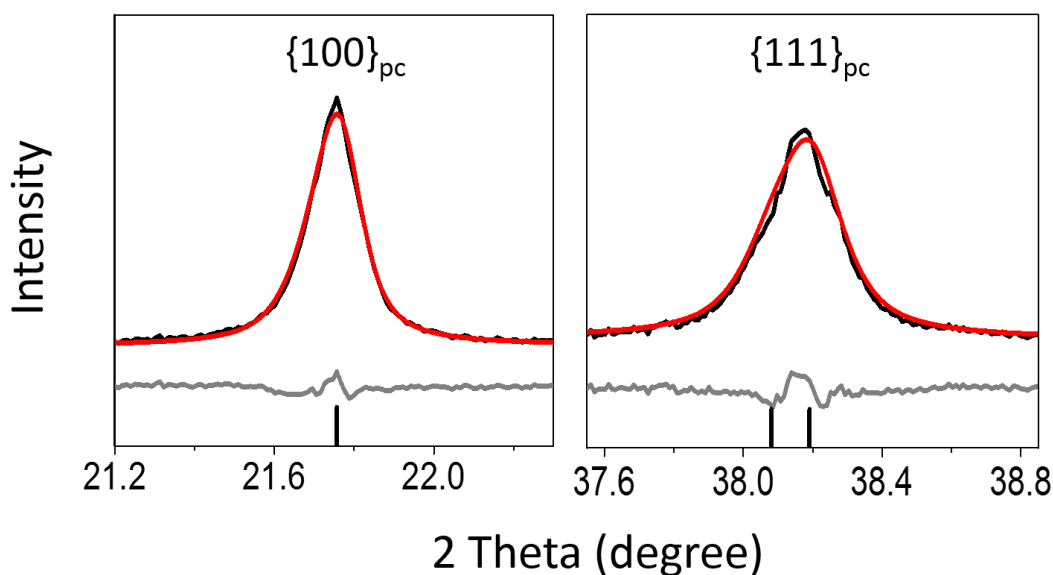
Figure 3.2. Refined profiles of $(100)_{pc}$ and $(111)_{pc}$ reflections. The black, red and grey lines are the experimental data, refined result and the difference between them, respectively. The black ticks are refined results indicating the peak positions.

3.4.2. Domain Structure and Phase Transition

Figures 3.3a - 3.3d displays the domain structure of a 30 µm thick (001) PSN crystal platelet. The optical observations were performed with the crossed polarizers parallel to, and at 45° to, the [100] direction. At room temperature, the platelet consists of a number of fine birefringent domains, representing a macrodomain state (Figure 3.3a). The crystal platelet is in extinction with an angle of 45° to the crossed polarizers (Figure 3.3b), consistent with the rhombohedral symmetry.[57] Upon heating to 112 °C, most domain walls vanish rapidly and most areas of the platelet are in full extinction at any angle to the crossed polarizers (Figs. 3.3c and 3.3d). This indicates a structural transition from the rhombohedral phase to the isotropic cubic phase. Upon cooling through 110 °C, birefringent domains start to show up again and the domain structure pattern at room temperature looks almost the same as that present before heating.
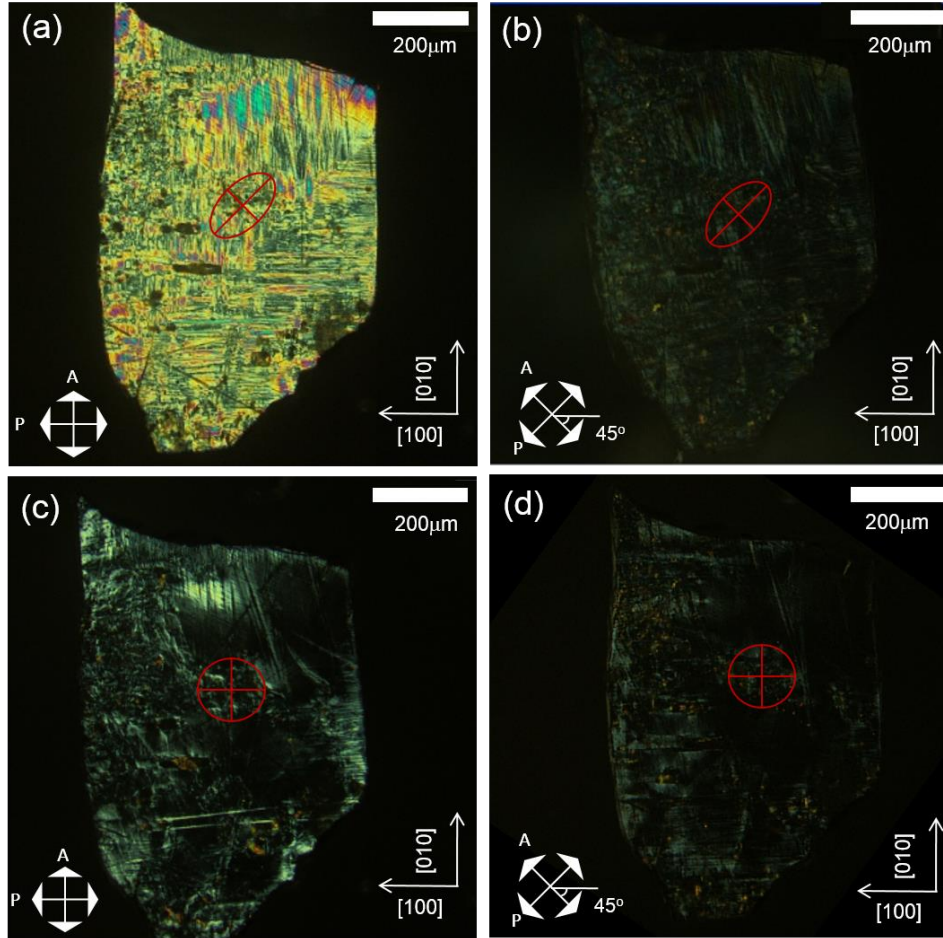
Figure 3.3.   Domain structures of PSN crystal platelet on the (001)-orientated platelet at (a, b) 25 °C and (c, d) 112 °C on heating.

The temperature dependence of birefringence on heating and cooling is shown in Figure 3.4. The birefringence is examined from the optical retardation determined at a central spot on the crystal platelet with a large domain. It is noticeable that no birefringence is detected above 112 °C on heating and 110 °C on cooling, suggesting that above these temperatures the crystal is in isotropic cubic phase. The discontinuous change at T_C and the observation of thermal hysteresis (~2 °C) reveal the first-order phase transition. Observation of the first-order phase transition in PSN system was reported in the variation of lattice constants as a function of temperature by Malibert et al.[61]
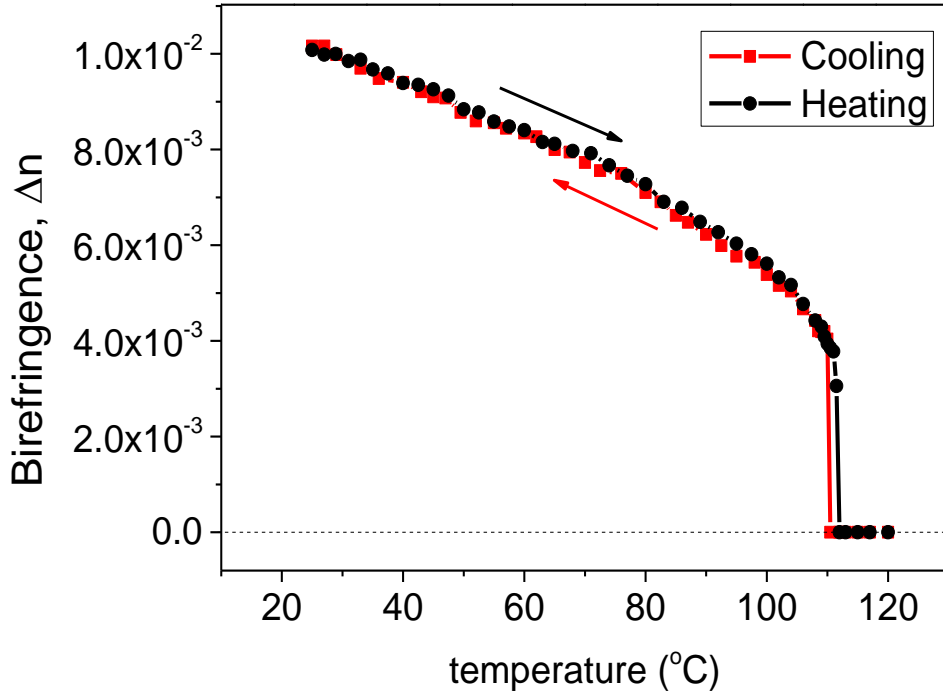
Figure 3.4. Temperature dependence of the birefringence on the (001) platelet
of an as-grown PSN single crystal.

3.4.3. Electrical Properties

The dielectric properties of PSN crystal was measured at varying frequencies (10^3 - 10^6 Hz) on heating and cooling, as presented in Figure 3.5. The crystal shows relaxor behavior with diffuse and broad peaks and frequency dispersion above T_C. Broad phase transition peaks result from the thermally activated reorientation of dipole moments of PNRs and the motion of PNR boundaries.[68-71] With decreasing frequencies T_m drops from ~130 °C to ~120 °C. These phenomena are generally observed in relaxor systems. Comparing with the work done by Bing et al., the PSN single crystals in this work exhibit a lower maximum permittivity, ε'_m, but at higher T_m. It means these two differently grown PSN crystals can have different degree of B-cation ordering and/or different amount of lead vacancies which are two factors affecting the system properties.[32, 33]

The dispersive T_m measured on both heating and cooling was fitted to the Vogel-Fulcher (V-F) law:

$$f = f_o \exp\left(\frac{-E_a}{T_m - T_o}\right) \quad , \tag{3.1}$$

where f is the frequency, f_o, E_a and T_o are fitting parameters. Figure 3.6 demonstrates that the V-F law satisfied by the experimental data measured on cooling, verifying the relaxor FE behavior. The resulting parameters are $f_o = 3.1(3) \times 10^{15}$ Hz, $E_a = 0.140(1)$ eV and $T_o = 63(1)$ °C. The ε'(T) dependence obeys a quadratic law at the temperature range between 150 °C and 200 °C (Figure 3.7):

$$\frac{\varepsilon_A}{\varepsilon} = 1 + \frac{(T - T_A)^2}{2\delta_A^2} \quad . \tag{3.2}$$

where T_A ($<T_m$) and ε_A ($>\varepsilon_m$), are fitting parameters defining the temperature and magnitude of the Lorenz peak, respectively. And δ is a measure of the degree of diffuseness of the peak.[26] The resulting parameters are as follows: $T_A = 2.0(1) \times 10^4$, $\varepsilon_A = 100.3(4)$ and $\delta = 31.4(1)$. The fit to the quadratic law further confirms that the PSN single crystals exhibit relaxor behavior.

The dielectric constant of the sample poled at room temperature was measured on zero-field heating (ZFH1), followed by subsequent zero-field cooling (ZFC) and heating (ZFH2). Figure 3.8 shows the temperature dependence of dielectric constants of the poled sample during ZFH1 at various frequencies. It is obvious that the dielectric maximum (ε'_m) and its temperature (T_m) are also frequency-dependent. The relationship between T_m and frequencies satisfies the V-F law, which means the poled PSN crystal still possesses the relaxor character. The resulting fitting parameters are $f_o = 5.2(3) \times 10^{10}$ Hz, $E_a = 0.037(3)$ eV and $T_o = 94(2)$ °C. Interestingly, an anomaly appears at about 180 °C.
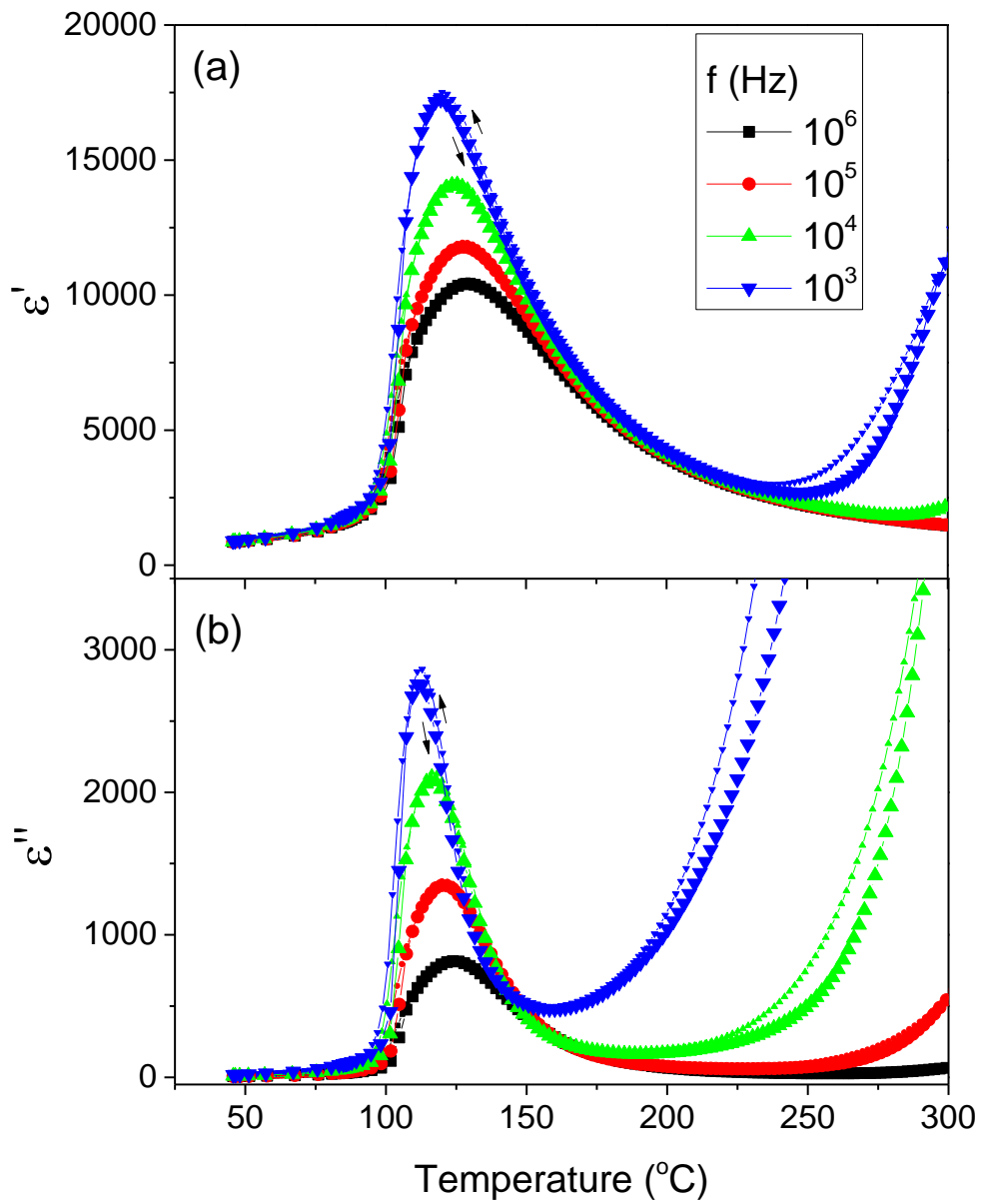
Figure 3.5. Temperature dependences of (a) the real part (ε') and (b) imaginary part (ε'') of dielectric constants measured on the (001)-orientated PSN crystal platelet between 10^3 Hz and 10^6 Hz upon heating and cooling.
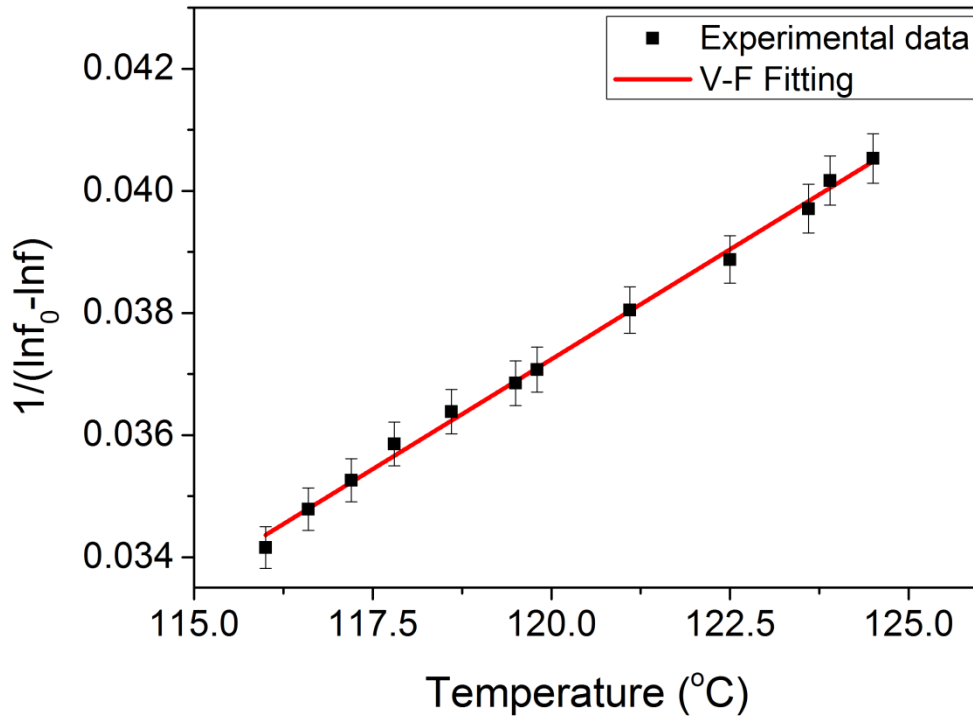
Figure 3.6. Vogel-Fulcher fitting of the real part of dielectric constant measured on cooling.
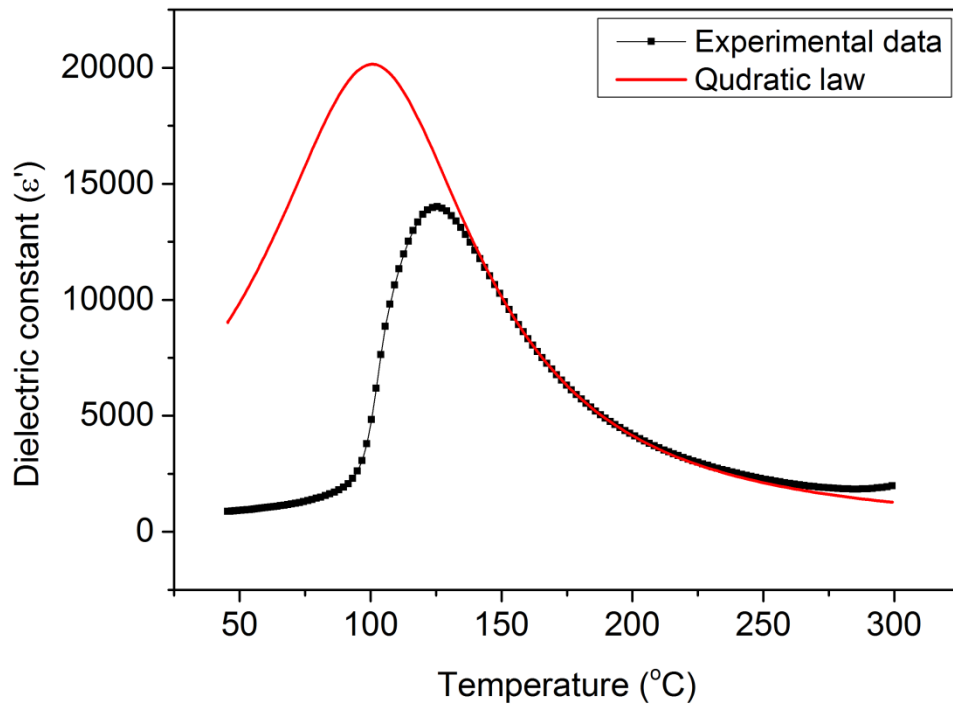
Figure 3.7.   Quadratic law fitting based on the real part of dielectric constant (ε')
at 10^4 Hz on cooling.
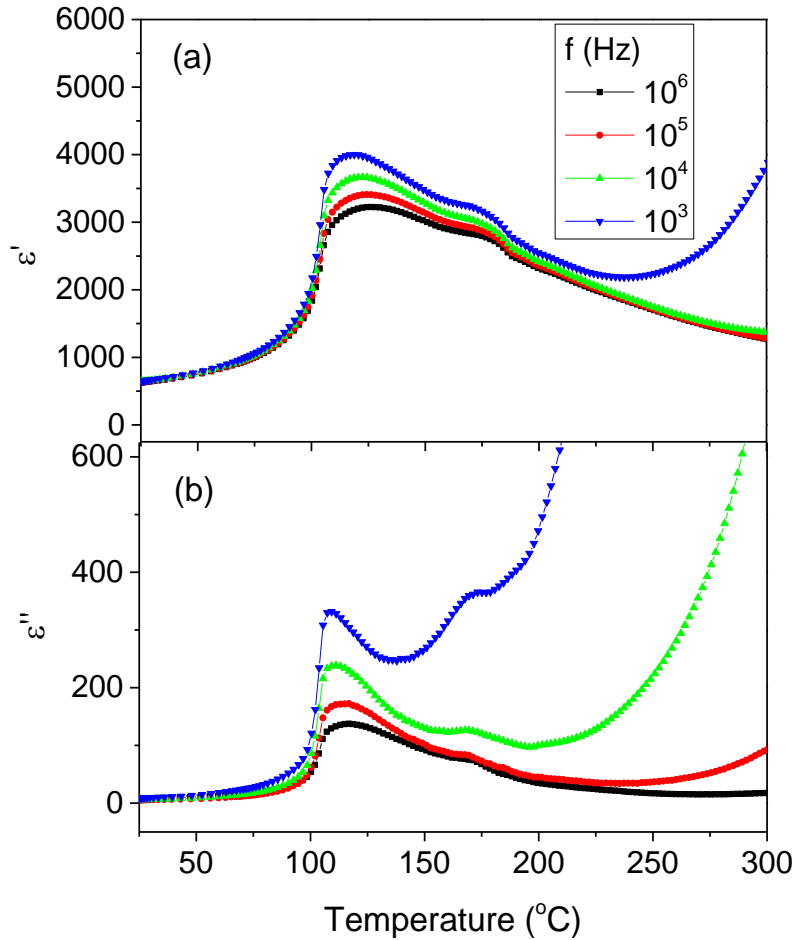
Figure 3.8. Temperature dependences of the (a) real part (ε') and (b) imaginary part (ε") of dielectric constant measured on the poled (001)-orientated PSN crystal platelet at 10^3 Hz to 10^6 Hz on heating.

The dielectric maxima ε'_m observed on ZFH1 are much lower than those observed on ZFC and ZFH2 (Figure 3.9). Though PSN is macroscopically ferroelectric at room temperature, it still exhibits some relaxor features.[37] The FE phase of PSN can be caused by the macroscopically ordered FE interaction between PNRs.[36] Therefore, poling PSN crystals at room temperature can generate two possible results. First, the poling field enhances the ferroelectric ordering within the crystal and therefore suppresses the concentration of PNRs and their boundary areas, leading to a decrease in permittivity. Second, poling the sample at room temperature causes some dynamic PNRs in the ER phase to grow larger and, thereby, static, consequently decreasing the dielectric permittivity on the first ZFH run. At high temperature (much above T_C) the poled

sample becomes depoled, and the permittivity increases on ZFC and ZFH2 as the field-induced static PNRs are released and become dynamic again, recovering the values and shape of the permittivity-temperature curves of the initial (un-poled) PSN crystal. It is possible that the dielectric anomaly around 180 °C is associated with the depoling process.
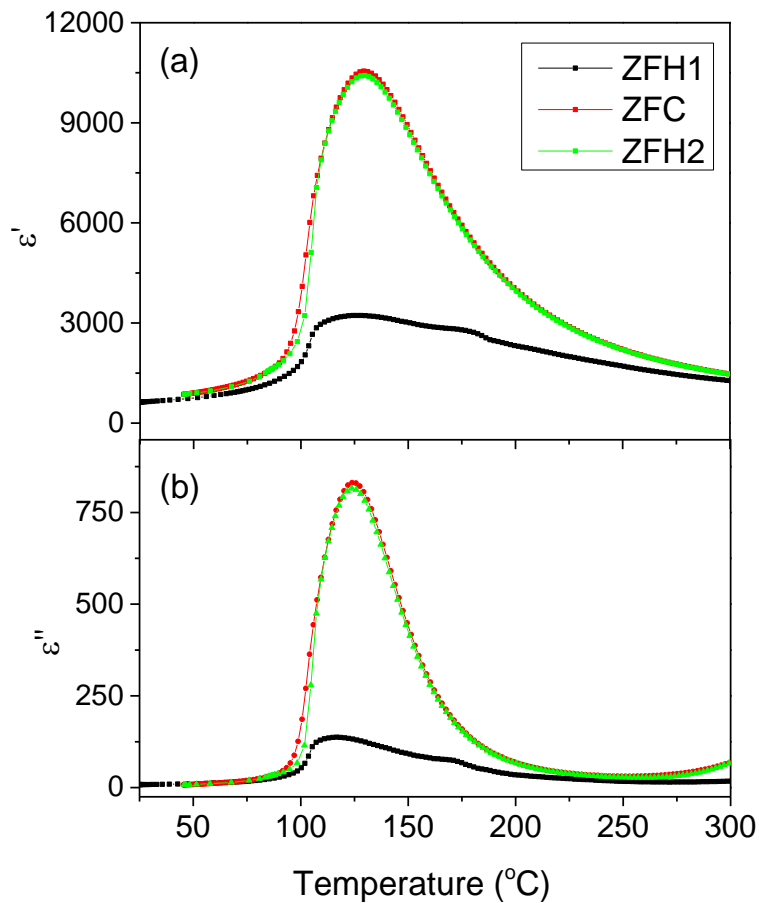
Figure 3.9.   Temperature dependences of (a) the real part (ε') and (b) imaginary part (ε'') of dielectric permittivity of the poled (001) PSN platelet at 10^6 Hz on zero-field heating (ZFH1, black), followed by subsequent zero-field cooling (ZFC, red) and heating (ZFH2, green).

A typical ferroelectric polarization-electric field (P-E) loop is obtained at room temperature and is displayed in Figure 3.10. A maximum electric field of ± 20 kV/cm is used. The coercive field (E_C) is about 5.8 kV/cm and the remnant polarization (P_r)

reaches ± 11.3 µC/cm^2. The FE hysteresis loop reveals the macroscopically FE nature of the PSN crystals below T_C.
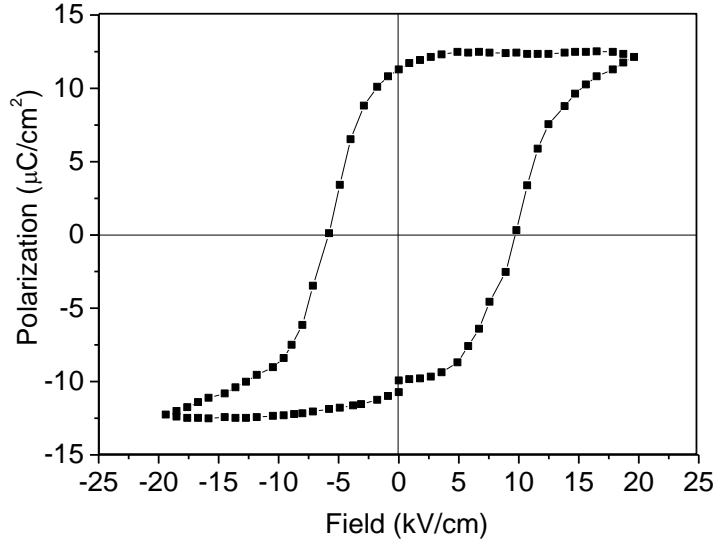
Figure 3.10.   Polarization versus electric field (P-E) hysteresis loop of the (001)-oriented PSN crystal platelet at 25°C.

3.5. Conclusions

PSN single crystals were successfully grown by the high-temperatrue solution method with a flux-charge mole ratio of 5:2. XRD pattern shows a pure perovskite structure without indication of B-site ordering. Optical observation indicates the PSN crystal is of rhombohedral structure. A first-order phase transition between rhombohedral and cubic symmetry was observed based on the discontinuous variation of birefringence measurement. Dielectric measurements revealed a ferroelectric-to-relaxor transition upon heating. The temperature dependence of the dielectric constant obeys the quadratic law, and the relationship between frequency and T_m follows the V-F law, which all suggest relaxor behavior existing in the PSN single crystals. Poling the crystal at room temperature does not change T_C but decreases the permittivity. The possible reason for the decrease of permittivity is that a sufficiently high external field can increase the size of PNRs, reducing their contribution to the permittivity. A dielectric anomaly was observed in the pre-poled sample at around 180 ^{o}C which could be caused by the transformation in the PNRs subsystem. The sample can be depoled at high temperature above T_C and

47

dielectric constant restores as a result. A typical FE hysteresis loop was displayed at room temperature, suggesting the FE nature of the low-temperature phase.

Chapter 4.

Study of A New Antiferroelectric Solid Solution of PbZrO$_3$-Pb(Zn$_{1/2}$W$_{1/2}$)O$_3$

4.1. Abstract

A new antiferroelectric solid solution of (1-x)PbZrO$_3$-xPb(Zn$_{1/2}$W$_{1/2}$)O$_3$ [(1-x)PZ-xPZnW, with x = 0 - 10%] has been prepared in the form of ceramics by conventional solid state reaction method. X-ray powder diffraction (XRD) reveals the perovskite structure of the (1-x)PZ-xPZnW ceramics. The lattice parameters a_{pc} and b_{pc} of the ceramics reduce more significantly than c_{pc} with increasing concentration of PZnW. These variations of lattice constants as a function of composition indicate the formation of solid solution. The Curie temperature (T$_C$) decreases from 228 ^{o}C to 195 ^{o}C when the percentage of PZnW increases from 0% to 10%. Meanwhile, another transition related to the transformation from antiferroelectric (AFE) to an intermediate ferroelectric (FE) phase was observed and its transition temperature (T$_{AFE-FE}$) was found to shift from 213 ^{o}C for x = 0 to 58 ^{o}C for x = 0.10. A typical ferroelectric hysteresis loop was displayed, indicating the FE nature of the intermediate phase.

4.2. Introduction

Recently, research on antiferroelectric (AFE) materials has received great interest because of their potential applications in high performance energy storage devices and microelectromechanical systems (MEMS) .[72-74] The basic physics of these applications is that the field-induced ferroelectric (FE) phase existing in AFEs leads to the enhanced effective energy density compared with paraelectrics (PEs) and FEs.[75] The most widely used and well known AFE material is the perovskite compound of PbZrO$_3$ (PZ). It has been extensively studied since 1950s.[38,76] PZ has an orthorhombic superlattice that

belongs to the *Pbam* space group. The dimensions of the superlattice are $a_o = \sqrt{2}a_{pc}$, $b_o = 2\sqrt{2}\,a_{pc}$, and $c_o = 2c_{pc}$, which is composed of eight pseudocubic unit cells with lattice parameters a_{pc} and c_{pc}.[39, 40] The antiferroelectric properties of PZ arise from the antiparallel displacements of Pb^{2+} along the pseudocubic $[1\ 1\ 0]_{pc}$ direction.[40, 77] The Curie temperature (T_C) of PZ is around 233 ^{o}C.[38] Between the room-temperature AFE phase and the high-temperature (above T_C) PE phase, there is a possible intermediate FE phase within a very narrow temperature range (225 - 230 ^{o}C) [41], which was first discovered by in a PZ single crystal.[41] However, since the critical field (E_F) for the field-induced FE state of PZ, around 220 kV/cm for high quality single crystals[78], is always far above its breakdown field at room temperature, chemical modifications are needed to improve its properties. Through substitutions using Ba^{2+}, La^{3+}, Ti^{4+}, Sn^{4+}, and Nb^{5+} ions [79-83] or forming solid solutions with $Pb(Mg_{1/2},W_{1/2})O_3$ (PMgW) [46, 73, 84], $Pb(Zn_{1/3}Nb_{2/3})O_3$ [85] and $Pb(Ni_{1/3}Nb_{2/3})O_3$ [86] or some other end-members, the physical and electrical properties of PZ can be improved and the temperature range of the possible intermediate phase can be enlarged. The reason for the expansion of the intermediate FE phase is assumed to be the interaction/competition between FE and AFE orderings that generates an incommensurate structural modulation. The quenched dopant can produce a reduction in the free energy barrier between AFE and FE phases and thus destabilizes the AFE coupling.[80, 87, 88] Consequently, the transition between the AFE and the intermediate FE phase occurs at lower transition temperature (T_{AFE-FE}), expanding the temperature range of the intermediate phase. These incommensurate states have been observed in the La- and Sn-modified PZ systems.[80, 89, 90]

$Pb(Zn_{1/2}W_{1/2})O_3$ (PZnW) is a complex perovskite with ordered Zn^{2+} and W^{6+} on the B-site of the perovskite ABO_3 lattice.[91] Though pure PZnW has not yet been synthesized using conventional solid state reaction method,[92] it can be stabilized by forming solid solutions with other perovskite compounds, such as $Pb(Zn_{1/2}W_{1/2})O_3$–$Pb(Zr_{0.5}Ti_{0.5})O_3$.[93,94] PZnW is predicted to be AFE [95] and has an identical stoichiometry and structure to PMgW.[92] In the PMgW system, Pb^{2+} ions antiparallelly shift along $<100>_{pc}$ and $<010>_{pc}$ directions, giving rise to a net zero polarization.[96] It is highly expected that the origins of antiferroelectricity in PZnW and PMgW are similar, which is different from the type of AFE ordering in PZ. Therefore, it is interesting to investigate whether this difference in AFE orderings can enlarge the temperature window of the intermediate phase and affect the

properties of PZ. Meanwhile, PZ-based solid solutions are primarily formed by FE end-members to date, so solid solutions with an AFE as end-member are also worthy to explore. In this Chapter, the influence of $Pb(Zn_{1/2}W_{1/2})O_3$ on the phase formation structure, and dielectric and antiferroelectric properties of $PbZrO_3$ are studied.

4.3. Experimental

The solid solution of $(1-x)PbZrO_3-xPb(Zn_{1/2}W_{1/2})O_3$ [(1-x)PZ-xPZnW, with x = 0% - 10%] was prepared by a two-step solid state reaction method. The precursor phase, $ZnWO_4$, was first synthesized from ZnO and WO_3 powders (purity >99%) at 1000 ℃ for 12 hours. The pre-formed precursors and the stoichiometric amounts of ZrO_2 and PbO were then mixed and ball-milled in ethyl alcohol for 24 hours with 1 mol% PbO excess to compensate for the lead oxide evaporation. The mixture of powders was calcined at 880 ℃ for 4 hours after being dried. The as-calcined powder was ground and ball-milled again overnight and then pressed into pellets for sintering. In order to obtain dense ceramics, 1 wt% polyvinyl alcohol binder was added. The sintering process was carried out at 1000 ℃ for 2 - 2.5 hours. X-ray powder diffraction (XRD) was performed with Cu *Kα* radiation on the Bruker D8 Diffractometer to investigate the purity and crystal structure of the sintered ceramics. The temperature dependence of dielectric permittivity was measured on a Novocontrol Alpha high resolution broadband dielectric analyzer equipped with a high-temperature furnace. The Strata235 Dual beam SEM/FIB was utilized to study the morphology of samples with different compositions. The (anti-)ferroelectric properties were measured by an RT-66 ferroelectric test system (Radian Technology).

4.4. Results and Discussion

4.4.1. Phase Formation

Figure 4.1 shows the X-ray diffraction patterns of the (1-x)PZ-xPZnW solid solution, which are indexed according to the basis of the orthorhombic unit cell. The 1/4 (h k l) - type superlattice reflections, such as (1 3 0 / 1 1 2) and (2 1 0) reflections, represent the antiparallel tilting of the oxygen octahedra without distortion.[48] It is clear that

the XRD patterns of all compositions match the Standard X-ray Diffraction Powder Patterns (PDF) card No. 87-564 of PbZrO$_3$ in the *Pbam* space group, indicating the orthorhombic symmetry of the PZ end member is preserved in the solid solution. When the concentration of PZnW reaches 6%, a secondary phase appears, as indicated by the peaks labeled with stars. This secondary phase is identified to be Pb(Zr$_{1.34}$W$_{0.66}$)O$_{6.5}$ whose PDF card (No. 17-0487) matches the peak positions of the impurity phase. However, the appearance of impurity is not an indicator of solubility limit because the properties of the system still change when x is greater than 6%. The impurity could be formed during the high temperature sintering process.

In order to study the crystal structure of the (1-x)PZ-xPZnW solid solution, the Rietveld refinements were carried out using TOPAS Academic software. The crystal structure of different compositions was all refined based on the *Pbam* model. The fitting results are listed in Table 4.1. The orthorhombic lattice parameters a_o, b_o and c_o are all converted to the pseudocubic parameters, a_{pc} (= b_{pc}) and c_{pc}, using the following equations:[97, 98]

$$a_{pc} = b_{pc} = \frac{1}{2}\sqrt{a_o^2 + \left(\frac{b_o}{2}\right)^2} \quad , \tag{4.1}$$

$$c_{pc} = \frac{1}{2}c_o \quad . \tag{4.2}$$

The variations of the lattice parameters a_{pc} and c_{pc} as a function of compositions are shown in Figure 4.2. Both a_{pc} and c_{pc} decrease when x increases. This downward trend in lattice constants seems to stop at x = 8% which could be indicative of the solubility limit of PZnW into PZ. The change of lattice parameters reflects the effect of the PZnW substitution on the PZ structure, confirming the formation of the (1-x)PZ-xPZnW solid solution. The decrease of lattice parameters is, to some extent, due to the fact that the average radius of Zn^{2+} (0.74 Å) and W^{6+} (0.60 Å) is slightly smaller than the radius size of Zr^{4+} (0.72 Å).[99] In addition, the magnitude of antiparallel displacements of Pb^{2+} can be lessened since the room for Pb^{2+} to displace is reduced by the contraction of the pseudocubic unit cells. Thus, the antiferroelectric phase becomes less stable with

increasing concentration of PZnW. The influence of PZnW on the structure of PZ ceramics is similar to that of $Pb(Mg_{1/2}W_{1/2})O_3$.[100]
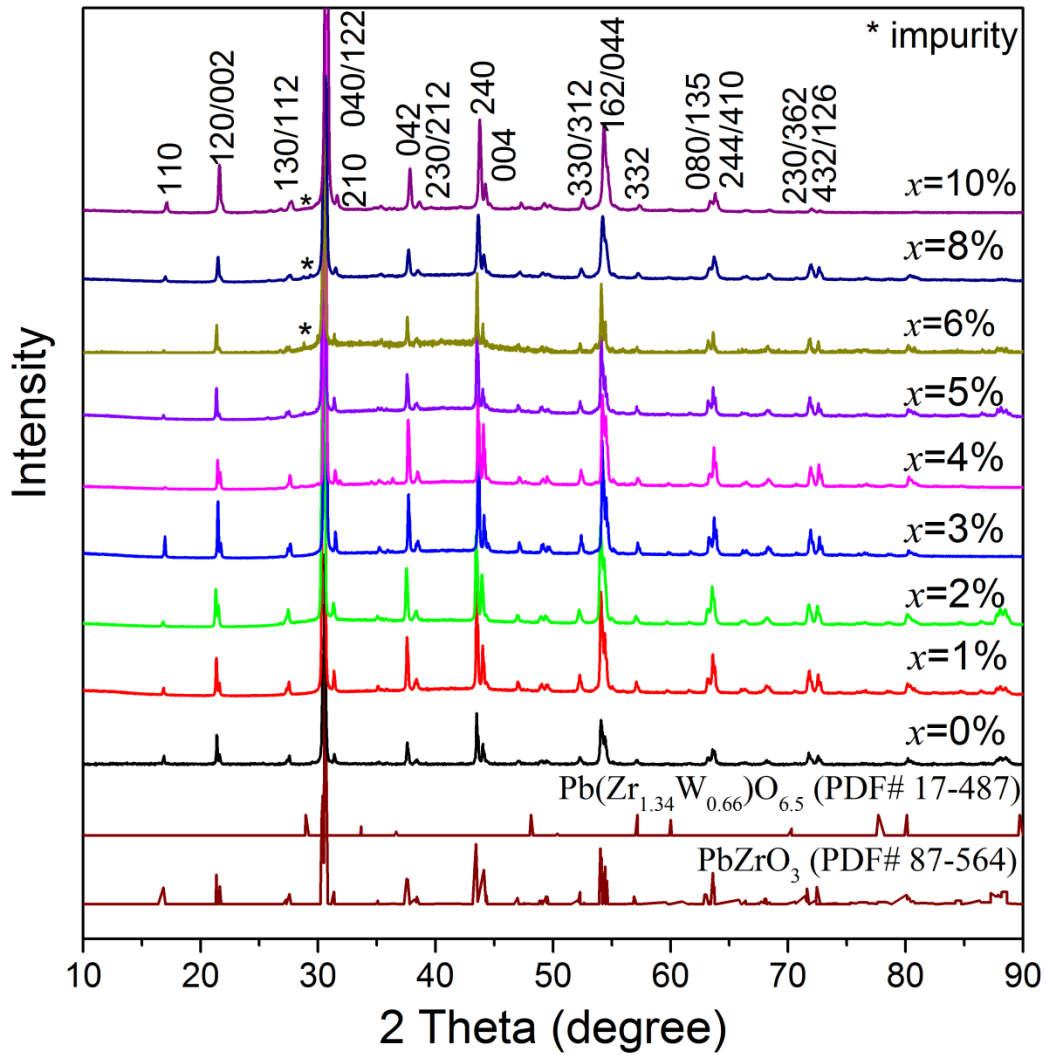
Figure 4.1. XRD patterns of $PbZrO_3$ and $(1-x)PbZrO_3–xPb(Zn_{1/2}W_{1/2})O_3$ (x = 0% - 10%). Peaks are indexed in the orthorhombic setting.
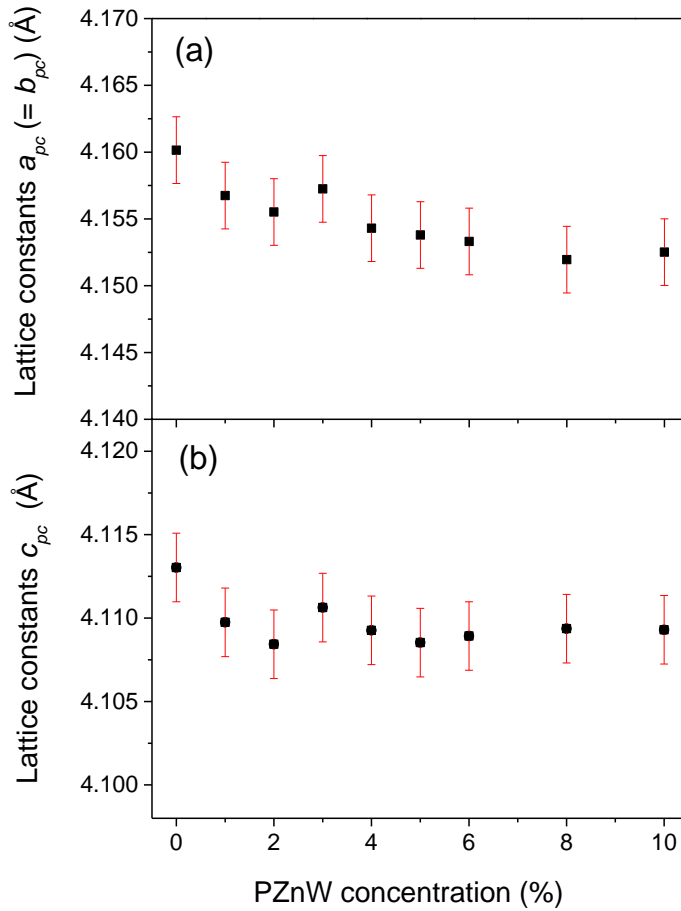
Figure 4.2.   Plots of lattice constants of (a) a_{pc} (= b_{pc}) and (b) c_{pc} as a function of composition for the (1-x)PbZrO$_3$–xPb(Zn$_{1/2}$W$_{1/2}$)O$_3$ solid solution.

Figure 4.3 displays the SEM micrographs of the surface of the as-sintered (1-x)PZ-xPZnW ceramics with x between 0% and 8%. No plate-like grains were observed for all the compositions. For the pure PbZrO$_3$ ceramic, pores are found to exist and its grain size is smaller (1 μm) compared to other compositions. With the substitution of PZnW, the number of pores drops significantly and the grains on the sample surface obviously become bigger. The ceramic with 3%PZnW exhibits the densest surface. The grain sizes of 3%PZnW (5.1 μm) and 4%PZnW (4.5 μm) are relatively larger than that of the rest of compositions whose grain size varies between 1.0 and 2.4 μm.

x=0%

x=0.5%

x=1%

x=2%

x=3%

x=4%

x=5%

x=6%

x=8%
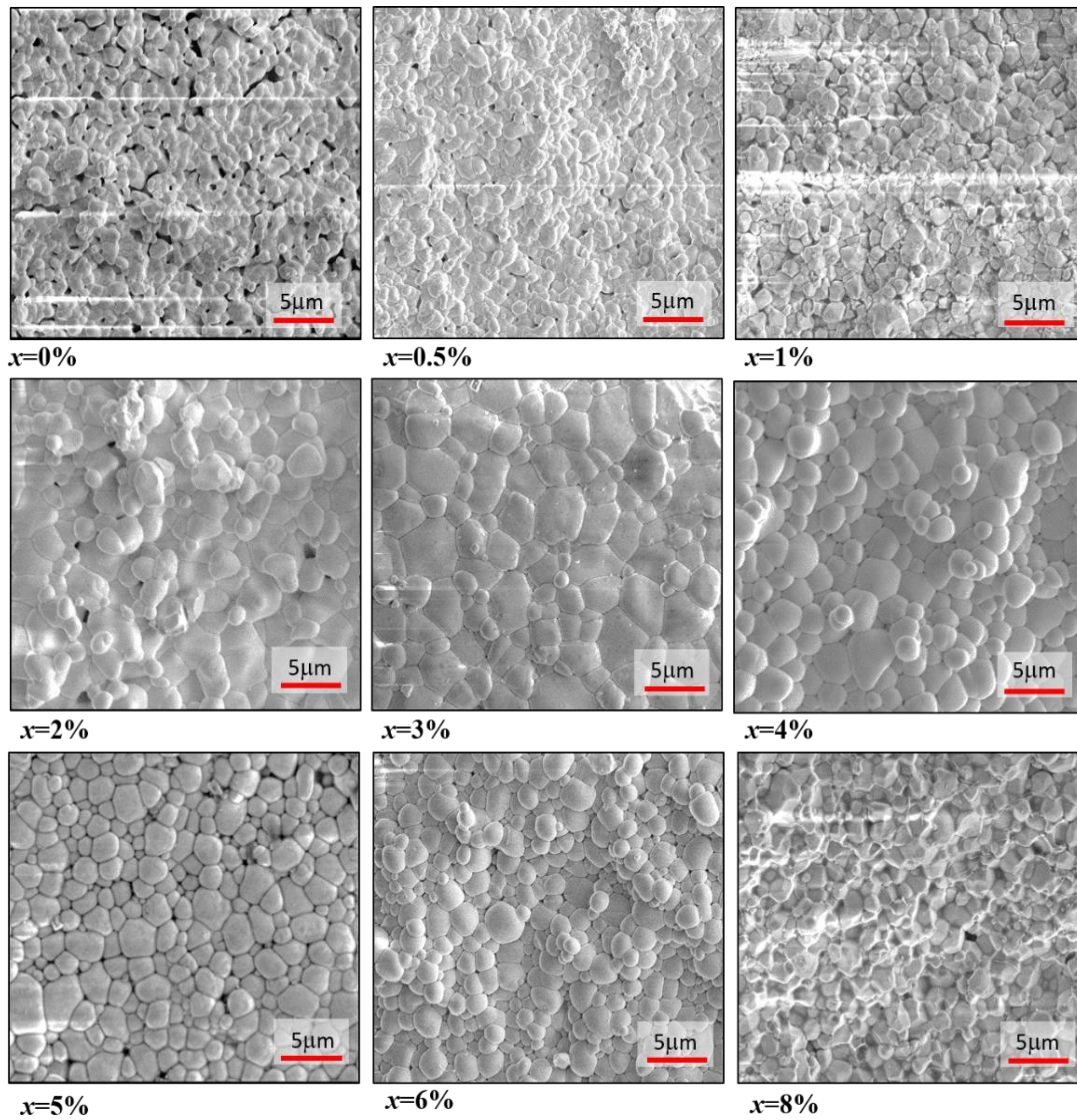
Figure 4.3.   Scanning electron microscopy (SEM) images of as-sintered
(1-x)PZ–xPZnW ceramics (x = 0% - 8%).

Table 4.1. Rietveld-refined structural parameters for various compositions of the (1-x)PZ-xPZnW solid solutions under *Pbam* model

	x	y	z
0%			
Pb1	0.7094(11)	0.12384(26)	0
Pb2	0.7115(11)	0.12968(26)	0.5
Zr1	0.24227(31)	0.12281(67)	0.2475(16)
O1	0.2998(75)	0.1477(45)	0
O2	0.2884(75)	0.0965(39)	0.5
O3	0.0229(16)	0.25264(98)	0.2373(55)
O4	0	0.5	0.3090(27)
O5	0	0	0.2540(90)
Dimensions (Å)	5.87884	11.77567	8.22606
R_{wp}	5.952		
1%			
Pb1	0.7113(14)	0.12370(30)	0
Pb2	0.7089(15)	0.12963(30)	0.5
Zr1	0.24104(33)	0.12223(61)	0.2497(44)
Zn1	0.24104(33)	0.12223(61)	0.2497(44)
W1	0.24104(33)	0.12223(61)	0.2497(44)
O1	0.2793(63)	0.1516(42)	0
O2	0.2822(63)	0.1003(44)	0.5
O3	0.0242(17)	0.2472(10)	0.2653(58)
O4	0	0.5	0.2002(34)
O5	0	0	0.249(11)
Dimensions (Å)	5.87364	11.76681	8.21949
R_{wp}	7.04		
2%			
Pb1	0.7113(14)	0.12370(30)	0
Pb2	0.7089(15)	0.12963(30)	0.5
Zr1	0.24104(33)	0.12223(61)	0.2497(44)
Zn1	0.24104(33)	0.12223(61)	0.2497(44)
W1 W	0.24104(33)	0.12223(61)	0.2497(44)
O1	0.2793(63)	0.1516(42)	0
O2	0.2822(63)	0.1003(44)	0.5
O3	0.0242(17)	0.2472(10)	0.2653(58)
O4	0	0.5	0.2002(34)
O5	0	0	0.249(11)

	x	y	z
Dimensions (Å)	5.87238	11.76239	8.21686
R_{wp}	8.913		
3%			
Pb1	0.7099(10)	0.12415(27)	0
Pb2	0.7072(11)	0.12962(27)	0.5
Zr1	0.24236(29)	0.12412(68)	0.24545(82)
Zn1	0.24236(29)	0.12412(68)	0.24545(82)
W1	0.24236(29)	0.12412(68)	0.24545(82)
O1	0.2772(58)	0.1608(22)	0
O2	0.3120(59)	0.1187(35)	0.5
O3	0.0175(18)	0.2566(10)	0.2745(39)
O4	0	0.5	0.1972(32)
O5	0	0	0.2602(70)
Dimensions (Å)	5.86983	11.7524	8.22126
R_{wp}	5.961		
4%			
Pb1	0.71164(79)	0.12367(44)	0
Pb2	0.70886(78)	0.12892(47)	0.5
Zr1	0.24272(41)	0.12250(65)	0.2516(12)
Zn1	0.24272(41)	0.12250(65)	0.2516(12)
W1	0.24272(41)	0.12250(65)	0.2516(12)
O1	0.2463(65)	0.1489(31)	0
O2	0.3205(58)	0.1401(40)	0.5
O3	0.0275(24)	0.2563(14)	0.2621(28)
O4	0	0.5	0.1636(41)
O5	0	0	0.2795(73)
Dimensions (Å)	5.87057	11.75917	8.21853
R_{wp}	8.522		
5%			
Pb1	0.7145(13)	0.12386(43)	0
Pb2	0.7063(13)	0.12840(39)	0.5
Zr1	0.24238(38)	0.12256(64)	0.2491(20)
Zn1	0.24238(38)	0.12256(64)	0.2491(20)
W1	0.24238(38)	0.12256(64)	0.2491(20)
O1	0.2469(62)	0.1536(39)	0
O2	0.3070(74)	0.1301(42)	0.5
O3	0.0293(21)	0.2498(13)	0.2554(87)

	x	y	z
O4	0	0.5	0.1959(33)
O5	0	0	0.2517(93)
Dimensions (Å)	5.87013	11.75717	8.21706
R_{wp}	8.505		
6%			
Pb1	0.7090(10)	0.12417(35)	0
Pb2	0.7129(11)	0.12857(37)	0.5
Zr1	0.24252(38)	0.12366(94)	0.24300(67
Zn1	0.24252(38)	0.12366(94)	0.24300(67
W1	0.24252(38)	0.12366(94)	0.24300(67
O1	0.3154(70)	0.1411(47)	0
O2	0.2814(69)	0.0904(34)	0.5
O3	0.0245(23)	0.2591(14)	0.2208(48)
O4	0	0.5	0.3123(39)
O5	0	0	0.2199(54)
Dimensions (Å)	5.8696	11.75549	8.21785
R_{wp}	8.646		
8%			
Pb1	0.7090(10)	0.12417(35)	0
Pb2	0.7129(11)	0.12857(37)	0.5
Zr1	0.24252(38)	0.12366(94)	0.24300(67)
Zn1	0.24252(38)	0.12366(94)	0.24300(67)
W1	0.24252(38)	0.12366(94)	0.24300(67)
O1	0.3154(70)	0.1411(47)	0
O2	0.2814(69)	0.0904(34)	0.5
O3	0.0245(23)	0.2591(14)	0.2208(48)
O4	0	0.5	0.3123(39)
O5	0	0	0.2199(54)
Dimensions (Å)	5.86747	11.75205	8.21873
R_{wp}	6.796		
10%			
Pb1	0.7050(13)	0.10953(49)	0
Pb2	0.7255(14)	0.12184(51)	0.5
Zr1	0.22436(88)	0.12630(47)	0.2505(13)
Zn1	0.22436(88)	0.12630(47)	0.2505(13)
W1	0.22436(88)	0.12630(47)	0.2505(13)
O1	0.3463(85)	0.1439(36)	0

	x	y	z
O2	0.2565(56)	0.0891(43)	0.5
O3	0.0039(36)	0.2755(19)	0.2331(54)
O4	0	0.5	0.2939(50)
O5	0	0	0.3048(43)
Dimensions (Å)	5.86849	11.75318	8.2186
R_{wp}	8.37		

4.4.2.   Electrical Properties

Temperature dependence of the dielectric permittivity and dielectric loss of the (1−x)PZ-xPZnW ceramics were measured at several frequencies on cooling from 300 $^{\circ}$C to 25 $^{\circ}$C (Figure 4.4). The un-modified PZ ceramic (x = 0%) transforms from the paraelectric cubic phase to the intermediate phase at T_C (228 $^{\circ}$C) on cooling. The permittivity decreases dramatically at 213 $^{\circ}$C (marked with a black arrow), which could indicate the transformation from the intermediate phase into the AFE phase. The B-site substitution using the Zn^{2+} and W^{6+} ions noticeably reduces the transition temperature T_{AFE-FE} from 213 $^{\circ}$C to 58 $^{\circ}$C with x increasing from 0% to 8%. Meanwhile, T_C drops slowly from 228 $^{\circ}$C to 195 $^{\circ}$C and remains at around 195 $^{\circ}$C once x reaches 5%. It is worth mentioning that the dielectric behaviour of 8%PZnW and 10%PZnW ceramics, including the magnitude of permittivity, T_{AFE-FE} and T_C, is almost the same. This confirms verifies that the solubility limit of (1-x)PZ-xPZnW solid solution is about 8%PZnW. As demonstrated in all dielectric spectra, the transition from the paraelectric phase to the intermediate phase at T_C is gradual while the transition from the intermediate phase to the AFE phase at T_{AFE-FE} is more sudden, suggesting the orders of these two transitions are different.

To further confirm this assumption, the dielectric constant of 5%PZnW (95%PZ-5%PZnW) was measured on both heating and cooling and the result is shown in Figure 4.5. It is noteworthy that thermal hysteresis appears at T_{AFE-FE} but there is no sign of it at T_C. The continuity in the first derivative of the free energy defines the order of phase transitions.[101] In first order phase transitions, the entropy and the spontaneous polarization, which are the first derivatives of the free energy with respect to temperature

and electric field, respectively, are discontinuous. In second order phase transitions, however, both the entropy and the spontaneous polarization show continuous feature.[101, 102] According to the thermodynamic analysis, thermal hysteresis is the most remarkable characteristic for first-order phase transitions.[102] Therefore, it is conjectured that the transition at T_C in this system is of second-order whereas the transition at T_{AFE-FE} is of first-order. Moreover, the value of thermal hysteresis at T_{AFE-FE} is enlarged with increasing PZnW concentration, from 18 ^{o}C for x = 3% to 46 ^{o}C for x = 8% (whose dielectric measurements not shown). The existence of thermal hysteresis for the first-order phase transitions can be explained by a triple-well potential diagram.[103] At the critical temperature, the triple wells have the same depth which means the same minimum free energies for the AFE and FE orderings in our case. But the transition does not occur at this point. On further heating, the minimum energy of AFE coupling rises. When it is higher enough than the minimum energy of FE coupling, the phase transition takes place. Thus, the transition temperature on heating is higher than the critical temperature. Similarly, this phenomenon happens on cooling and the thermal hysteresis is then generated.[103] As the concentration of PZnW increases, T_{AFE-FE} shifts to lower temperature. On the other hand, the changing rate of the minimum potential energies of AFE or FE ordering should slow down at lower temperature. Therefore, the thermal hysteresis enlarges at higher concentration of PZnW, even though the energy barrier between the AFE and FE states is smaller.

Electrical field versus polarization hysteresis loops (P-E loops) of (1-x)PZ-xPZnW (x = 0% - 8%) were measured under a maximum field of 70 kV/cm at room temperature. All compositions display linear P-E loops due to their high critical fields E_F which are greater than the maximum (breakdown) field. In order to display the temperature dependence of (anti-)ferroelectric properties of the (1-x)PZ-xPZnW ceramics, the P-E loops of the 97%PZ-3%PZnW ceramic measured on cooling from 225 ^{o}C to 25 ^{o}C are shown in Figure 4.6a – 4.6d. At 225 ^{o}C, a temperature above T_C (212 ^{o}C), a narrow and unsaturated P-E loop shows up, indicating the presence of the paraelectric phase. When the temperature decreases to 210 ^{o}C, a typical ferroelectric hysteresis loop appears. It reveals a transition from the paraelectric to ferroelectric state, and further confirms the ferroelectric nature of the intermediate phase. Upon further cooling through T_{AFE-FE} to 150 ^{o}C, a double hysteresis loop revealing antiferroelectricity emerges. In addition, it is obvious that E_F becomes larger on cooling, around 58 kV/cm at 150 ^{o}C compared to 65

kV/cm at 140 ºC (Figure 4.6c). When temperature decreases to 25 ºC, a linear loop appears again due to the large critical field E_F.
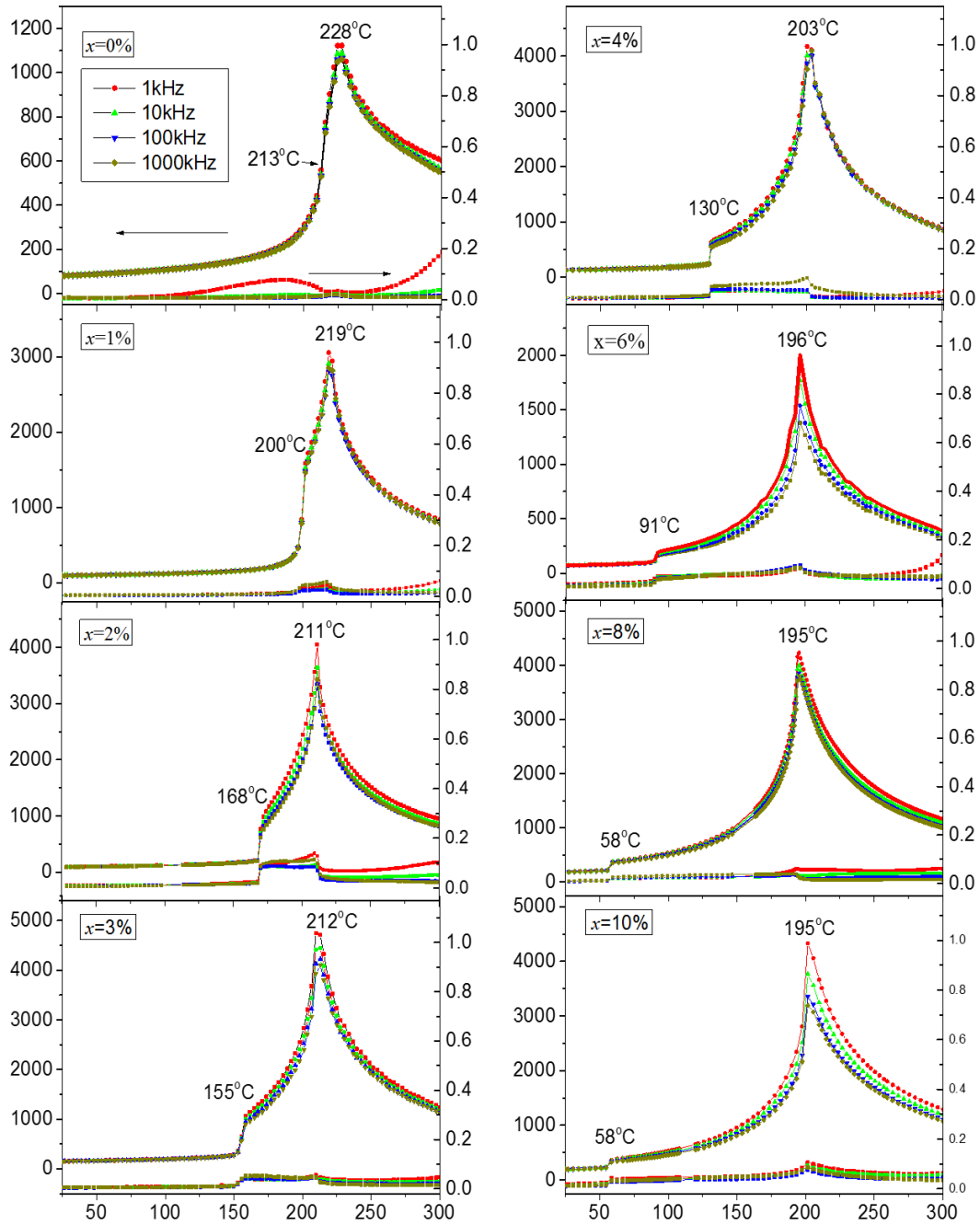
Figure 4.4.   Real part of dielectric permittivity (ε') and dielectric loss (tanδ) as a function of temperature for the (1−x)PZ-xPZnW ceramics, x = 0% - 10%.
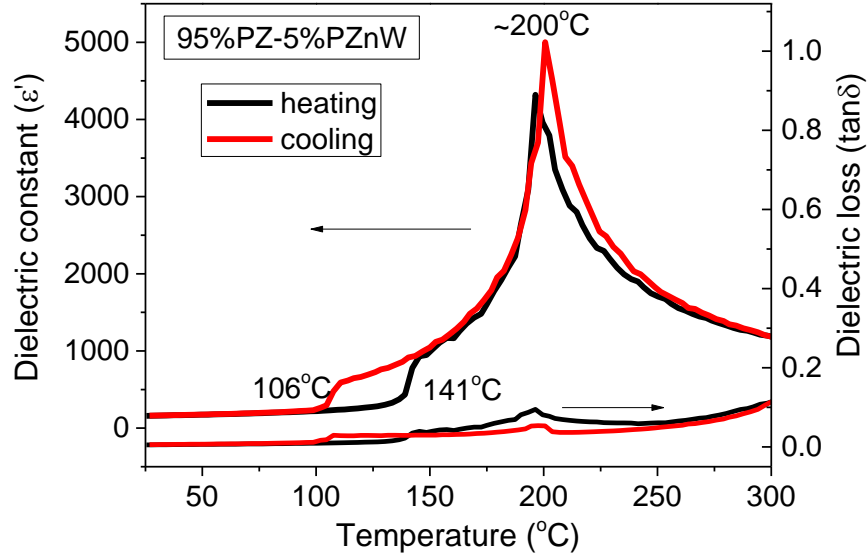
Figure 4.5. Temperature dependences of the dielectric constant (ε') and dielectric loss (tan δ) of 95%PZ-5%PZnW at 10^3 Hz on heating and cooling.
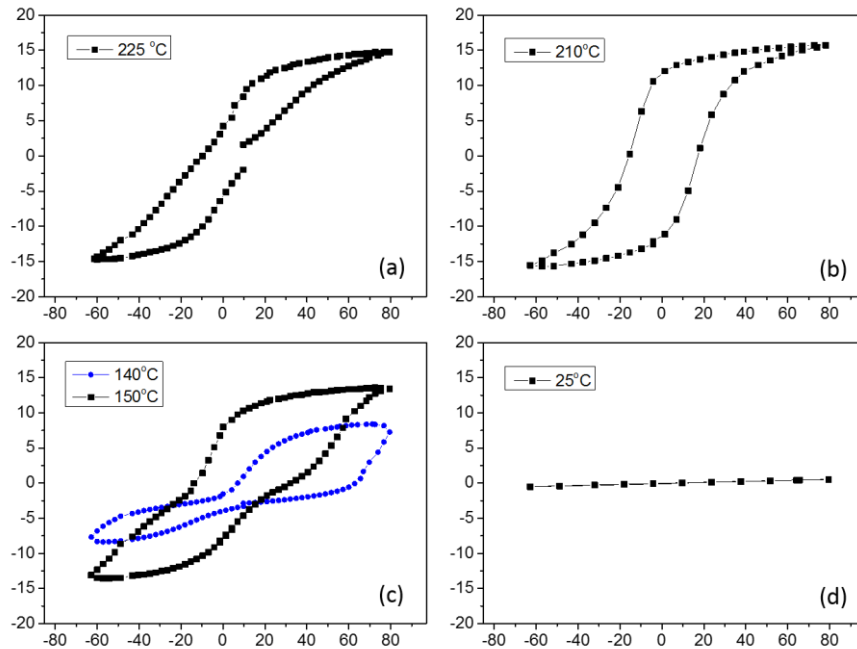
Figure 4.6. Polarization versus electric field, P(E), loops of the 97%PZ-3%PZnW ceramic measured on cooling at: (a) 225 °C, (b) 210 °C, (c) 140 and 150 °C, and (d) 25 °C.

4.4.3. Phase Diagram of the (1-x)PbZrO₃-xPb(Zn₁/₂W₁/₂)O₃ Solid Solution

The variations of the transition temperatures T_{AFE-FE} on heating and cooling, and of T_C as a function of the PZnW concentration, are illustrated in Figure 4.7. It is obvious that T_{AFE-FE} decreases more significantly than T_C as the PZnW concentration increases. The decreasing rate of T_{AFE-FE} is approximately 12 °C and 20 °C per percent of PZnW on heating and cooling, respectively. The decreasing rate of T_C is around 4 °C per percent of PZnW. The different decreasing rate for T_{AFE-FE} and T_C enlarges the temperature range of the intermediate ferroelectric phase. The resultant expansion of the intermediate FE phase can be explained by the presence of the incommensurate structural modulations. The dopants, Zn^{2+} and W^{6+} ions, on B-site can be quenched and thus produce an incommensurately modulated state in the PZ-based system. Such incommensurate phase reduces the energy barrier between the AFE and FE ordering[80] and therefore lowers the transition temperature T_{AFE-FE}. While the concentration of PZnW increases, the energy barrier between the AFE and FE coupling decreases. As a result, the intermediate FE state is stabilized to a lower temperature.
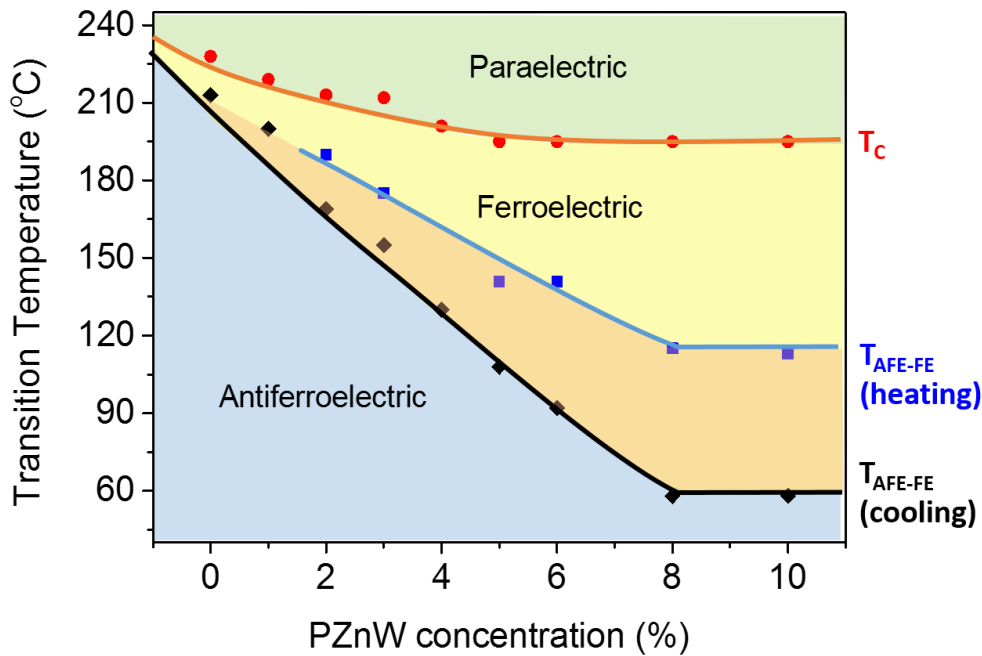
Figure 4.7.   Variations of the transition temperatures of T_{AFE-FE} measured on heating (blue) and on cooling (black), and of T_C (red), as a function of the concentration of PZnW for the PZ – PZnW solid solution.

4.5. Conclusions

In summary, a new solid solution of $(1-x)PbZrO_3$-$xPb(Zn_{1/2}W_{1/2})O_3$ ($x = 0\%$ - 10%) has been successfully synthesized by the solid state reaction method. The solubility limit is found to be around 8%PZnW. All the compositions within the solubility limit crystallize in an orthorhombic structure with the space group of *Pbam*. In addition, the grain size increases significantly with the addition of PZnW while the number of pores decreases. The substitution of PZnW reduces T_{AFE-FE} more noticeably than T_C, enlarging the temperature window for the intermediate FE phase. A typical ferroelectric hysteresis loop was displayed at temperatures between T_{AFE-FE} and T_C, confirming the ferroelectric nature of the intermediate phase. Double hysteresis loops referring to the AFE properties are observed below T_{AFE-FE} and unsaturated P-E loop revealing the PE behaviour appears above T_C. The $(1-x)PZ$-$xPZnW$ solid solution ceramics experience a transition sequence from the antiferroelectric to the intermediate ferroelectric and then to the paraelectric phases upon heating and this transition sequence is reversible. Also, the substitution of PZnW narrows the energy difference between the AFE and FE ordering and thus expands the temperature range for the intermediate ferroelectric phase, making it possible to investigate the structure and properties of this intermediate phase. This study will be reported in **Chapter 5**.

Chapter 5.

Study of the Intermediate Ferroelectric Phase in the Solid Solution of (1-x)PbZrO$_3$-xPb(Zn$_{1/2}$W$_{1/2}$)O$_3$

5.1. Abstract

The antiferroelectric 0.97PbZrO$_3$-0.03Pb(Zn$_{1/2}$W$_{1/2}$)O$_3$ (97%PZ-3%PZnW) ceramic was prepared by the solid state reaction method. The temperature dependence of dielectric permittivity was studied. The Curie temperatures (T$_C$) on cooling and heating are both 212 ^{o}C, indicating a second order phase transition. Another phase transition below T$_C$ was observed, from the antiferroelectric (AFE) phase at room temperature to an intermediate phase at higher temperature. This transition occurs at 155 ^{o}C and 175 ^{o}C on cooling and heating, respectively, showing thermal hysteresis. It represents a first order phase transition. Within the temperature range of the intermediate phase, ferroelectric hysteresis loops were displayed and second harmonic generation signals were detected, indicating the non-centrosymmetric and polar nature for the intermediate phase. High resolution X-ray diffraction and the subsequent refinement results show that the intermediate FE phase is of rhombohedral structure with $R3m$ and the AFE phase is of orthorhombic structure with space group *Pbam*. A phase diagram of the (1-*x*) PbZrO$_3$-*x* Pb(Zn$_{1/2}$W$_{1/2}$)O$_3$ solid solution has been established as a result of this work.

5.2. Introduction

Chemical modified PbZrO$_3$ (PZ) materials and PbZrO$_3$-based antiferroelectric (AFE) solid solutions are attracting much extensive attention in recent years because of their potential applications in high performance energy storage devices and microelectromechanical systems.[70, 77, 99] Comparing to ferroelectrics (FE) and linear paraelectrics (PE), AFE materials enhance the energy density significantly, resulting from

their reversible field-induced AFE to FE transformation.[71] High breakdown field and low critical field (E_F) for field-induced AFE-FE transition are therefore prerequisites for practical applications. In PZ systems, lead cations displace along the $(110)_{pc}$ direction, giving rise to quadrupling of the unit cell and antiferroelectric property.[39, 40] At room temperature, PZ is of the orthorhombic structure that belongs to the *Pbam* space group with dimensions of $\sqrt{2}a_{pc} \times 2\sqrt{2}a_{pc} \times 2c_{pc}$, where a_{pc} and c_{pc} are lattice parameters of the pseudocubic perovskite subcell.[5, 6] Most of AFEs experience a usual phase transition from PE phase to AFE phase while cooling down through Curie temperature (T_C).[100] But in PZ systems, there is a possible intermediate FE phase in between the room-temperature AFE and the high-temperature PE phase. This intermediate phase was first discovered by B. A. Scott[41] in a PZ single crystal, and its temperature window is narrow (225 - 230 ^{o}C).[77] Whatmore et al. later confirmed the existence of the intermediate phase using X-ray Diffractometer (XRD) and dielectric measurement.[42] They reported that the intermediate phase is of rhombohedral symmetry[42] but the space group which it belongs to is still uncertain. It is also found that pressure affects the stability of the intermediate phase.[101]

In general, critical fields of unmodified PZ systems are far higher than their breakdown fields, which narrows their application range. Currently, chemical modification has been utilized to improve their properties. Most commonly, La^{3+}, Ti^{4+} and Sr^{2+} ions are used to modify PZ simultaneously, forming the lead lanthanum stannate zirconate titanate (PLZST) solid solution. This modification successfully enlarges the longitudinal strain of the system.[44, 45] Besides, substitution using Hf^{2+} ion decreases the AFE-FE transition temperature (T_{AFE-FE}) and T_C, which slightly expands the existence of the FE phase.[103] Inducing Ba^{2+} also lowers T_C, along with E_F, of PZ ceramics.[103] Some PZ-based solid solutions, for example $PbZrO_3$-$Pb(Mg_{1/2}W_{1/2})O_3$[46], $PbZrO_3$-$Pb(In_{1/2}Nb_{1/2})O_3$[47] and $PbZrO_3$-$Pb(Co_{1/3}Nb_{2/3})O_3$[48], have successfully improved the stability of the intermediate FE phase, bringing down the transition temperature of T_{AFE-FE}. In the form of thin films, Sr-doping improves energy storage density and energy efficiency[104], while Ce-doping on the $[111]_{pc}$-oriented PZ thin films decreases dielectric permittivity and increases E_F.[105] Nonetheless, many of those reports are focused on properties study and few of them have a deep insight into the intermediate FE phase even though this phase is also of great interest to investigate. $Pb(Zn_{1/2}W_{1/2})O_3$ (PZnW) perovskite has not been synthesized through conventional solid state reaction method but through high pressure

synthesis.[106] Since its difficulties of synthesis, reports on its properties are deficient. On the other hand, PZnW is predicted to be antiferroelectric and identical to $Pb(Mg_{1/2}W_{1/2})O_3$ whose Pb^{2+} displacements are along $[100]_{pc}$ or $[010]_{pc}$ orientations.[91,107] The different AFE orderings in between PZ and PZnW is possible to generate incommensurate states in their solid solutions and thus expands the existence of the intermediate FE phase in PZ systems. Since $PbZrO_3$-based solid solutions primarily use FE end-members by far, solid solutions using AFE end-members are also an interesting field to explore. According to our previous report (**Chapter 3**)[108], it has been discovered that the formation of solid solution with $Pb(Zn_{1/2}W_{1/2})O_3$ significantly enlarged the temperature range of the intermediate phase in PZ ceramics. In this work, the ceramics of $0.97PbZrO_3$-$0.03Pb(Zn_{1/2}W_{1/2})O_3$ (97%PZ-3%PZnW) is utilized to investigate the phase evolution by a series of measurements.

5.3. Experimental

The ceramics of composition $(1-x)PbZrO_3$-$xPb(Zn_{1/2}W_{1/2})O_3$ (x = 3%) were prepared by a two-step solid state reaction method. The precursor phase, $ZnWO_4$, was first synthesized from the mixture of ZnO and WO_3 powders (purity >99%) at 1000°C for 12 hours. It was then mixed with stoichiometric amount of ZrO_2 and PbO. An excess 1 mol% PbO was added to compensate the lead oxide evaporation during high temperature synthesis process. The mixed oxides were milled with zirconium oxide balls in ethyl alcohol for 24 hours, and then dried and calcined at 880 °C for 4 hours. The as-calcined powder was ball milled in ethyl alcohol overnight. In order to obtain dense ceramics, 1 wt% polyvinyl alcohol (PVA) binder was used. After being dried, the calcined powder was pressed into pellets and sintered at 1000 °C for 2 hours. The temperature dependence of dielectric permittivity was measured by using a Novocontrol broadband dielectric analyzer. The polarization versus electric field (P-E) loops were measured by RT-66 ferroelectric test system (Radian Technology). Second Harmonic Generation (SHG) measurements were carried out with an Nd-YAG laser producing a 1 Hz pulsed infrared beam (λ = 1064 nm). High-resolution X-ray powder diffraction (XRD) was performed on a PANalytical X'Pert Pro MPD with curved Johansson monochromator producing Cu *Kα1* radiation and with the Anton Paar HTK1200N furnace for high

temperature measurement. The last two experiments were performed at the University of Warwick, UK, in collaboration with Prof. P. A. Thomas and her group.

5.4. Results and Discussion

5.4.1. Electrical Properties

Shown in Figure 5.1 are the temperature dependences of the dielectric permittivity of a $0.97PbZrO_3$-$0.03Pb(Zn_{1/2}W_{1/2})O_3$ (97%PZ-3%PZnW) ceramic that were measured at 1 kHz on heating and cooling between 25 ^{o}C and 300 ^{o}C. Two dielectric anomalies are observed, which implies the existence of an intermediate phase between the room-temperature antiferroelectric phase and the high-temperature (above T_C) paraelectric phase. The values of T_C on cooling and heating are found to be both 211 ^{o}C. Namely, no thermal hysteresis is found at T_C, which means that this transition is a second-order phase transition. The other dielectric anomaly at a lower transition temperature (T_{AFE-FE}) results from the transition between the antiferroelectric phase and the intermediate phase. This intermediate phase has been observed in un-modified PZ systems, but within a very narrow temperature range only.[42] In the 97%PZ-3%PZnW ceramic, this transition takes place at 173 ^{o}C on heating and 155 ^{o}C on cooling. Meanwhile, the permittivity changes abruptly at T_{AFE-FE}. The thermal hysteresis of 18 ^{o}C and the sudden changes in permittivity indicate a first-order phase transition between the AFE and intermediate phases.
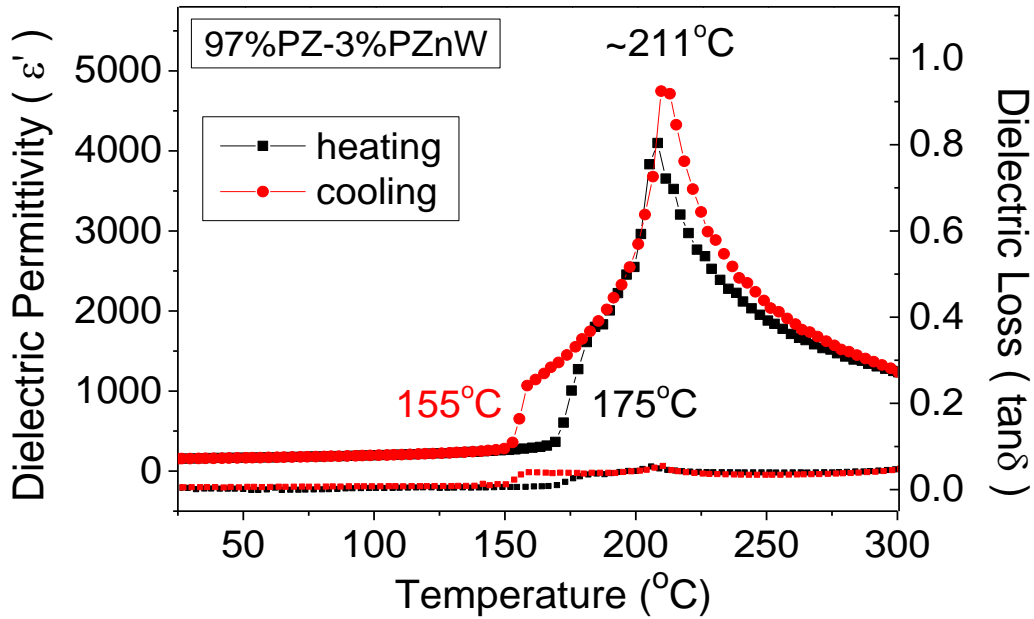
Figure 5.1.   Variation of the dielectric constant (ε') as a function of temperature for the 97%PZ–3%PZnW ceramic measured at 10^3 Hz upon heating and cooling.

To further investigate the nature of this intermediate phase, ferroelectric measurements were performed at several temperatures on heating. The resulting P-E loops are shown in Figure 5.2. At room temperature, only a linear curve is obtained because of the high E_F. With increasing temperature, the energy barrier between the AFE ordering and the metastable field-induced FE ordering is reduced, and E_F decreases as a result. A double hysteresis loop is therefore displayed at 120 °C. When the temperature approaches 170 °C (around $T_{AFE\text{-}FE}$), a typical ferroelectric hysteresis loop with remanent polarization of 14.0 μC/cm^2 is obtained. It reveals the occurrence of the phase transition at $T_{AFE\text{-}FE}$ and the ferroelectric nature for the intermediate phase. A slim and non-linear P-E loop is displayed at 240 °C, confirming the paraelectric phase above T_C.
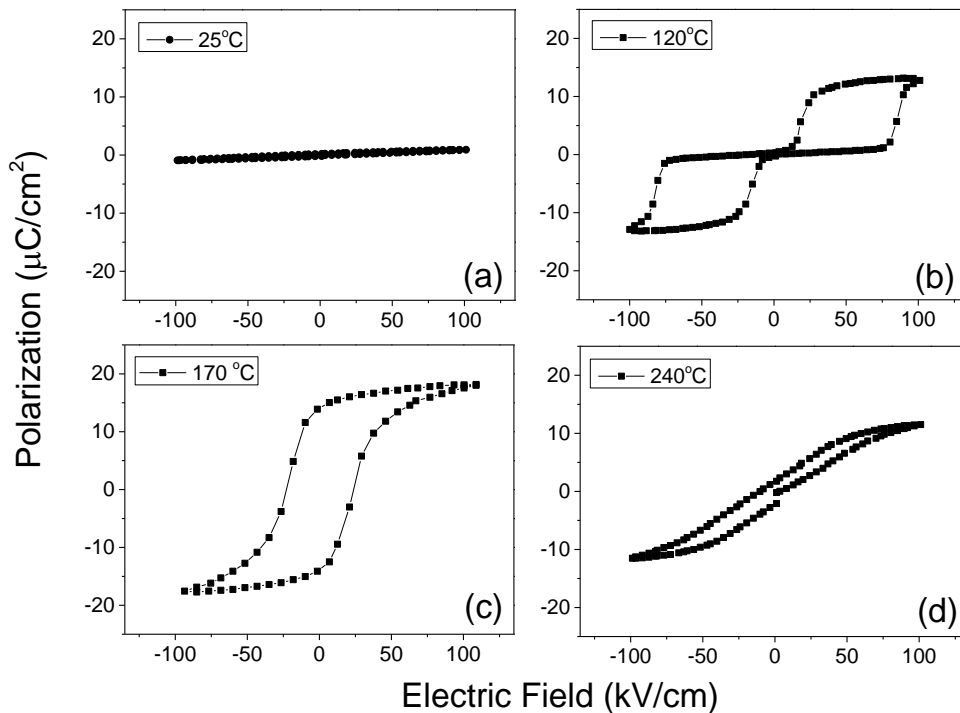
Figure 5.2.   Polarization versus electric field loops displayed on 97%PZ–3%PZnW upon heating at: (a) 25 °C, (b) 120 °C, (c) 170 °C and (d) 240 °C.

5.4.2.   Structural Analysis of the Intermediate Ferroelectric Phase

The SHG measurement of 97%PZ-3%PZnW was carried out between 25 °C and 300 °C on heating and subsequent cooling. The results are shown in Figure 5.3. This technique is capable of revealing the existence of non-centrosymmetric structures. For a crystal symmetry possessing a center of inversion, the SHG intensity signal is zero. Otherwise it is non-zero.[109] Thus, based on the changes in SHG signal, one can determine whether a compounds experiences a transformation from a centrosymmetric structure to a non-centrosymmetric one, and vice versa. From Figure 5.3, it is clear that the SHG signals are non-zero only in between 175 and 214 °C on heating, and 146 and 214 °C on cooling. In other words, the 97%PZ-3%PZnW ceramic is non-centrosymmetric within those temperature windows while it is centrosymmetric outside those windows. In the SHG measurement, thermal hysteresis appears only at T_{AFE-FE}, which is consistent with the results from the dielectric measurements.
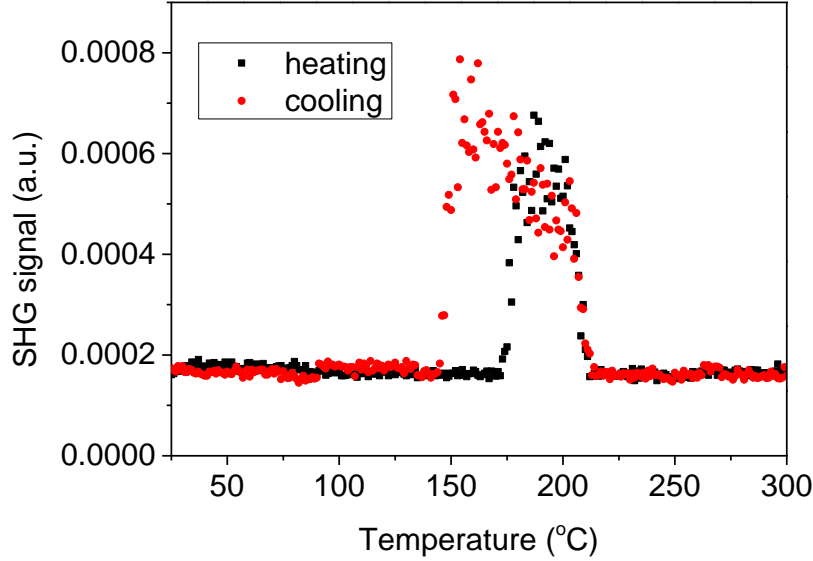
Figure 5.3.   Variation of the normalized SHG intensity (in a.u.) as a function of temperature for 97%PZ-3%PZnW.

High-temperature XRD data were utilized to determine the structure of the intermediate ferroelectric state. Shown in Figure 5.4a and 5.4b are the XRD patterns of the 97%PZ-3%PZnW ceramic measured on heating. For a better visualization of superlattice, the indices of both the orthorhombic *Pbam* ($\sqrt{2}a_{pc} \times 2\sqrt{2}a_{pc} \times 2c_{pc}$) setting and the pseudocubic ($a_{pc} \times a_{pc} \times c_{pc}$) setting are labeled in Figure 5.4b, using subscripts *o* and *pc*, respectively. The antiparallel displacements of Pb^{2+} in the $PbZrO_3$ and $PbZrO_3$-based solid solutions are associated with the 1/4 (*h k l*) reflections.[39] The intensities of the $(7/4\ \text{-}1/4\ 0)_{pc}$ and $(5/4\ \text{-}3/4\ 1)_{pc}$ peaks decrease with increasing temperature up to 175 °C, above which those two peaks disappear. This suggests that the driving force of the antiparallel Pb^{2+} ordering is reduced by thermal energy. The $(1\ 1\ 1)_{pc}$ peak meanwhile develops a shoulder peak on the lower angle side at 175 °C, which reveals the appearance of a rhombohedral phase. The overall XRD pattern at 175 °C represents a mixture of the rhombohedral and orthorhombic structures. A pure rhombohedral structure appears at 200 °C, as seen from the observation that the $(7/4\ \text{-}1/4\ 0)_{pc}$, $(5/4\ \text{-}3/4\ 1)_{pc}$ and $(0\ 0\ 2)_{pc}$ peaks disappear while the $(1\ 1\ \text{-}1)$ reflection remains. It is noteworthy that no peaks corresponding to oxygen tilting are observed. Therefore, this intermediate ferroelectric phase should belong to *R*3*m* space group rather than *R*3*c*.

71

On heating up to 225 °C, the (1 1 1) reflection gradually becomes singlet, indicating a transition into the cubic phase.

In order to study the evolution of structural parameters, the Rietveld refinements were carried out using TOPAS Academic software. The results are shown in Table 5.1. A single *Pbam* model was used for the fitting of the XRD data collected between 25 °C and 150 °C. The calculated results are in accordance with the experimental data, which means that in the antiferroelectric state, the crystal structure of 97%PZ-3%PZnW is *Pbam*. For the structure at 175 °C, the *Pbam* model was first examined but its agreement R-factor (R_{wp}) is abnormally high, jumping to 22.79%. The calculated intensities of some reflections also fail to match the experimental results, such as the (1 1 0)$_{pc}$ reflection (see Figure 5.5a). In order to fully analyze the nature of this phase(s), both the *Pbam* and *R3m* models are simultaneously applied in the subsequent refinements. Here, the hexagonal unit cell setting[92] is used in the fitting of the *R3m* model. A great improvement in the fitting results is obtained, which suggests the mixture of phases consisting of the orthorhombic and rhombohedral symmetries. The corresponding fitting result is shown in Figure 5.5b. The phase fractions of the orthorhombic (*Pbam*) and rhombohedral (*R3m*) structures are found to be 60% and 40%, respectively. The crystal is a pure rhombohedral phase without oxygen octahedron tilts at 200 °C. The experimental data are fitted almost perfectly based on a single *R3m* model. This confirms that the intermediate ferroelectric phase belongs to the space group of *R3m*. It is reasonable to speculate that the intermediate phase existing in the 97%PZ-3%PZnW ceramic is the same as the intermediate phase existing in the PZ and PZ-based solid solutions. Therefore, we can deduce that the intermediate phase found in PZ[42] and other PZ-based systems is the rhombohedral phase with space group of *R3m*. At 225 °C and above, the fitting of powder data matches the calculated results using $Pm\bar{3}m$ model.
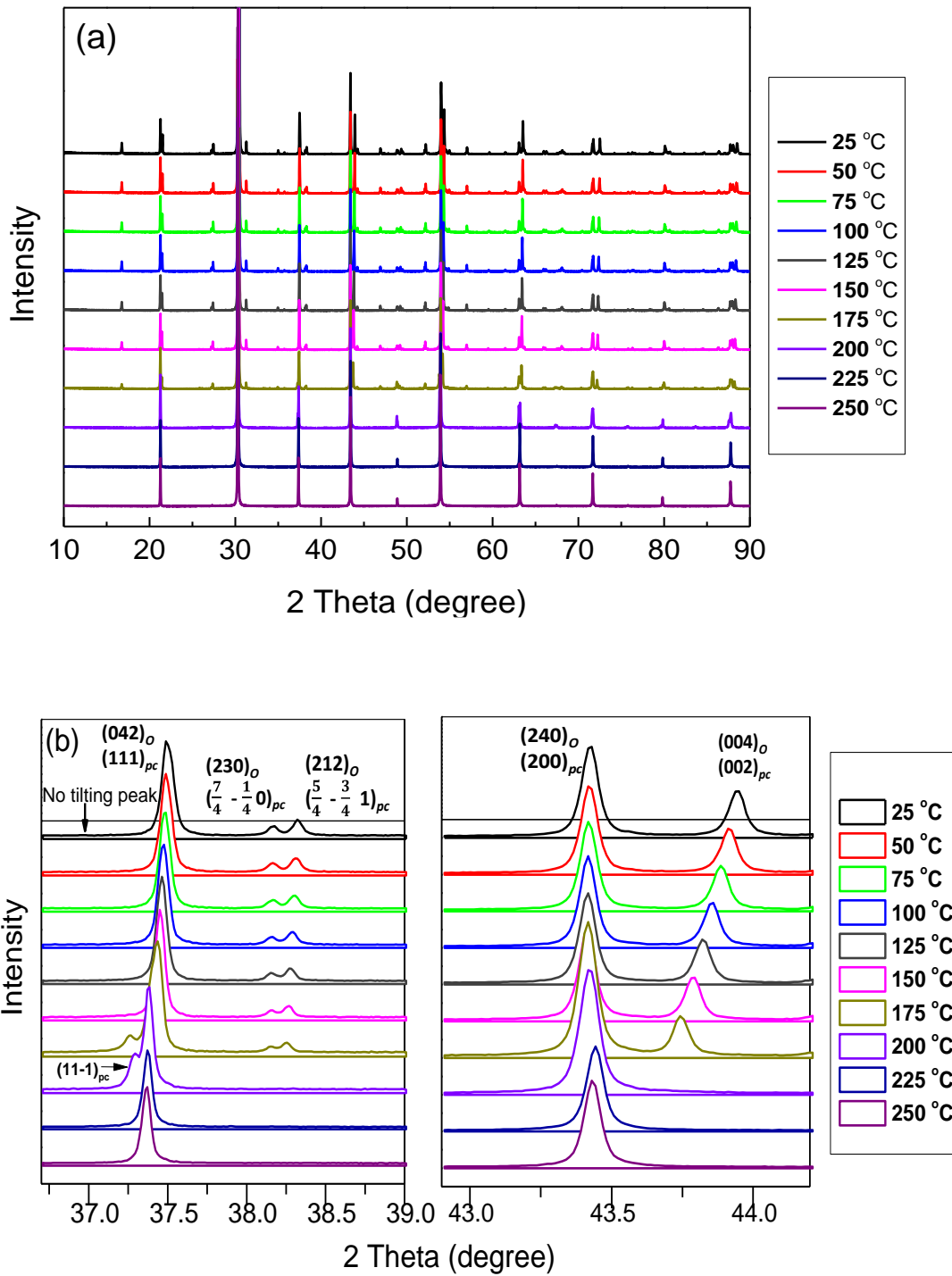
Figure 5.4. (a) Temperature evolution of the XRD patterns of the 97%PZ-3%PZnW ceramic. (b) Detailed X-ray diffraction patterns for some selected peaks measured at different temperatures.

Table 5.1. Rietveld-refined structural parameters for the 97%PZ-3%PZnW solid solution from the XRD data collected at difference temperatures on heating.

	x	y	z
25 ºC			
Pb1	0.71105(57)	0.12937(15)	0 1
Pb2	0.70871(57)	0.12424(15)	0.5
Zr1	0.24257(23)	0.12445(37)	0.25282(63)
Zn1	0.24257(23)	0.12445(37)	0.25282(63)
W1	0.24257(23)	0.12445(37)	0.25282(63)
O1	0.2918(43)	0.1022(27)	0
O2	0.2643(42)	0.1492(26)	0.5
O3	0.0249(15)	0.25694(79)	0.2767(32)
O4	0	0.5	0.2118(30)
O5	0	0	0.2379(52)
Dimensions (Å)	5.87612(3)	11.77017(6)	8.22348(4)
model	*Pbam*		
50 ºC			
Pb1	0.71147(76)	0.12930(16)	0
Pb2	0.70946(77)	0.12428(15)	0.5
Zr1	0.24229(23)	0.12443(38)	0.2492(18)
Zn1	0.24229(23)	0.12443(38)	0.2492(18)
W1	0.24229(23)	0.12443(38)	0.2492(18)
O1	0.2909(46)	0.1020(28)	0
O2	0.2665(45)	0.1469(27)	0.5
O3	0.0246(15)	0.25814(79)	0.2719(48)
O4	0	0.5	0.2100(36)
O5	0	0	0.2350(69)
Dimensions (Å)	5.87659(3)	11.76971(6)	8.22814(4)
model	*Pbam*		
75 ºC			
Pb1	0.71277(59)	0.12932(15)	0
Pb2	0.71025(60)	0.12437(15)	0.5
Zr1	0.24221(22)	0.12420(35)	0.25168(99)
Zn1	0.24221(22)	0.12420(35)	0.25168(99)
W1	0.24221(22)	0.12420(35)	0.25168(99)
O1	0.2906(44)	0.1052(25)	0
O2	0.2645(43)	0.1468(24)	0.5

	x	y	z
O3	0.0251(14)	0.25887(78)	0.2730(41)
O4	0	0.5	0.2105(33)
O5	0	0	0.2390(64)
Dimensions (Å)	5.87705(3)	11.76956(6)	8.23312(3)
model	*Pbam*		
100 ºC			
Pb1	0.71347(70)	0.12896(17)	0
Pb2	0.71232(70)	0.12437(17)	0.5
Zr1	0.24310(24)	0.12450(42)	0.2515(12)
Zn1	0.24310(24)	0.12450(42)	0.2515(12)
W1	0.24310(24)	0.12450(42)	0.2515(12)
O1	0.2883(48)	0.1030(30)	0 1 1.10(14)
O2	0.2668(47)	0.1452(29)	0.5
O3	0.0219(15)	0.25726(83)	0.2734(44)
O4	0	0.5	0.2114(36)
O5	0	0	0.2411(72)
Dimensions (Å)	5.87789(4)	11.7694(7)	8.23872(4)
model	*Pbam*		
125 ºC			
Pb1	0.71320(73)	0.12887(17)	0 1
Pb2	0.71525(73)	0.12444(17)	0.5
Zr1	0.24263(25)	0.12442(44)	0.2521(12)
Zn1	0.24263(25)	0.12442(44)	0.2521(12)
W1	0.24263(25)	0.12442(44)	0.2521(12)
O1	0.2881(54)	0.1064(29)	0 1
O2	0.2643(52)	0.1442(28)	0.5
O3	0.0200(15)	0.25723(85)	0.2704(42)
O4	0	0.5	0.2146(36)
O5	0	0	0.2320(57)
Dimensions (Å)	5.87834(4)	11.76891(7)	8.24423(4)
model	*Pbam*		
150 ºC			
Pb1	0.71603(89)	0.12864(19)	0
Pb2	0.71691(89)	0.12474(19)	0.5
Zr1	0.24309(26)	0.12448(41)	0.24783(92)
Zn1	0.24309(26)	0.12448(41)	0.24783(92)
W1	0.24309(26)	0.12448(41)	0.24783(92)

	x	y	z
O1	0.2825(65)	0.1052(30)	0 1
O2	0.2639(63)	0.1369(32)	0.5
O3	0.0215(16)	0.25751(89)	0.2694(41)
O4	0	0.5	0.2125(35)
O5	0	0	0.2362(62)
Dimensions (Å)	5.87884(4)	11.76859(7)	8.25056(3)
model	*Pbam*		

175 ºC

	x	y	z
Pb1	0.7188(79)	0.1285(26)	0
Pb2	0.7160(80)	0.1254(26)	0.5
Zr1	0.2437(34)	0.1239(45)	0.2492(10)
Zn1	0.2437(34)	0.1239(45)	0.2492(10)
W1	0.2437(34)	0.1239(45)	0.2492(10)
O1	-0.286(48)	-0.095(21)	0
O2	-0.252(73)	0.3672(51)	0.5
O3	0.4838(20)	0.7566(11)	0.2340(40)
O4	0	0.5	0.2887(48)
O5	0	0	0.2496(63)
Dimensions (Å)	5.87937(5)	11.76803(11)	8.25801(4)
model	*Pbam*	occupancy	60.2%

175 ºC

	x	y	z
Pbr	0	0	0.2387(13)
Zrr	0	0	0.0032(14)
Znr	0	0	0.0032(14)
Wr	0	0	0.0032(14)
Orh	0.1868(21)	0.3735(43)	0.083333
Dimensions (Å)	5.87316(5)	5.87316(5)	14.43869(16)
model	*R*3*m* (hexagonal setting)	occupancy	39.8%

200 ºC

	x	y	z
Pbr	0	0	0.23319(78)
Zrr	0	0	-0.00397(84)
Znr	0	0	-0.00397(84)
Wr	0	0	-0.00397(84)
Orh	0.1662(10)	0.3323(20)	0.083333
Dimensions (Å)	5.87516(3)	5.87516(3)	14.43006(12)
model	*R*3*m* (hexagonal setting)		

225 ºC

	x	y	z
Pbr	0	0	0 1
Zrr	0.5	0.5	0.5
Znr	0.5	0.5	0.5
Wr W	0.5	0.5	0.5
Orh	0.5	0.5	0
Dimensions (Å)	4.15594(2)	4.15594(2)	4.15594(3)
model	$Pm\overline{3}m$		
250 ºC			
Pbr	0	0	0
Zrr	0.5	0.5	0.5
Znr	0.5	0.5	0.5
Wr	0.5	0.5	0.5
Orh	0.5	0.5	0
Dimensions (Å)	4.15672(2)	4.15672(2)	4.15672(3)
model	$Pm\overline{3}m$		
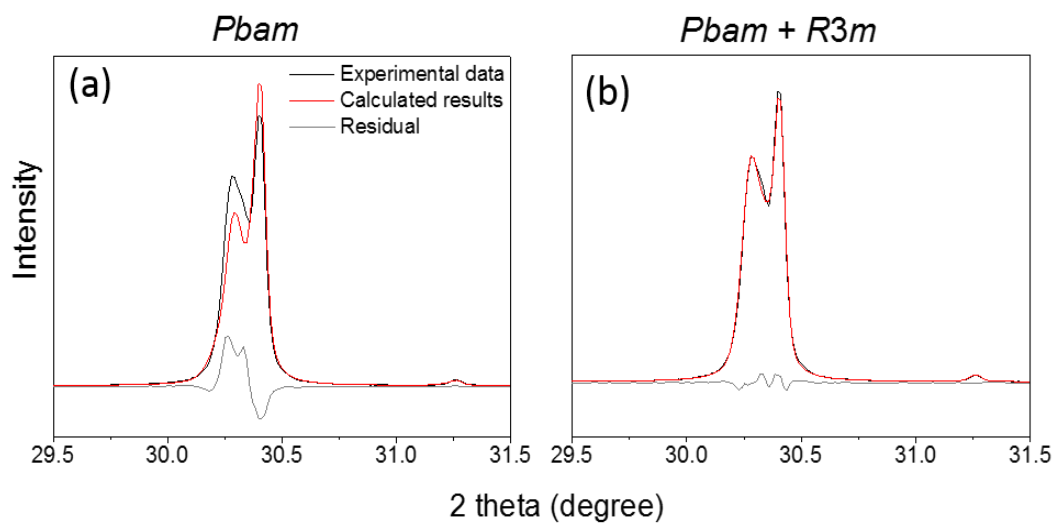
Figure 5.5. Refined peak profiles for the (1 1 0)$_{pc}$ reflection at 175 ºC with (a) *Pbam* structural model and (b) a mixture of *Pbam* + *R*3*m* models.

Overall, the 97%PZ-3%PZnW solid solution experiences a transition sequence from antiferroelectric *Pbam* to ferroelectric *R*3*m* and then to paraelectric *Pm*$\bar{3}$*m* phase on heating. This phase sequence is similar to that of the Ti-substituted PbZrO$_3$ ceramics with Ti concentration less than 6%.[110, 111] Figure 5.6a and Figure 5.6b depict the orthorhombic *Pbam* structure at 25 °C and the rhombohedral *R*3*m* structure in hexagonal setting at 200 °C, respectively, drawn based on the results of refinement. The green dash lines and arrows indicate the Pb displacements, and the yellow arrows show the displacement directions. Lead ion displaces along the b_H-axis [(1 1 0)$_{pc}$] in the orthorhombic structure and along the c_H-axis [(1 1 1)$_{pc}$] in the rhombohedral structure.
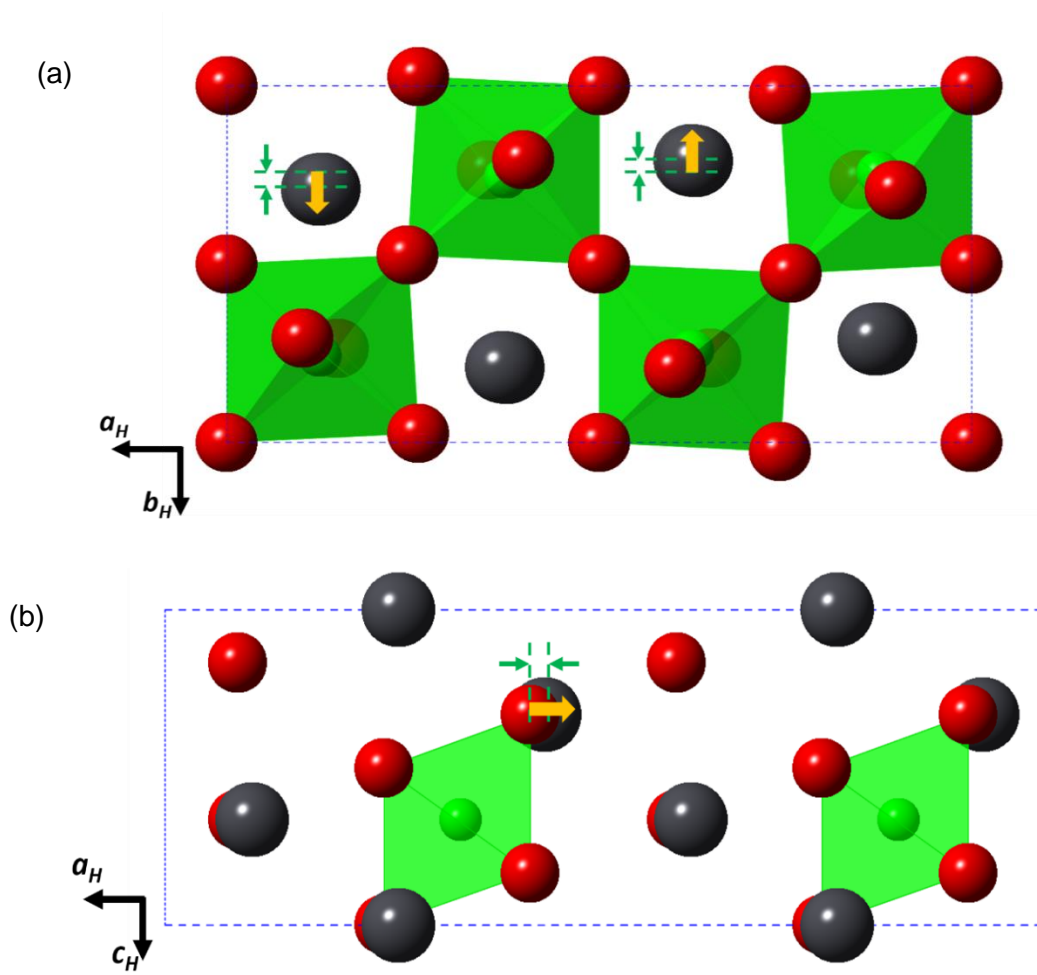
Figure 5.6.   The projection of the crystal structure of 97%PZ-3%PZnW, (a) at 25 °C along the c_O-axis and (b) at 200 °C along the b_H-axis. (a) is the orthorhombic *Pbam* structure and (b) is 1/3 of the rhombohedral *R*3*m* structure in the hexagonal setting. Green dash lines and arrows show the lead displacements in the unit cell while yellow arrows show the displacement directions.

For the purpose of comparison, the lattice parameters obtained from the above fittings are all converted into pseudocubic setting using the following equations:[92, 93]

$$a_{pc} = b_{pc} = \frac{1}{2}\sqrt{a_o^2 + \left(\frac{b_o}{2}\right)^2} \quad \text{and} \quad c_{pc} = \frac{1}{2}c_o \quad \text{(Orthorhombic).} \quad (5.1)$$

$$a_{pc} = b_{pc} = c_{pc} = \frac{1}{6}\sqrt{c_H^2 + 12a_H^2} \quad \text{(Rhombohedral),} \quad (5.2)$$

$$cos\gamma = \frac{c_H^2 - 6a_H^2}{c_H^2 + 12a_H^2} \quad \text{(Rhombohedral),} \quad (5.3)$$

$$\text{and} \quad cos\gamma = \frac{a_{pc}}{c_{pc}} \quad \text{(Orthorhombic).} \quad (5.4)$$

The results are listed in Table 5.2 and plotted in Figure 5.7a and 5.7b. It is seen from Figure 5.7a that the lattice constant c_{pc} increases significantly with increasing temperature in the *Pbam* phase, whereas $a_{pc}$ and b_{pc} only show a slighter increase. This suggests that the thermal energy expands the antiferroelectric *Pbam* structure more significantly in the c_{pc} direction than the others. At T_{AFE-FE} 175 °C, the *R3m* phase emerges abruptly, leading to a sudden change in the lattice parameters. At 200 °C, all the lattice constants merge into one lattice constant because the *Pbam* phase completely disappears and only the *R3m* phase is retained. Since *Pbam* and *R3m* are not group-subgroup related,[112] the discontinuous change in lattice parameters appears to be reasonable and it explains the first-order transition between the AFE and FE phases. On the other hand, *R3m* is one of the sub-groups of *Pm$\bar{3}$m,* therefore, a_{pc} changes continuously while passing thought T_C and this transition is a second-order transition. The continuous and discontinuous variations of the crystal structures at transition temperatures is more evidently reflected by the thermal variations of the lattice angle γ, i.e. the angle between a_{pc}- and b_{pc}- axes, as shown in Figure 5.7b.

Table 5.2. Lattice parameters for the various phases existing in the 97%PZ-3%PZnW solid solution at different temperatures, obtained from the Rietveld refinements.

Temperature (°C)	model	$a_{pc}\,(=b_{pc})$ (Å)	c_{pc} (Å)	ϒ (degree)	R_{wp}
25	*Pbam*	4.15822	4.11174	89.36	10.148
50	*Pbam*	4.15830	4.11407	89.39	9.996
75	*Pbam*	4.15844	4.11656	89.42	9.365
100	*Pbam*	4.15870	4.11936	89.46	10.356
125	*Pbam*	4.15878	4.12212	89.49	10.315
150	*Pbam*	4.15890	4.12528	89.53	11.169
175	*Pbam* (60%)	4.15898	4.12901	89.59	9.295
	R3m (40%)	4.15800	4.15800	89.86	9.295
200	*R3m*	4.15811	4.15811	89.90	10.574
225	*Pm-3m*	4.15594	4.15594	90.00	10.723
250	*Pm-3m*	4.15672	4.15672	90.00	10.599
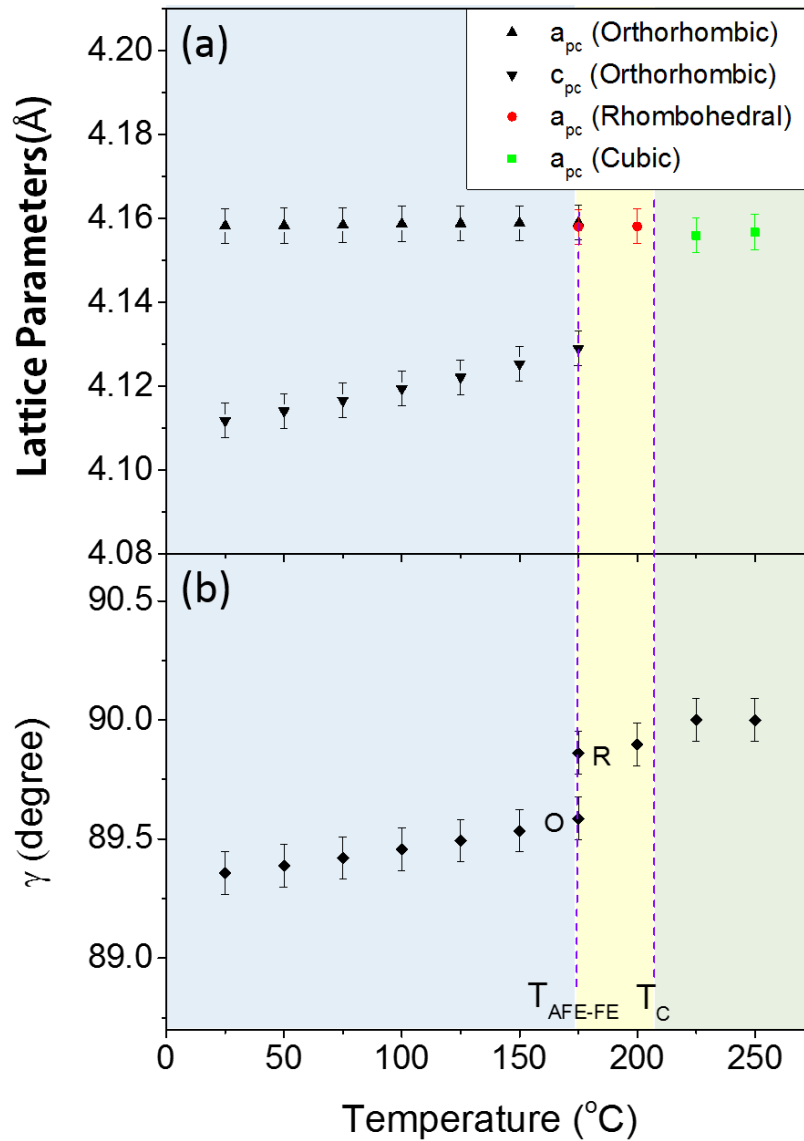
Figure 5.7.   Plots of (a) lattice constants and (b) angle γ as a function of temperature. O and R are short for orthorhombic and rhombohedral structures, respectively.

5.4.3.   Updated Phase Diagram of the (1-x)PbZrO₃-xPb(Zn₁/₂W₁/₂)O₃ Solid Solution

According to the high-temperature structural study, the compostion – temperature phase diagram from the previous work is updated and shown in Figure 5.8. The red solid line is a guideline to variation of the Curie temperatures as a function of composition. The blue and black lines are indications of T_{AFE-FE} with differernt compositions measured on

heating and cooling, respectively. Below T_{AFE-FE}, the solid solution remains in the antiferroelectric *Pbam* phase. At T_{AFE-FE}, a first-order phase transition takes place. The system then consists of a mixture of ferroelectric *R*3*m* and antiferroelectric *Pbam* phases at temperature slightly above T_{AFE-FE}. The portion of *Pbam* phase decreases upon heating and disppears eventually above T_{AFE-FE} (heating), giving rise to a pure *R*3*m* phase. Upon heating through T_C, the *R*3*m* structure transforms into the $Pm\bar{3}m$ phase gradually.
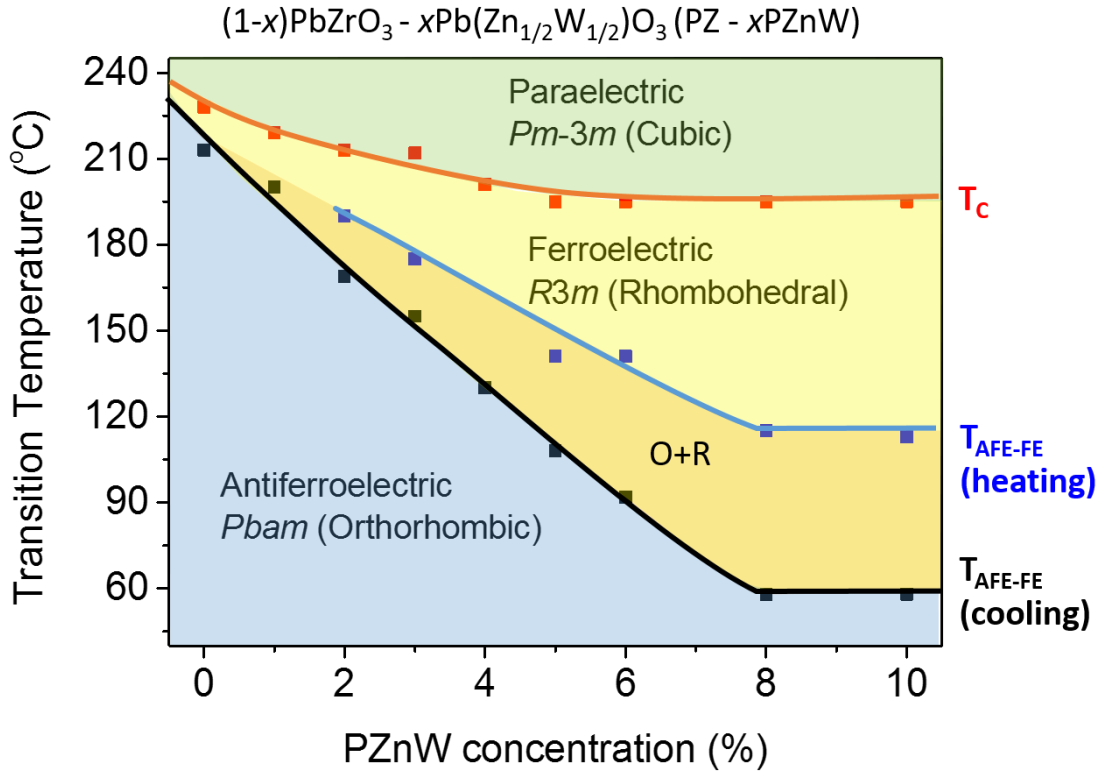
Figure 5.8. Temperature – compositon phase diagram established for the $(1\text{-}x)PbZrO_3\text{-}xPb(Zn_{1/2}W_{1/2})O_3$ solid solution system based on the experimental transition temperatures (dots) and their trends (solid lines) of T_C (red) and of $T_{AFE\text{-}FE}$ measured on heating (blue) and cooling (black).

5.5. Conclusions

The solid solution of $(1\text{-}x)PbZrO_3\text{-}xPb(Zn_{1/2}W_{1/2})O_3$, $x = 3\%$, is found to experience a sequence of transitions from the antiferroelectric to the intermediate ferroelectric and then to the paraelectric phase upon heating. The SHG measurement indicates the non-centrosymmetric nature for the intermediate phase and the typical ferroelectric

hysteresis loop displayed at T>T_{AFE-FE} reveals the ferroelectric character of this phase. The crystal structure is orthorhombic *Pbam* below T_{AFE-FE} and cubic *Pm$\bar{3}$m* above T_C. The intermediate ferroelectric phase is refined to be rhombohedral *R*3*m*, and it is expected to be representive of the other intermediate phases observed in PZ and other PZ-based systems. A thermal hystersis occurs at T_{AFE-FE}. On the other hand, the crystal structure turns from *R*3*m* to *Pm$\bar{3}$m* gradually at T_C and no thermal hysteresis is observed. Therefore, the transition between AFE and FE phases is of first-order while that between FE and PE phases is of second-order.

Chapter 6.

General Conclusions and Future Directions

6.1. General Conclusions

The research on ferroelectric (FE) and antiferroelectric (AFE) materials involves the design and synthesis of new materials with better properties, and the study of the relationship between structure and physical properties. FE and AFE properties are generated from parallel or antiparallel alignment of cation displacement. These properties can appear in the same structure (perovskite) with different subtle structural modifications. FE and AFE materials can be prepared in the form of ceramics, single crystals and thin films etc. In this work, the forms of ceramics and single crystals are mainly studied. Single crystals can be grown by high temperature solution growth method and top-seeded solution growth (TSSG) method. Ceramics can be synthesized by solid-state reaction. In general, single crystals are superior to their ceramic counterparts in terms of electrical properties, which make them the most promising materials for applications in devices that require high sensitivity, efficiency and power. The phase and purity of samples can be identified by X-ray diffractometer (XRD). Accurate lattice parameters can be obtained through Rietveld refinement. Polarized Light Microscopy (PLM) is practically helpful in studying the crystal symmetry of single crystals. Scanning electron microscope (SEM) is used as a tool to investigate the morphology of samples. Dielectric impedance spectroscopy is practical not only in terms of measuring dielectric properties but also in terms of studying phase evolution of samples. Ferroelectric impedance spectroscopy is utilized to investigate ferroelectric or antiferroelectric properties.

There are two major research projects described in this thesis. The first system is the $Pb(Sc_{1/2}Nb_{1/2})O_3$ (PSN) single crystals and the second one is the $(1-x)PbZrO_3-xPb(Zn_{1/2}W_{1/2})O_3$ [$(1-x)PZ-xPZnW$] solid solution in the form of ceramics.

In the first project, PSN single crystals were successfully grown using a high temperature solution growth method. XRD and PLM confirm the perovskite structure with rhombohedral symmetry for the as-grown PSN crystals. Relaxor properties have been observed in the as-grown PSN single crystals with diffuse peaks with frequency dispersion dielectric and satisfaction to the Vogel-Fulcher law and the quadratic law. PSN crystals in this work show lower dielectric maximum but higher temperature of dielectric peak, compared to PSN crystals grown under different conditions. These phenomena of PSN imply that the growth conditions can affect the properties of PSN crystals, presumably by altering the degree of B-cation ordering and the amount of lead vacancies. Poling the canonical relaxor of $Pb(Mg_{1/3}Nb_{2/3})O_3$ (PMN) can induce a macroscopic FE phase in the non-ergodic phase. Unlike PMN system, poling PSN crystals at room temperature does not induce any phases but change its dielectric properties, which suggests that some polar nano-regions (PNRs) remain in the FE state and they can be affected by the external fields.

In the second project, dense ceramics of a new antiferroelectric (1-x)PZ-xPZnW (x = 0% - 10%) solid solution with stable perovskite phases were successfully synthesized. The solubility limit was found to be x = 8%. Substitution of PZnW into PZ system does not affect the crystal symmetry but significantly expands the temperature range of the intermediate phase compared to PZ and other PZ-based solid solutions. From the ferroelectric property measurement, it is clear that the intermediate phase is a FE phase. The synthesized samples all undergo a transition sequence from antiferroelectric to intermediate ferroelectric and then to paraelectric (PE) phase. This transition sequence is reversible. XRD patterns of the 97%PZ-3%PZnW ceramic are measured upon heating. Based on the Rietveld refinement results, it is found that the AFE, FE and PE phases belong to the space groups of *Pbam*, *R*3*m* and *Pm*$\bar{3}$*m*, respectively.

6.2. Future Directions

By far, there is proof that the growth parameters have influenced the PSN crystal properties and quality, by affecting their compositional order and the amount of lead vacancies. However, variation of growth parameters has not been studied in this thesis.

Also, diverse growth techniques need to be developed, e.g. the top-seeded solution growth (TSSG) method. On the other hand, the mechanisms of poling effects in PSN crystals require deeper investigation.

Impurity was detected in some compositions of (1-x)PZ-xPZnW solid solution which means the synthetic conditions should be optimized. In order to further enhance the performance of the solid solution, it is better to grow single crystals of this solid solution. (1-x)PZ-xPZnW solid solution still exhibits AFE properties with high critical field (E_F) at room temperature, chemical modification with B-site ions such as Nb^{5+} could be performed in order to find the optimum composition for high-density energy storage capacitors and high-strain transducers.

Bibliography

1.   H. Kronmüller and S. Parkin, John Wiley & Sons (2007).

2.   H. J. Goldschmidt and J. R. Rait, Nature **152**, 356 (1943).

3.   R. E. Eitel, C. A. Randall, T. R. Shrout, P. W. Rehrig, W. Hackenberger and S.-E. Park, Jpn. J. Appl. Phys. **40**, 5999-6002 (2001).

4.   J. Curie and P. Curie, Bulletin de la Société minérologique de France **3**, 90-93 (1880).

5.   G. H. Haertling, J. Am. Ceram. Soc. **82** (4), 797–818 (1999).

6.   D. Damjanovic, Rep. Prog. Phys. **61**, 1267–1324 (1998).

7.   S. V. Kalinin and A. Gruverman, Scanning Probe Microscopy: Electrical and Electromechanical Phenomena at the Nanoscale, Springer (2010).

8.   A. R. West, Basic Solid State Chemistry second Edition, Chichester (1996).

9.   H. Ibach and H. Lüth, Solid-State Physics, Springer (2009).

10.   B. Jaff, Proceedings of the IRE **49** (8), 1264-1267 (1961).

11.   X. Hao, J. Zhai, L. B. Kong and Z. Xu, Progress in Materials Science **63**, 1-57 (2014).

12.   C. Haas, Phys. Rev. **140** (3A), A863-A868 (1965).

13.   I. Burn and D. M. Smyth, J. Mater. Sci. **7**, 339-343 (1972).

14.   Y. Xu, Ferroelectric Materials and Their Applications, North-Holland (1991).

15.   M. E. Lines and A. M. Glass, Principles and Applications of Ferroelectrics and Related Materials, Clarendon Press (1977).

16.   A. F. Devonshire, The London, Edinburgh, and Dublin Philosophical Magazine and Journal of Science: Series 7 **40** (309), 1040-1063 (1949).

17. H. Yan, F. Inam, G. Viola, H. Ning, H. Zhang, Q. Jiang, T. Zeng, Z. Gao and M. J. Reece, J Adv. Dielectr. **01** (01), 107-118 (2011).

18. A. A. Bokov and Z.-G. Ye, J. Mater. Sci. **41** (1), 31-52 (2006).

19. Z.-G. Ye, Key Eng. Mater. **155-156**, 81-122 (1998).

20. L. E. Cross, Ferroelectrics **76** (1), 241-267 (1987).

21. G. A. Smolenskii, V. A. Iupov, A. I. Agranovskaya and S. N. Popov, Sov. Phys. Solid State **2**, 2584 (1961).

22. A. Krumins, T. Shiosaki and S. Koizumi, Jpn. J. Appl. Phys. **33**, 4940 (1994).

23. C. G. F. Stenger and A. J. Burggraaf, Phys. Stat. Sol. (a) **61** (1), 275-285 (1980).

24. C. G. F. Stenger and A. J. Burggraaf, Phys. Stat. Sol. (a) **61** (2), 653-664 (1980).

25. D. Viehland, S. J. Jang, L. E. Cross and M. Wuttig, J. Appl. Phys. **68** (6), 2916-2921 (1990).

26. Z.-G. Ye and A. A. Bokov, Solid State Commun. **116**, 105-108 (2000).

27. G. A. Smolenskii, V. A. Isupov and A. I. Agranovskaya, Sov. Phys. Solid State **1**, 150 (1959).

28. F. Galasso and W. Darby, Inorg. Chem. **4** (1), 71-73 (1965).

29. V. G. Smotrakov, I. P. Raevskii, M. A. Malitsskaya, S. M. Zaitsev, Y. M. Popov and N. A. Strekneva, Inorg. Muter. **19**, 105 (1983).

30. Y. Bing and Z.-G. Ye, International Symposium on Applications of Ferroelectrics (ISAF 2002), 447-450 (2002).

31. A. A. Bokov, I. P. Raevskii and V. G. Smotrakov, Sov. Phys. Solid State **25** (7), 1168-1170 (1983).

32. F. Chu, I. M. Reaney and N. Setter, J. Appl. Phys. **77** (4), 1671-1676 (1995).

33. F. Chu, I. M. Reaney and N. Setter, J. Am. Ceram. Soc. **78** (7), 1947-1952 (1995).

34. Y. H. Bing, A. A. Bokov and Z.-G. Ye, Curr. Appl. Phys. **11** (3), S14-S21 (2011).

35. Z.-G. Ye and H. Schmid, Ferroelectrics **145** (1), 83-108 (1993).

36.   M. Ahart, A. Hushur, Y. Bing, Z.-G. Ye, R. J. Hemley and S. Kojima, Appl. Phys. Lett. **94** (14), 142906 (2009).

37.   H. Y. Guo, Y. H. Bing and Z.-G. Ye, J. Appl. Phys. **112** (5), 052009 (2012).

38.   G. Shirane, E. Sawaguchi and Y. Takagi, Phys. Rev. **84** (3), 476-481 (1951).

39.   H. Fujishita and S. Hoshino, J. Phys. Soc. Jpn. **53** (1), 226-234 (1984).

40.   A. M. Glazer, K. Roleder and J. Dec, Acta Cryst. **B49**, 846-852 (1993).

41.   B. A. Scott and G. Burns, J. Am. Ceram. Soc. **55** (7), 331-333 (1972).

42.   R. W. Whatmore and A. M. Glazer, J. Phys. C: Solid State Phys. **12**, 1505-1519 (1979).

43.   M. J. Haun, T. J. Harvin, M. T. Lanagan, Z. Q. Zhuang, S. J. Jang and L. E. Cross, J. Appl. Phys. **65** (8), 3173-3180 (1989).

44.   M. Chen, X. Yao and L. Zhang, J. Eur. Ceram. Soc. **21**, 1159-1164 (2001).

45.   W. Pan, Q. Zhang, A. Bhalla and L. E. Cross, J. Am. Ceram. Soc. **72** (4), 571-579 (1989).

46.   N. Vittayakorn, P. Charoonsuk, P. Kasiansin, S. Wirunchit and B. Boonchom, J. Appl. Phys. **106** (6), 064104 (2009).

47.   U. Sukkha, R. Muanghlua, S. Niemcharoen, B. Boonchom and N. Vittayakorn, J. Am. Ceram. Soc. **94** (10), 3397-3404 (2011).

48.   W. Banlue and N. Vittayakorn, Appl. Phys. A **93** (2), 565-569 (2008).

49.   C. Perrin, N. Menguy, E. Suard, C. Muller, C. Caranoni and A. Stepanov, J. Phys.: Condens. **12**, 7523-7539 (2000).

50.   M. Ladd and R. Palmer, Structure Determination by X-Ray Cristallography, Springer Science & Business Media (2013).

51.   N. Technologies, Novocontrol Technologies GmbH & Co. KG (2012).

52.   G. Willians and D. K. Thomas, Novocontrol Application Note Dielectrics (1998).

53.   C. Sawyer and C. Tower, Phys. Rev. **35** (3), 269-273 (1930).

54.   P. Dimitruk and M. W. Davidson, 2012 Olympus America Inc. (2013).

55.   M. Françon and S. Mallick, Polarization Interferometers: Applications in Microscopy and Macroscopy, John Wiley & Sons Ltd (1971).

56.   W. J. Patzelt, Ernst Leitz Wetzlar GmbH (1985).

57.   A. A. Bokov, X. Long and Z.-G. Ye, Phys. Rev. B **81** (17), 172103 (2010).

58.   K. Uchino, Ferroelectrics **151** (1), 321-330 (1994).

59.   N. Ortega, A. Kumar, J. F. Scott, D. B. Chrisey, M. Tomazawa, S. Kumari, D. G. Diestra and R. S. Katiyar, J. Phys.: Condens. Matter. **24** (44), 445901 (2012).

60.   B. Fang, R. Sun, Y. Shan, K. Tezuka and H. Imoto, J. Mater. Sci. **42** (22), 9227-9233 (2007).

61.   C. Malibert, B. Dkhil, J. M. Kiat, D. Durand, J. F. Berar and A. S.-D. Bire, J. Phys.: Condens. Matter. **9**, 7485-7500 (1997).

62.   N. Takesue, M. Y. Fujii , H. Chen, S. Tatemori and J. Hatano, J. Phys.: Condens. Matter. **11**, 8301-8312 (1999).

63.   C. G. F. Stenger and A. J. Burggraaf, Phys. Stat. Sol. (a) **61** (1), 275-285 (1980).

64.   K. Z. Baba-Kishi, P. M. Woodward and K. Knight, Ferroelectrics **261** (1), 21-26 (2001).

65.   B. J. Maier, R. J. Angel, B. Mihailova, W. G. Marshall, M. Gospodinov and U. Bismayer, J. Phys.: Condens. Matter. **23** (3), 035902 (2011).

66.   N. M. C Perrin, E Suard, Ch Muller, C Caranoni and A Stepanov, J. Phys.: Condens. Matter **12**, 7523-7539 (2000).

67.   E. Venturini, R. Grubbs, G. Samara, Y. Bing and Z.-G. Ye, Physical Review B **74** (6), 064108 (2006).

68.   A. E. Glazounov and A. K. Tagantsev, Ferroelectrics **221**, 57-66 (1999).

69.   I. Rychetsky, S. Kamba, V. Porokhonskyy, A. Pashkin, M. Savinov, V. Bovtun, J. Petzelt, M. Kosec and M. Dressel, J. Phys.: Condens. Matter. **15**, 6017-6030 (2003).

70.   P. Dhak, D. Dhak, T. Subashchandrabose, M. Das and P. Pramanik, J. Nanopart. Res. **13**, 4153-4159 (2011).

71.   R. Haumont, B. Dkhil, J. M. Kiat, A. Al-Barakaty, H. Dammak and a. L. Bellaiche, Phys. Rev. B **68**, 014114 (2003).

72.   J. Parui and S. B. Krupanidhi, Appl. Phys. Lett. **92** (19), 192901 (2008).

73.   C. Piyanut, W. Supamas, M. Rangson, N. Surasak, B. Banjong and N. Vittayakorn, J. Alloys Compd. **506** (1), 313-316 (2010).

74.   W. Y. Pan, C. Q. Dam, Q. M. Zhang and L. E. Cross, J. Appl. Phys. **66** (12), 6014-6023 (1989).

75.   L. E. Cross, J. Phys. Soc. Jpn. **23** (1), 77-82 (1967).

76.   W. Qu, X. Tan, N. Vittayakorn, S. Wirunchit and M. F. Besser, J. Appl. Phys. **105** (1), 014106 (2009).

77.   F. Jona, G. Shirane, F. Mazzi and R. Pepinsky, Phys. Rev. **105** (3), 849-856 (1957).

78.   O. E. Fesenko, R. V. Kolesova and Y. G. Sindeyev, Ferroelectrics **20** (1), 177-178 (1978).

79.   N. Vittayakorn, T. Bongkarn and G. Rujijanagul, Physica B: Condensed Matter **387** (1-2), 415-420 (2007).

80.   D. Viehland, X. H. Dai, J. F. Li and Z. Xu, J. Appl. Phys. **84** (1), 458 (1998).

81.   P. Liu and X. Yao, Solid State Commun. **132** (12), 809-813 (2004).

82.   R. Rivera and A. Stashans, Phys. Scr. **78** (4), 045601 (2008).

83.   I. Jankowska-Sumara, A. Majchrowski and J. Żmija, J. Mater. Sci. **44** (12), 3229-3234 (2009).

84.   V. V. Shvartsman, E. D. Politova and S. Y. Stefanovich, Ferroelectrics **238** (1), 123-130 (2000).

85.   U. Sukkha, R. Muanghlua, S. Niemcharoen, B. Boonchoma and N. Vittayakorn, Appl. Phys. A **100** (2), 551-559 (2010).

86.   S. Wirunchit and N. Vittayakorn, Appl. Phys. A **104** (2), 024103 (2008).

87.   X. Tan, C. Ma, J. Frederick, S. Beckman, K. G. Webber and D. J. Green, J. Am. Ceram. Soc. **94** (12), 4091-4107 (2011).

88.   H. He and X. Tan, Phys. Rev. B **72** (2), 024102 (2005).

89.   V. Heine and J. McConnell, Phys. Rev. Lett. **46** (16), 1092-1095 (1981).

90.   T. Asada and Y. Koyama, Phys. Rev. B **69** (10), 104108 (2004).

91.   B. Okai, J. Yoshimoto and T. Fujita, J. Phys. Soc. Jpn. **37**, 281 (1974).

92.   W.-J. Lee and N.-K. Kim, J. Mater. Sci. **43** (10), 3608-3611 (2008).

93.   O. Khamman, X. Tan, S. Ananta and R. Yimnirun, J. Mater. Sci. **44** (7), 1868-1872 (2009).

94.   Z. Ren, N. Zhang, S. Huo, J. Y. Y. Wong and Z.-G. Ye, Ferroelectrics **464** (1), 27-34 (2014).

95.   I. Grinberg, M. R. Suchomel, P. K. Davies and A. M. Rappe, J. Appl. Phys. **98** (9), 094111 (2005).

96.   G. Baldinozzi, P. Sciau, M. Pinot and D. Grebille, Acta Cryst. **B51**, 668-673 (1995).

97.   H. D. Megaw and C. N. W. Darlington, Acta Cryst. **A31**, 161-173 (1975).

98.   N. Zhang, H. Yokota, A. M. Glazer and P. A. Thomas, Acta Crystallogr., Sect. B: Struct. Sci. **67**, 386-398 (2011).

99.   J. Parui and S. B. Krupanidhi, Appl. Phys. Lett. **92** (19), 192901 (2008).

100.   F. C. Pulvari, Phys. Rev. **120** (5), 1670-1673 (1960).

101.   G. Samara, Phys. Rev. B **1** (9), 3777-3786 (1970).

102.   M. A. De La Rubia, R. E. Alonso, A. R. López-Garcia and J. D. Frutos, IEEE transactions on ultrasonics, ferroelectrics, and frequency control **56** (9), 1799-1805 (2009).

103.   B. P. Pokharel and D. Pandey, J. Appl. Phys. **86** (6), 3323-3327 (1999).

104.   X. Hao, J. Zhai and X. Yao, J. Am. Ceram. Soc. **92** (5), 1133-1135 (2009).

105.   E. Mensur Alkoy and T. Shiosaki, J. Am. Ceram. Soc. **92** (2), 396-404 (2009).

106.   O. F. T. Fujita, T. Nakagawa and S. Nomura, Mat. Res. Bull. **5**, 759-764 (1970).

107.   W.-J. Lee, J.-S. Kim and N.-K. Kim, J. Eur. Ceram. Soc. **27** (16), 4473-4478 (2007).

108.   S. Huo, Z. Ren, N. Zhang and Z.-G. Ye, in preparation.

109.   N. Masó, D. I. Woodward, P. A. Thomas, A. Várez and A. R. West, J. Mater. Chem. **21** (8), 2715 (2011).

110.   D. Woodward, J. Knudsen and I. Reaney, Phys. Rev. B **72** (10) (2005).

111.   H. Hassan, M. Maglione, M. D. Fontana and J. Handerek, J. Phys.: Condens. Matter. **7**, 8647-8654 (1995).

112.   H. T. Stokes, E. H. Kisi, D. M. Hatch and C. J. Howard, Acta Crystallogr., Sect. B: Struct. Sci. B **58**, 934-938 (2002).